BRNO UNIVERSITY OF TECHNOLOGY
VYSOKÉ UČENÍ TECHNICKÉ V BRNĚ

FACULTY OF ELECTRICAL ENGINEERING AND COMMUNICATION
DEPARTMENT OF RADIO ELECTRONICS
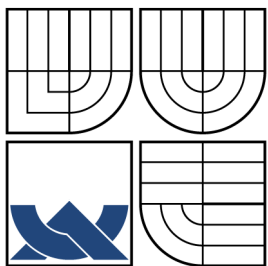
FAKULTA ELEKTROTECHNIKY A KOMUNIKAČNÍCH TECHNOLOGIÍ
ÚSTAV RADIOELEKTRONIKY

PULSED ELECTROMAGNETIC FIELD RADIATION FROM SLOT ANTENNAS

DOCTORAL THESIS
DOKTORSKÁ PRÁCE

AUTHOR   MARTIN ŠTUMPF
AUTOR PRÁCE

BRNO UNIVERSITY OF TECHNOLOGY
VYSOKÉ UČENÍ TECHNICKÉ V BRNĚ

FACULTY OF ELECTRICAL ENGINEERING AND
COMMUNICATION
DEPARTMENT OF RADIO ELECTRONICS

FAKULTA ELEKTROTECHNIKY A KOMUNIKAČNÍCH
TECHNOLOGIÍ
ÚSTAV RADIOELEKTRONIKY

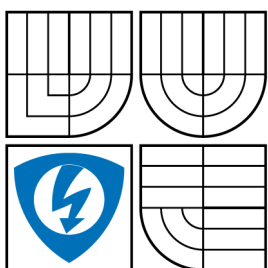# PULSED ELECTROMAGNETIC FIELD RADIATION FROM SLOT ANTENNAS
PULZNÍ ELEKTROMAGNETICKÉ ZÁŘENÍ ŠTĚRBINOVÝCH ANTÉN

DOCTORAL THESIS
DOKTORSKÁ PRÁCE

AUTHOR   MARTIN ŠTUMPF
AUTOR PRÁCE

SUPERVISORS   Dr. JAROSLAV LÁČÍK
VEDOUCÍ PRÁCE

                                Prof. ADRIANUS T. DE HOOP

                                Dr. IOAN E. LAGER

BRNO 2011

ABSTRACT

Simple two-dimensional antenna radiators that serve as building blocks of antenna arrays are analyzed analytically in the time-domain. As a main tool for the analysis the Cagniard-DeHoop method is employed. It is shown that the chosen approach is capable of providing the exact and closed-form time-domain expressions that clearly demonstrate the influence of input parameters involved and elucidate physical insights into the pulsed electromagnetic field radiation behavior. Given numerical examples illustrate important features of the pulsed electromagnetic fields in diverse problem configurations. The obtained results are useful for the efficient design of antenna arrays excited by pulsed fields.

KEYWORDS

time-domain, pulsed electromagnetic field, slot antenna, antenna array, Cagniard-DeHoop technique

ABSTRAKT

Jednoduché dvojrozměrné anténní zářiče, které slouží jako stavební bloky anténních polí, jsou analyticky analyzovány v časové oblasti. Jako hlavní nástroj pro analýzu je použita Cagniard-DeHoopova metoda. Je ukázáno, že zvolený přístup umožňuje získat přesné vzorce v časové oblasti v uzavřeném tvaru, které jasně demonstrují vliv vstupních parametrů a objasňují fyzikální podstatu pulsního elektromagnetického vyzařování. Dané numerické výsledky ilustrují důležité aspekty pulsního elektromagnetického záření v rozličných konfiguracích problémů. Získané výsledky jsou užitečné pro efektivní návrh anténních polí, které jsou buzeny pulsními signály.

KLÍČOVÁ SLOVA

časová oblast, pulsní elektromagnetické pole, štěrbinová anténa, anténní pole, Cagniard-DeHoopova technika

DECLARATION

I declare that I have elaborated my doctoral thesis on the theme of "Pulsed electro-magnetic field radiation from slot antennas" independently, under the supervision of the doctoral thesis supervisors and with the use of technical literature and other sources of information which are all quoted in the thesis and detailed in the list of literature at the end of the thesis.

As the author of the doctoral thesis I furthermore declare that, concerning the creation of this doctoral thesis, I have not infringed any copyright. In particular, I have not unlawfully encroached on anyone's personal copyright and I am fully aware of the consequences in the case of breaking Regulation $\S\,11$ and the following of the Copyright Act No 121/2000 Vol., including the possible consequences of criminal law resulted from Regulation $\S\,152$ of Criminal Act No 140/1961 Vol.

Brno   . . . .
                                          (author's signature)

Contents

... "But why are such terrific efforts made just to find new particles?" asked Mr Tompkins.

"Well, this is science," replied the professor, "the attempt of the human mind to understand everything around us, be it giant stellar galaxies, microscopic bacteria, or these elementary particles. It is interesting and exciting and that is why we are doing it."

"But doesn't the development of science serve practical purposes by improving the comfort and well being of people?"

"Of course it does, but this is only a secondary purpose. Do you think that the main purpose of music is to teach buglers to waken soldiers in the morning, to call them for meals, or to order them to go into battle? They say "curiosity kills the cat"; I say "Curiosity makes a scientist"."

And with these words the professor wished Mr Tompkins a good night.

– Mr Tompkins Explores the Atom, G. Gamow

Chapter 1

Introduction

Recently, with the advent of communication systems based on the transfer, identification and subsequent interpretation of digital signals, there is a growing importance of the time-domain analysis of such systems. One of the actual requirements imposed on modern communication systems is the capability of providing a bundle of services for a high number of customers. These new capabilities bear high demands on the signal processing and front-end parts of communication systems. Since the signals between the transmitting and receiving parts of such communication systems must be steered in specified directions, a utilization of antenna structures that provide a spatial filtering is necessary. This calls for the use of antenna arrays and the investigation of their pulsed field radiation behavior.

The important building block of an antenna array is the radiator itself which can take various forms. One of the practically well verified antenna array elements consists of an aperture that can be realized as an open end of a waveguide or as a horn. Since the aperture type antennas are frequently used in intricate ambient conditions (for example, in aeronautical applications), their openings are usually protected by a dielectric covering that can significantly affect the radiation behavior. A synthesis of antenna arrays is therefore unavoidably connected with an understanding of the antenna element behavior itself in diverse circumstances.

Beside of this, a pulsed field behavior of simple aperture radiators and antenna arrays is of a great interest in the design and optimisation of inter- and intra-chip wireless pulsed signal transfer channels in integrated circuits. The need of wireless integrated circuit interconnects that are capable of transfering pulsed-shaped (bit-like) signals originates in the trend of miniaturization of electronic circuit components and in the using of still higher bit rates, which leads to the impossibility of realising the required interconnects in the classical electrical conductive-wire manner. The research on this subject is nowadays in full progress [24, 25].

1.1   Compendium of relevant approaches

In order to satisfy the high demands of advanced communication systems, an efficient design of antenna array requires a tool that clearly demonstrates the influence of the involved configurational and excitation parameters. This requirement can hardly be met with traditional numerical approaches (Finite Difference Method, Finite Element Method,

Method of Moments) that provide single-purpose results giving superficial insights only. On this account, an application and investigation of analytical techniques is in our scope of interest. Although antenna enginnering has a long history, the pulsed field behavior of antenna systems is still a subject seldom touched upon. In this respect, the analysis of pulsed behavior of antenna systems and the time-domain description of an antenna itself has received attention in [4, 17, 38].

The early works on the analysis of microwave components with a construction based on the horizontally stratified media lean upon the formulation of Sommerfeld [39, 40]. Sommerfeld's approach involves the Fourier transformation with respect to time followed by the 'cylindrical' form of the two-dimensional Fourier transformation with respect to the spatial coordinates parallel to the media interface (Fourier-Bessel transformation). The same theoretical machinery led to the development of the frequency-domain integral equation technique [31]. The main drawback of this approach is a demanding numerical solution of an inverse spatial-transformation integral (commonly known as Sommerfeld's integral). In general, the Sommerfeld-type integral has an unbounded domain of integration, oscillatory integrands containing the pole and branch-point singularities. The mentioned difficulties are ussually solved via the proper choice of an integration contour and by special extrapolation techniques accelerating the convergence of numerical integration [30]. Despite of the inherent drawbacks, the frequency-domain integral equation technique has proved to be useful for analyses of various microwave devices based on the microstrip structure [32].

Regarding the radiation from flanged parallel-plate waveguides excited by an incident mode a number of approaches have been formerly applied. They are mainly focused on an aperture radiator description in terms of the aperture admitance and self-reflection coefficients connected with a particular excitation mode. These approaches are based on a variational problem formulation [29], on the correlation matrix technique [28] or on the asymptotical ray method [26]. The 'classical' approach is described in Harrington's book [22, Sec. 3.11]. In the latter, the one-dimensional Fourier transforms are applied with respect to time and horizontal spatial coordinate. The difficulties arise when one attempts to perform an inverse spatial Fourier transformation. Again, this can be done numerically or, for particular cases, through the asymptotic integration techniques [20, Sec. 4].

The difficulties involved in Sommerfeld's formulation have been avoided by De Hoop's modification of Cagniard's method [5, 6] which is widely known as the Cagniard-DeHoop technique [2, 3, 7, 10, 11, 21]. The Cagniard-DeHoop method is based on the combination of a unilateral Laplace transformation with respect to time with the spatial slowness representation such that the time-domain counterpart is found by inspection, without making use of an inverse Laplace transformation. The corresponding procedure based on the time Fourier transform can be found in Chew's book [9, Sec. 4.2]. The Cagniard-DeHoop allows for the inclusion of Boltzmann-type relaxation behavior (which includes, for example, Lorentz-line and Drude/Debye-absorption behavior) at the expense of having to use more complicated theorems of the time Laplace transformation. In this respect, the generalized Cagniard-DeHoop technique [14, 16, 18] employing the Schouten-VanDerPol theorem [37, 43] has been developed.

1.2 Statement of the problem

Based on the observation that all other known approaches (which include both numerical and analytical ones) do not yield exact solutions of the problem in hand, the pulsed field radiation behavior of the slot antennas is investigated by means of the Cagniard-DeHoop technique. The Cagniard-DeHoop method yields the closed-form expressions providing the pulsed radiated electromagnetic fields as functions of position and time. Such expressions clearly demonstrate the influence of the parameters involved and thus provide useful insights into the slot antenna synthesis. They serve as the basis for carrying out parameter sensitivity analyses as to pulse shapes in relation to the geometrical and physical parameters of the configuration. Since the expressions obtained can be evaluated at a given observation position and within any finite time window with any prescribed accuracy, they can serve as a benchmark tool in the use of purely computational techniques that are required for the configurations of higher complexity.

Our investigation is aimed at two-dimensional structures only. More precisely, the pulsed electromagnetic field radiation from a slot, that would be conceived as an open end of the parallel-plate waveguide, is thoroughly investigated in a number of configurations. An excitation field distribution over the radiating aperture is prescribed in two ways. The uniform excitation field distribution corresponds to the radiation from a parallel-plate waveguide carrying the Transverse ElectroMagnetic (TEM) mode, while a nonuniform excitation field distribution corresponds to, in our case, the Transverse Magnetic (TM) modal excitation. The applied theory can be further generalized to account for three-dimensional radiators.

1.3 General conventions

1.3.1 Employed quantities

Throughout this thesis light-faced Roman or Greek symbols stand for scalars. The tensors of higher order are preferably handled with the subscript (indicial) notation. In it, the latin subscript can stand for $\{1, 2, 3\}$. Whenever appropriate the Roman bold-face letters stand for vectors.

In order to localize the position of a point in a Cartesian space $\mathbb{R}^3$, the orthogonal right-handed Cartesian reference frame is employed (see Fig. 1.1). The spatial reference frame is defined with respect to the origin O and the three mutually perpendicular base vectors $\{\boldsymbol{i}_1, \boldsymbol{i}_2, \boldsymbol{i}_3\}$ of unit length each; they form, in the indicated order, a right-handed system. Within this reference frame, the position of a point is defined by the vector

$$\boldsymbol{x} = x_1 \boldsymbol{i}_1 + x_2 \boldsymbol{i}_2 + x_3 \boldsymbol{i}_3 \tag{1.1}$$

The partial differentiations with respect to x_m is denoted as ∂_m. The symbols t and ∂_t are reserved for the time coordinate and the partial differentiation with respect to time, respectively. Such product of arithmetic arrays is ussually written in a shorthand way with the help of the summation convention

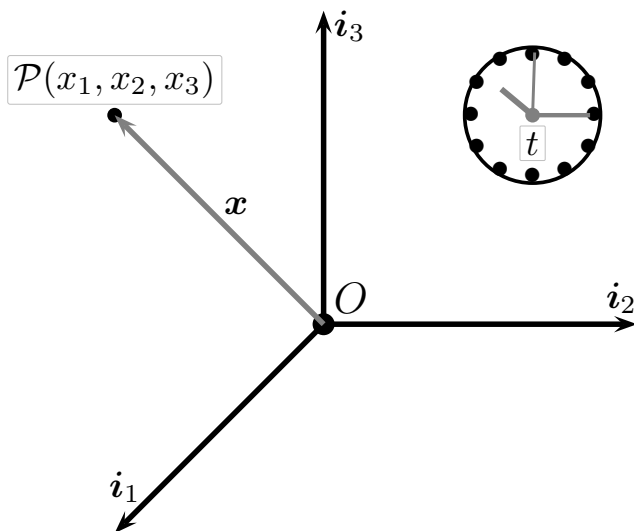$$\boldsymbol{x} = x_k \boldsymbol{i}_k \tag{1.2}$$

Figure 1.1: Orthogonal Cartesian reference frame with origin O and three mutually perpendicular base vectors $\{\boldsymbol{i}_1, \boldsymbol{i}_2, \boldsymbol{i}_3\}$ of unit length each, position vector $\boldsymbol{x} = x_1\boldsymbol{i}_1 + x_2\boldsymbol{i}_2 + x_3\boldsymbol{i}_3$, and time coordinate t.

where the repeated (dummy) subscript implies a summation. Special tensors that are in use are the Kronecker and Levi-Civita tensors. The Kronecker tensor is the symmetrical unit tensor of rank two defined as

$$\delta_{p,q} = \begin{cases} 1 \text{ if } p = q \\ 0 \text{ if } p \neq q \end{cases} \tag{1.3}$$

The Levi-Civita tensor is the completely antisymmetrical unit tensor of rank three defined as

$$\boldsymbol{e}_{k,m,p} = \begin{cases} 1 & \text{if } \{k, m, p\} \text{ is even permutation of } \{1, 2, 3\} \\ -1 & \text{if } \{k, m, p\} \text{ is odd permutation of } \{1, 2, 3\} \\ 0 & \text{all other cases} \end{cases} \tag{1.4}$$

1.3.2 Employed integral transformations

As a basic tool for the analysis we employ the advantage of the shift invariance of the analyzed configuration by carrying out appropriate integral transformations with respect to time and spatial coordinates. In order to take into account the property of causality of a pertaining wave field, the one-sided Laplace transformation with respect to time of a bounded physical quantity $f(x_1, t)$ is applied

$$\hat{f}(x_1, s) = \int_{t=0}^{\infty} \exp(-st) f(x_1, t) \mathrm{d}t \tag{1.5}$$

with *real and positive* transformation parameter s. This choice of the transformation parameter ensures the uniqueness of Eq. (1.5) by Lerch's theorem [27, 44]. The latter asserts that a causal function is uniquely given by its known Laplace transform specified

at the sequence of real s values $\{s_n \in \mathbb{R}; s_n = s_0 + nh, s_0 > 0, h > 0, n = 0, 1, 2, \dots\}$. As a consequence of the Laplace transformation and the vanishing initial conditions we have $\partial_t \to s$. From here on, the corresponding Laplace transformation counterpart is denoted by the circumflex over a symbol.

Subsequently, the unilateral Laplace transformation is combined with the slowness field representation that is capable of handling fields in an unbounded domain. The latter representation with respect to the spatial coordinate x_1 is given as

$$\hat{f}(x_1, s) = \frac{s}{2\pi \mathrm{i}} \int_{p=-\mathrm{i}\infty}^{\mathrm{i}\infty} \exp(-spx_1)\tilde{f}(p, s)\mathrm{d}p \tag{1.6}$$

involving imaginary values of the slowness parameter p along x_1, i.e. $p \in \mathbb{C}$ with $\mathrm{Re}(p) = 0$. As a consequence of the latter representation we have $\partial_1 \to -sp$. From here on, the corresponding wave slowness quantity is denoted by the tilde over a symbol.

Finally, in accordance with the international conventions, the physical quantities are expressed in SI units (International System of Units) [15].

1.4   Outline of the thesis

The analysis of the slot antennas effectuated throughout this thesis is based on the Maxwell's laws of macroscopic electromagnetic theory [23]. The electromagnetic field equations as applied throughout the thesis are briefly discussed in Chapter 2. The comprehensive survey of the subject can be found in [15, Part 3].

The main part of the thesis consists of seven chapters dealing with problems of increasing complexity. In view of consistency, each of these parts is treated at full length and can be regarded, to a certain extent, as a separate, self-contained account. Throughout the thesis we investigate the pulsed-field radiation behavior of a slot in an electrically perfectly conducting screen. The source exciting the structures is modeled as a prescribed distribution of the transverse electric field across the radiating slot.

Starting with a freestanding infinitesimal slot (line source) we gradually extend the problem complexity by inclusion an additional electrically conducting screen or a dielectric covering layer. Subsequently, we proceed to the more realistic radiator by considering a finite width of the slot. Again, the pulsed radiation from this slot is investigated in the presence of an electrically conducting screen or a dielectric layer. Finally, it is demonstrated how to deal with the spatially nonuniform distribution of the excitation, as occurs in the case of the modal excitation. For the sake of briefness, most of the chapters are suplemented by an Appendix, where the generic integral representation applying to the corresponding problem is solved. A number of numerical results that illustrate important features of corresponding wave phenomena are given.

Chapter 3 addresses the radiation properties of a slot of infinitesimal width in a two-dimensional configuration. The solution of the latter problem is solvable also in the frequency domain and can be found in the literature (see, for example [20]). In this part, the radiated pulsed fields are found via the Cagniard-DeHoop technique and also with the help of the corresponding scalar Green's function.

Chapter 4 can be considered as a generalization of the previous chapter and as a preparatory step for the next one. Here, the pulsed radiation from a narrow slot is investigated in the presence of a perfectly conducting screen that is placed above the slot. This chapter brings new features as the reflected wave constituents that occur on account of the additional screen.

Throughout Chapter 5, our considerations are aimed at the narrow slot antenna configuration covered by a dielectric slab. Thanks to the presence of the dielectric covering, the pertaining wave motion appears as the superposition of a number of propagating, reflecting, and refracting wave constituents. The exact solution of this problem can be found in [42] where the attention was focused on the evaluation of the field pulse shapes at dielectric/air interface. This has been extended here such that the closed-form expressions for radiated fields are given in the dielectric layer, at the dielectric/vacuum interface as well as in the vacuum half-space.

In the next chapters, the problem has been generalized by considering a finite slot width. A pulsed field radiation from a freestanding wide slot is investigated in Chapter 6. Here it is shown that the excitation via a wide slot shows additional features in that the corners of the waveguide feed show a separate diffractive behavior with accompanying wavefronts. The results of this chapter have been used for the description of pulsed radiation from a simple antenna array configuration [41].

Again, Chapter 7 can be considered as a certain generalization of the previous chapter and as a preparatory step for the next one. Here, the wide slot from Chapter 6 is analyzed in the presence of a perfectly conducting screen. It is shown that this additional screen causes reflections of diffractive and plane radiated wave fields.

Chapter 8 deals with the pulsed electromagnetic radiation from a wide slot that is covered by a dielectric layer [19]. On account of the presence of the dielectric slab, the pertaining wave motion appears as the superposition of a number of propagating, reflecting, and refracting wave constituents emanating from the corners of the feeding waveguide in addition to the plane wave propagating and reflecting above the radiating slot.

Finally, in Chapter 9 the problem of a nonuniform spatial distribution of an excitation field (as in the case of a modal excitation in the radiating aperture) is addressed. It is shown that the modal aperture excitation can be taken into account at the expense of having to evaluate an additional one-dimensional integral over a finite time-window.

In conclusion, the accomplishments of the thesis and the prospective aims are summarized.

Chapter 2

The electromagnetic field equations

Summary

In this chapter, the electromagnetic source-free field equations, as used throughout the thesis, are given. Since all problem configurations, as well as their excitation, are independent of one of the spatial coordinates, our starting equations take on a particular form that is derived here.

2.1   The basic equations

Throughout the thesis, the pulsed electromagnetic radiation from a two-dimensional slot antenna is evaluated (see Fig. 2.1). It is assumed that a radiating aperture $\mathcal{A} = \{-w/2 < x_1 < w/2, -\infty < x_2 < \infty, x_3 = 0\}$ of a width w (w is vanishing for a narrow slot antenna, w is finite for a wide slot antenna) is mounted on a perfectly electrically conducting screen $\mathcal{S} = \{(-\infty < x_1 < -w/2) \cup (w/2 < x_1 < \infty), -\infty < x_2 < \infty, x_3 = 0\}$ and radiates into a linear, time invariant, instantaneously and locally reacting, homogeneous and isotropic domain $\mathcal{D}$ described by its scalar electric permitivity ϵ and scalar magnetic permeability μ.

In this domain, the nonzero electromagnetic wave field quantities satisfy the electromagnetic field equations [15, Sec. 18.3]

$$-\boldsymbol{e}_{k,m,p}\partial_m H_p + \epsilon\partial_t E_k = 0 \tag{2.1}$$

$$\boldsymbol{e}_{j,n,r}\partial_n E_r + \mu\partial_t H_j = 0 \tag{2.2}$$

where $\boldsymbol{e}_{k,m,p}$ is the Levi-Civita tensor and

$$E_k = E_k(\boldsymbol{x}, t) \quad \text{is the electric field strength [V/m]},$$
$$H_p = H_p(\boldsymbol{x}, t) \quad \text{is the magnetic field strength [A/m]}.$$

The excited field quantities are causally related to the x_2-independent excitation E_1 field distribution on the radiating aperture

$$\lim_{x_3\downarrow 0} E_1(x_1, x_3, t) = [V_0(t)/w]\Omega(x_1)\Pi(x_1/w) \tag{2.3}$$
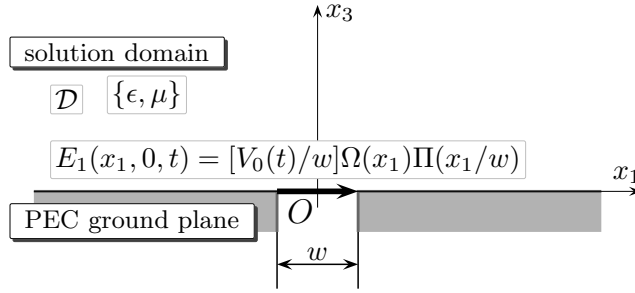
Figure 2.1: Generic configuration with indication of the aperture feeding.

for $t > 0$, $x_1 \in \mathbb{R}$. Here, $V_0(t)$ is a feeding pulse, $\Omega(x_1)$ describes a spatial distribution of an excitation field and $\Pi(x)$ is the rectangular function defined with the help of the Heaviside step function $H(x)$ as

$$\Pi(x) = H(x + 1/2) - H(x - 1/2) \tag{2.4}$$

On account of the problem configuration that is x_2-independent, the electromagnetic field equations can be written out in terms of their components as

$$\partial_3 H_2 + \epsilon \partial_t E_1 = 0 \tag{2.5}$$
$$-\partial_1 H_2 + \epsilon \partial_t E_3 = 0 \tag{2.6}$$
$$-\partial_1 E_3 + \partial_3 E_1 + \mu \partial_t H_2 = 0 \tag{2.7}$$

and

$$-\partial_3 E_2 + \mu \partial_t H_1 = 0 \tag{2.8}$$
$$\partial_1 E_2 + \mu \partial_t H_3 = 0 \tag{2.9}$$
$$\partial_1 H_3 - \partial_3 H_1 + \epsilon \partial_t H_2 = 0 \tag{2.10}$$

The Eqs. (2.5) – (2.7) interrelate $\{E_1, E_3, H_2\}(x_1, x_3, t)$ components (Transverse Magnetic, or TM, with respect to x_3) while the Eqs. (2.8) – (2.10) interrelate $\{H_1, H_3, E_2\}(x_1, x_3, t)$ components (Transverse Electric, or TE, with respect to x_3). Since the excitation is included in via the excitation condition (2.3) for pulsed E_1 field component, only the TM field components are nonzero.

Chapter 3

Pulsed electromagnetic field radiation from a narrow slot antenna

Summary

The pulsed electromagnetic field radiated by a 2D narrow slot antenna is analytically investigated via the application of the Cagniard-DeHoop technique. Starting with the description and formulation of the field problem we shall arrive at closed-form expressions describing the pulsed field radiation behavior of a narrow slot in an electrically perfectly conducting screen. Illustrative numerical results are given in Chapter 5, where a pulse distortion due to the presence of a dielectric slab is investigated.[1]

3.1 Introduction

This chapter aims at providing the description of the pulsed electromagnetic field radiation from a narrow slot in an unbounded perfectly electrically conducting (PEC) screen. The source is modeled as a prescribed distribution of the transverse electric field across the slot of a uniform and vanishing width. In fact, the problem configuration consists of the magnetic line source. The source further radiates into free space. Using the combination of a unilateral Laplace transformation with respect to time and the spatial slowness representation of the field components that is known as the Cagniard-DeHoop method, closed-form expressions are obtained for the electric and the magnetic field as a function of position and time. It is emphasized that the time-domain field expressions resulting from this section are well-known and is possible to derive them in a number of ways. In this respect, the electromagnetic field quantities are found via the application of the Cagniard-DeHoop technique and by means of the scalar Green's function of the wave equation.

Illustrative numerical results are given in Chapter 5, where a pulse distortion due to the presence of a dielectric slab is investigated.

3.2 Description of the configuration and formulation of the field problem

The configuration examined is shown in Fig. 3.1. The configuration consists of an unbounded electrically perfectly conducting screen $\mathcal{S} = \{(-\infty < x_1 < -w/2) \cup (w/2 < x_1 < \infty), -\infty < x_2 < \infty, x_3 = 0\}$ with a feeding aperture $\mathcal{A} = \{-w/2 < x_1 < w/2, -\infty < x_2 < \infty, x_3 = 0\}$ of the vanishing width $w \downarrow 0$. The structure radiates into the vacuum half-space $\mathcal{D}_0 = \{-\infty < x_1 < \infty, -\infty < x_2 < \infty, 0 < x_3 < \infty\}$ with vacuum electric permittivity and magnetic permeability $\{\epsilon_0, \mu_0\}$ and corresponding electromagnetic wave speed $c_0 = (\epsilon_0 \mu_0)^{-1/2}$.
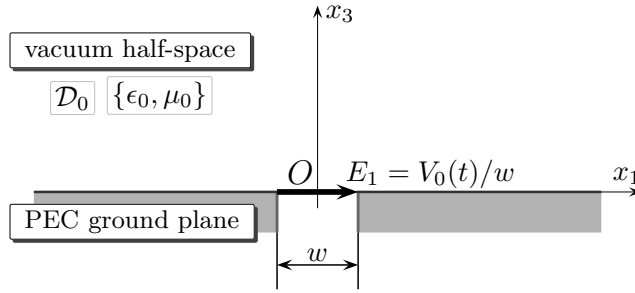

Figure 3.1: Configuration with indication of the aperture feeding.

The antenna aperture is fed by the uniformly distributed, x_2-independent, electric field

$$E_1(x_1, 0, t) = V_0(t)/w \quad \text{in } \mathcal{A} \tag{3.1}$$

where $V_0(t)$ is the feeding 'voltage'. Since the excitation, as well as the configuration, are independent of x_2, the non-zero components of the electric field strength $\{E_1, E_3\}(x_1, x_3, t)$ and the magnetic field strength $H_2(x_1, x_3, t)$ satisfy in $\mathcal{D}_0$ the source-free field equations (cf. Eqs. (2.5) – (2.7))

$$\partial_1 H_2 - \epsilon_0 \partial_t E_3 = 0 \tag{3.2}$$

$$\partial_3 H_2 + \epsilon_0 \partial_t E_1 = 0 \tag{3.3}$$

$$\partial_1 E_3 - \partial_3 E_1 - \mu_0 \partial_t H_2 = 0 \tag{3.4}$$

with the excitation condition (cf. Eq. (2.3))

$$\lim_{x_3 \downarrow 0} E_1(x_1, x_3, t) = V_0(t) \delta(x_1) \quad \text{for all } t \tag{3.5}$$

where $\delta(x)$ is Dirac's distribution. It is assumed that $V_0(t)$ starts to act at $t = 0$ and that prior to this instant the field vanishes throughout the configuration.

3.3   Field representations

In view of the Cagniard-DeHoop technique we employ the unilateral Laplace transformation with respect to time

$$\hat{V}_0(s) = \int_{t=0}^{\infty} \exp(-st)V_0(t)\mathrm{d}t \tag{3.6}$$

in which s is taken to be real-valued and positive relying on Lerch's theorem [27], [44]. Further we use the wave slowness field representation

$$\left\{\hat{E}_1, \hat{E}_3, \hat{H}_2\right\}(x_1, x_3, s) = \frac{s}{2\pi\mathrm{i}} \int_{p=-\mathrm{i}\infty}^{\mathrm{i}\infty} \exp(-spx_1)\left\{\tilde{E}_1, \tilde{E}_3, \tilde{H}_2\right\}(p, x_3, s)\mathrm{d}p \tag{3.7}$$

Under these transformations, the field equations (3.2) – (3.4) and the excitation condition (3.5) transform into

$$-sp\tilde{H}_2 - s\epsilon_0\tilde{E}_3 = 0 \tag{3.8}$$

$$\partial_3\tilde{H}_2 + s\epsilon_0\tilde{E}_1 = 0 \tag{3.9}$$

$$-sp\tilde{E}_3 - \partial_3\tilde{E}_1 - s\mu_0\tilde{H}_2 = 0 \tag{3.10}$$

and

$$\lim_{x_3\downarrow 0}\tilde{E}_1(p, x_3, s) = \hat{V}_0(s) \tag{3.11}$$

respectively. The bounded slowness-domain field quantities follow from (3.8) – (3.10) by expressing them in the form

$$\left\{\tilde{E}_1, \tilde{E}_3, \tilde{H}_2\right\}(p, x_3, s) = \{\gamma_0(p)/\epsilon_0, -p/\epsilon_0, 1\}\, A(p,s)\exp\left[-s\gamma_0(p)x_3\right] \quad \text{in } \mathcal{D}_0 \tag{3.12}$$

The unknown $A(p, s)$ results from the application of the excitation condition (3.11) as

$$A(p, s) = \epsilon_0\hat{V}_0(s)/\gamma_0(p) \tag{3.13}$$

3.4   The time-domain radiated fields

In this section we focus on the time-domain fields radiated into the vacuum halfspace $\mathcal{D}_0$. Using the results of Section 3.3 we express them as

$$\{\hat{E}_1, \hat{E}_3, \hat{H}_2\}(x_1, x_3, s) = \frac{s\hat{V}_0(s)}{2\pi\mathrm{i}} \int_{p=-\mathrm{i}\infty}^{\mathrm{i}\infty} \left\{1, -\frac{p}{\gamma_0(p)}, \frac{\epsilon_0}{\gamma_0(p)}\right\}\exp\{-s[px_1 + \gamma_0(p)x_3]\}\mathrm{d}p \tag{3.14}$$

The algebraic parts of the integrand do not contain any propagation coefficient that differs from the propagation coefficient $\gamma_0(p)$ in the propagation factor. This has the consequence that the corresponding Cagniard-DeHoop contour for a positive horizontal

offset intersects the real p-axis in between $p = 0$ and $p = 1/c_0$, implying the absence of head-waves. Following the recipe given in Appendix A for $c_0 = c_1$, the corresponding time-domain expressions in $\mathcal{D}_0$ can be found as

$$\{E_1, E_3, H_2\}(x_1, x_3, t) = \partial_t V_0(t) \overset{(t)}{*} \frac{1}{\pi} \left\{ \frac{x_3 t}{r^2}, -\frac{x_1 t}{r^2}, \epsilon_0 \right\} \frac{H(t - r/c_0)}{(t^2 - r^2/c_0^2)^{1/2}} \tag{3.15}$$

where $r = (x_1^2 + x_3^2)^{1/2} > 0$ and $E_1(x_1, 0, t) = V_0(t)\delta(x_1)$. The time-domain expressions can also be found from the solution of the source-free field equations (3.2) – (3.4) with (3.5) under the unilateral Laplace transformation. The solution is given as

$$\{\hat{E}_1, \hat{E}_3, \hat{H}_2\}(x_1, x_3, s) = \frac{s\hat{V}_0(s)}{\pi c_0} \left\{ \frac{x_3}{r} K_1(sr/c_0), -\frac{x_1}{r} K_1(sr/c_0), (\epsilon_0/\mu_0)^{1/2} K_0(sr/c_0) \right\} \tag{3.16}$$

where $K_{0,1}(x)$ are the modified Bessel functions of the second kind. Employing the inverse Laplace transformation of the modified Bessel functions $K_0(sr/c_0)$ and $K_1(sr/c_0)$

$$\frac{H(t - r/c_0)}{(t^2 - r^2/c_0^2)^{1/2}}, \quad \frac{c_0 t}{r} \frac{H(t - r/c_0)}{(t^2 - r^2/c_0^2)^{1/2}} \tag{3.17}$$

respectively, we arrive at the time-domain expressions (3.15). In the last example we express the electromagnetic field components in terms of the scalar fundamental solution of the wave equation

$$\{E_1, E_3, H_2\}(x_1, x_3, t) = V_0(t) \overset{(t)}{*} \{-\partial_3 G_0, \partial_1 G_0, \epsilon_0 \partial_t G_0\}(x_1, x_3, t) \tag{3.18}$$

where $G_0 = G_0(x_1, x_3, t)$ is a solution of the following problem in $\mathcal{D}_0$

$$(\partial_1^2 + \partial_3^2 - \partial_t^2/c_0^2)G_0 = 0$$
$$\lim_{x_3 \downarrow 0} \partial_3 G_0 = -\delta(t)\delta(x_1) \tag{3.19}$$

which is

$$G_0(x_1, x_3, t) = \begin{cases} \pi^{-1}(t^2 - r^2/c_0^2)^{-1/2} & \text{for } r/c_0 < t < \infty, \\ 0 & \text{for } 0 < t < r/c_0 \end{cases} \tag{3.20}$$

Carrying out the spatial differentiation introduced in (3.18) we arrive at

$$\{E_1, E_3\}(x_1, x_3, t) = V_0(t) \overset{(t)}{*} \frac{1}{\pi} \left\{ -\frac{x_3}{c_0^2}, \frac{x_1}{c_0^2} \right\} \frac{H(t - r/c_0)}{(t^2 - r^2/c_0^2)^{3/2}} \tag{3.21}$$

Noting that

$$\partial_t \left[t/(t^2 - r^2/c_0^2)^{1/2} \right] = -(r/c_0)^2/(t^2 - r^2/c_0^2)^{3/2} \tag{3.22}$$

then the application of integration by parts transforms expressions (3.18) into (3.15) again.

Chapter 4

Pulsed electromagnetic field radiation from a narrow slot antenna between two parallel planes

Summary

The pulsed electromagnetic field in between two parallel planes excited by a 2D narrow slot is analytically investigated via the application of the Cagniard-DeHoop technique. Starting with the description and formulation of the field problem we shall construct the exact pulse shapes for the radiated electromagnetic field components.

4.1   Introduction

The present chapter aims at providing the description of the pulsed electromagnetic field radiation from a narrow slot in an unbounded perfectly electrically conducting (PEC) screen. The source excited the structure is modeled as a prescribed distribution of the transverse electric field across the slot of a uniform and vanishing width. The structure further radiates into the domain in between two PEC parallel planes. If the upper plane is moved far away from the radiating slot, all reflected time-domain constituents become negligible and only upgoing radiated time-domain constituent is relevant. In this sense, the solved problem can be considered as a certain generalization of the problem described in Chapter 3.

Reflections occur due to the additional screen above the slot, and the slowness-domain quantities have to be written as a superposition of constituents, each of which admits a closed-form representation attainable with the Cagniard-DeHoop technique as described in Appendix A. It is shown that the wave motion consists of the set of upgoing and downgoing cylindrical waves emanating from the slot.

The problem solved in this chapter was studied by Schelkunoff in the frequency domain [36]. In it, electromagnetic waves between two parallel, perfectly electrically conducting screens are investigated with the aid of the 'Laplace transform method'. In view of the latter, the electromagnetic field in between the planes is excited by an a-c voltage applied

across the slot and the time dependence of electromagnetic field components is supressed by assuming $\exp(\mathrm{i}\omega t)$ time behavior. The excited electromagnetic field components are subsequently represented via the Bromwich contour inversion integral that is solved by means of the residue theorem.

The aproach presented in this chapter is somewhat more general in the sense that the electromagnetic field components are found in the space-time domain, without anticipation of the time-domain behavior of excited electromagnetic field. As the main tool, the combination of a unilateral Laplace transformation with the spatial wave slowness representation is used, which is known as the Cagniard-DeHoop technique.

4.2 Description of the configuration and formulation of the field problem

The configuration examined is shown in Fig. 4.1. The configuration consists of two unbounded electrically perfectly conducting screens $\mathcal{S}_1 = \{-\infty < x_1 < \infty, -\infty < x_2 < \infty, x_3 = h\}$ and $\mathcal{S}_2 = \{(-\infty < x_1 < -w/2) \cup (w/2 < x_1 < \infty), -\infty < x_2 < \infty, x_3 = 0\}$ with a feeding aperture $\mathcal{A} = \{-w/2 < x_1 < w/2, -\infty < x_2 < \infty, x_3 = 0\}$ of the vanishing width $w \downarrow 0$. The structure radiates into the domain $\mathcal{D} = \{-\infty < x_1 < \infty, -\infty < x_2 < \infty, 0 < x_3 < h\}$ with scalar electric permittivity and magnetic permeability $\{\epsilon, \mu\}$ and corresponding electromagnetic wave speed $c = (\epsilon\mu)^{-1/2}$.
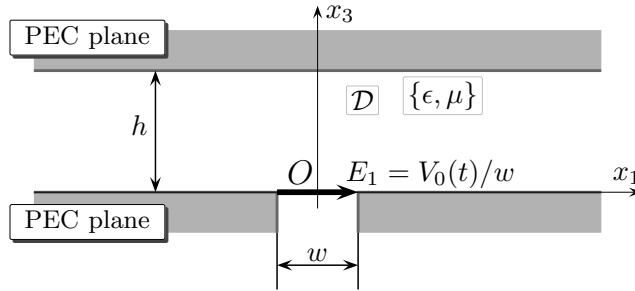

Figure 4.1: Configuration with indication of the aperture feeding.

The antenna aperture is fed by the uniformly distributed, x_2-independent, electric field

$$E_1(x_1, 0, t) = V_0(t)/w \quad \text{in } \mathcal{A} \tag{4.1}$$

where $V_0(t)$ is the feeding 'voltage'. Since the excitation, as well as the configuration, are independent of x_2, the non-zero components of the electric field strength $\{E_1, E_3\}(x_1, x_3, t)$ and the magnetic field strength $H_2(x_1, x_3, t)$ satisfy in $\mathcal{D}$ the source-free field equations (cf. Eqs. $(2.5) - (2.7)$)

$$\partial_1 H_2 - \epsilon \partial_t E_3 = 0 \tag{4.2}$$

$$\partial_3 H_2 + \epsilon \partial_t E_1 = 0 \tag{4.3}$$

$$\partial_1 E_3 - \partial_3 E_1 - \mu \partial_t H_2 = 0 \tag{4.4}$$

The boundary condition of the explicit type requires that

$$\lim_{x_3 \uparrow h} E_1(x_1, x_3, t) = 0 \quad \text{for all } t \text{ and for all } x_1 \tag{4.5}$$

while the excitation condition is (cf. Eq. (2.3))

$$\lim_{x_3 \downarrow 0} E_1(x_1, x_3, t) = V_0(t)\delta(x_1) \quad \text{for all } t \tag{4.6}$$

where $\delta(x)$ is Dirac's distribution. It is assumed that $V_0(t)$ starts to act at $t = 0$ and that prior to this instant the field vanishes throughout the configuration.

4.3 Field representations

In view of the Cagniard-DeHoop technique we employ the unilateral Laplace transformation with respect to time

$$\hat{V}_0(s) = \int_{t=0}^{\infty} \exp(-st)V_0(t)\mathrm{d}t \tag{4.7}$$

in which s is taken to be real-valued and positive relying on Lerch's theorem [27], [44]. Further we use the wave slowness field representation

$$\left\{\hat{E}_1, \hat{E}_3, \hat{H}_2\right\}(x_1, x_3, s) = \frac{s}{2\pi \mathrm{i}} \int_{p=-\mathrm{i}\infty}^{\mathrm{i}\infty} \exp(-spx_1)\left\{\tilde{E}_1, \tilde{E}_3, \tilde{H}_2\right\}(p, x_3, s)\mathrm{d}p \tag{4.8}$$

Under these transformations, the field equations (4.2) – (4.4) and the boundary conditions (4.5) – (4.6) transform into

$$-sp\tilde{H}_2 - s\epsilon\tilde{E}_3 = 0 \tag{4.9}$$
$$\partial_3\tilde{H}_2 + s\epsilon\tilde{E}_1 = 0 \tag{4.10}$$
$$-sp\tilde{E}_3 - \partial_3\tilde{E}_1 - s\mu\tilde{H}_2 = 0 \tag{4.11}$$

and

$$\lim_{x_3 \uparrow h} \tilde{E}_1(p, x_3, s) = 0 \tag{4.12}$$

$$\lim_{x_3 \downarrow 0} \tilde{E}_1(p, x_3, s) = \hat{V}_0(s) \tag{4.13}$$

The bounded slowness-domain field quantities follow from (4.9) – (4.13) by expressing them in the form

$$\left\{\tilde{E}_1, \tilde{E}_3, \tilde{H}_2,\right\}(p, x_3, s) = \{\gamma(p)/\epsilon, -p/\epsilon, 1\} A^+(p, s)\exp\left[-s\gamma(p)(x_3 - h)\right]$$
$$+ \{-\gamma(p)/\epsilon, -p/\epsilon, 1\} A^-(p, s)\exp\left[-s\gamma(p)(h - x_3)\right] \tag{4.14}$$

15

in which

$$\gamma(p) = (1/c^2 - p^2)^{1/2} \quad \text{with } \mathrm{Re}[\gamma(p)] > 0 \tag{4.15}$$

for all $p \in \mathbb{C}$. The unknown coefficients result from the application of boundary conditions (4.12) – (4.13) as

$$A^+(p,s) = A^-(p,s) = \frac{\epsilon}{\gamma(p)} \frac{\tilde{E}_1(p,0,s)}{\exp[s\gamma(p)h] - \exp[-s\gamma(p)h]} \tag{4.16}$$

Via the convergent expansion

$$\frac{\exp[s\gamma(p)h]}{\exp[s\gamma(p)h] - \exp[-s\gamma(p)h]} = \sum_{n=0}^{\infty} \exp[-2ns\gamma(p)h] \tag{4.17}$$

the slowness-domain field quantities can be written as the superposition of constituents each of which admits a closed-form representation attainable with Cagniard-DeHoop technique.

4.4   The time-domain radiated fields

In this section we provide the time-domain fields radiated into the domain $\mathcal{D}$. Using the results of Section 4.3 we express them as

$$\left\{ \hat{E}_1, \hat{E}_3, \hat{H}_2 \right\} (x_1, x_3, s) = \sum_{n=0}^{\infty} \left\{ \hat{E}_1^{[n]}, \hat{E}_3^{[n]}, \hat{H}_2^{[n]} \right\} (x_1, x_3, s) \tag{4.18}$$

with

$$
\begin{aligned}
&\left\{ \hat{E}_1^{[n]}, \hat{E}_3^{[n]}, \hat{H}_2^{[n]} \right\} (x_1, x_3, s) \\
&= \frac{s\hat{V}_0(s)}{2\pi\mathrm{i}} \int_{p=-\mathrm{i}\infty}^{\mathrm{i}\infty} \left\{ 1, -\frac{p}{\gamma(p)}, \frac{\epsilon}{\gamma(p)} \right\} \exp\{-s[px_1 + \gamma(p)Z_+]\}\mathrm{d}p \\
&+ \frac{s\hat{V}_0(s)}{2\pi\mathrm{i}} \int_{p=-\mathrm{i}\infty}^{\mathrm{i}\infty} \left\{ -1, -\frac{p}{\gamma(p)}, \frac{\epsilon}{\gamma(p)} \right\} \exp\{-s[px_1 + \gamma(p)Z_-]\}\mathrm{d}p
\end{aligned}
\tag{4.19}
$$

with $Z_+ = x_3 + 2nh$ and $Z_- = 2(n+1)h - x_3$. The algebraic parts of the integrands do not contain any propagation coefficient that differs from the propagation coefficient $\gamma(p)$ in the propagation factors. This has the consequence that the corresponding Cagniard-DeHoop contours for a positive horizontal offset intersect the real p-axis in between $p = 0$ and $p = 1/c$, implying the absence of head-waves. Following the recipe given in Appendix A for $c = c_0 = c_1$, the corresponding time-domain expressions in $\mathcal{D}$ can be found as

$$
\begin{aligned}
\left\{ E_1^{[n]}, E_3^{[n]}, H_2^{[n]} \right\} (x_1, x_3, t) &= \partial_t V_0(t) \overset{(t)}{*} \frac{1}{\pi} \left\{ \frac{Z_+ t}{x_1^2 + Z_+^2}, -\frac{x_1 t}{x_1^2 + Z_+^2}, \epsilon \right\} \frac{H(t - T_+)}{(t^2 - T_+^2)^{1/2}} \\
&+ \partial_t V_0(t) \overset{(t)}{*} \frac{1}{\pi} \left\{ -\frac{Z_- t}{x_1^2 + Z_-^2}, -\frac{x_1 t}{x_1^2 + Z_-^2}, \epsilon \right\} \frac{H(t - T_-)}{(t^2 - T_-^2)^{1/2}}
\end{aligned}
\tag{4.20}
$$

16

where

$$T_\pm = (x_1^2 + Z_\pm^2)^{1/2}/c. \tag{4.21}$$

Obviously, the wave motion consists of set of upgoing and downgoing time-domain constituents. In the limit $h \to \infty$, i.e. as the upper plane is moved towards infinity, the reflected time-domain constituents become negligible and only the zero-order upgoing constituent is relevant. This is consistent with the expressions (3.15) derived in the previous chapter.

Chapter 5

Pulsed electromagnetic field radiation from a narrow slot antenna with a dielectric layer

Summary

The pulsed electromagnetic field radiated by a 2D narrow slot antenna with a dielectric layer is analytically investigated via the application of the Cagniard-DeHoop technique. Starting with the description and formulation of the field problem we shall arrive at closed-form expressions describing the pulsed field radiation behavior of a narrow slot in an electrically perfectly conducting screen covered by a dielectric layer. In order to illustrate the pulse distortion that results from the presence of the dielectric slab, the results of this chapter shall be also compared with ones from Chapter 3. Illustrative numerical examples are given.[2]

5.1 Introduction

With the rapid development of communication systems whose operation is based upon the transfer of pulsed electromagnetic fields and the detection and subsequent interpretation of the pertaining digital signals, there is a need for the mathematical analysis of model configurations where the influence of (a number of) the system parameters on the performance shows up in closed-form analytic expressions that characterize the physical behavior. The present chapter aims at providing such a tool with regard to the pulsed radiation behavior of a narrow slot antenna covered with a dielectric layer in a two-dimensional setting.

The source exciting the structure is modeled as a prescribed distribution of the transverse electric field across a slot of uniform width in a perfectly electrically conducting (PEC) planar screen. The pulse shape of the exciting field is arbitrary. In front of this slotted plane there is a homogeneous, isotropic dielectric slab of uniform thickness. The

---

structure further radiates into free space. Using the combination of a unilateral Laplace transformation with respect to time and the spatial slowness representation of the field components that is known as the Cagniard-DeHoop method, closed-form expressions are obtained for the electric and the magnetic field as a function of position and time. The representation appears as the superposition of a number of propagating, reflecting and refracting wave constituents in the slab and is, within any finite time window of observation, exact. It is immediately clear that the pulse shapes of these constituents (that successively reach a receiving observer) are distorted versions of the time derivative of activating source signature. Parameters in this respect are: the pulse shape of the excitation (characterized by the pulse rise time and the pulse time width of a unipolar pulse), the thickness and the dielectric properties of the slab, as well as the position of observation relative to the exciting slot.

The exact description of the pulsed electromagnetic field behavior of this problem was published in [42]. In this paper, the attention was focused on the evaluation of the fields at the dielectric/air interface, which is sufficient for the evaluation of radiated fields into the vacuum half-space. This has been extended here such that the closed-form expressions for radiated fields are given in the dielectric layer, at the dielectric/vacuum interface as well as in the vacuum half-space. For the evaluation of the pulse shapes in the vacuum half-space, the parametrization of the Cagniard-DeHoop integration contour is carried out numerically via the iterative process described in Appendix D. The last section provides a number of illustrative numerical examples and is divided into three subsections. At first, numerical examples that illustrate the distortion of pulse shapes (of continuous components across the interface) at the vacuum/dielectric interface due to the presence of a dielectric layer are given. The next subsection shows the pulse shapes (of component that jumps across the interface) just below and above the vacuum/dielectric interface. Finally, the time-evolution of the Poynting vector in the dielectric layer, dielectric/vacuum interface and in vacuum is given. This example is further supplemented with the illustration of Cagniard-DeHoop paths connected with the observation point in the vacuum half-space for the first two wave constituents.

In the case of vanishing contrast (in electromagnetic properties) between the dielectric slab and free-space, obtained results become identical with ones given in Chapter 3. In this sense, the solved problem can be considered as a certain generalization of the problem described Chapter 3.

5.2 Description of the configuration and formulation of the field problem

The configuration examined is shown in Fig. 5.1. The configuration consists of an unbounded electrically perfectly conducting screen $\mathcal{S} = \{(-\infty < x_1 < -w/2) \cup (w/2 < x_1 < \infty), -\infty < x_2 < \infty, x_3 = 0\}$ with a feeding aperture $\mathcal{A} = \{-w/2 < x_1 < w/2, -\infty < x_2 < \infty, x_3 = 0\}$ of the vanishing width $w \downarrow 0$. The covering dielectric slab occupies the domain $\mathcal{D}_1 = \{-\infty < x_1 < \infty, -\infty < x_2 < \infty, 0 < x_3 < d\}$. The structure radiates into the vacuum half-space $\mathcal{D}_0 = \{-\infty < x_1 < \infty, -\infty < x_2 < \infty, d < x_3 < \infty\}$. The spatial
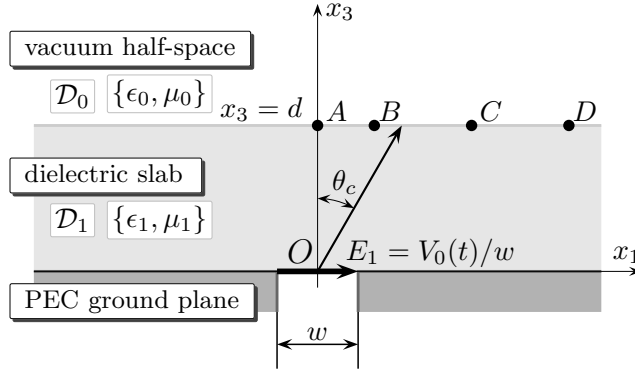
Figure 5.1: Configuration with indication of the critical angle $\theta_c = \arcsin(c_1/c_0)$. Positions of the observation points $\{B, C, D\}$ are not true-to-scale with those chosen in Section 5.7.1.

distribution of electric permittivity and magnetic permeability is

$$\{\epsilon, \mu\} = \begin{cases} \{\epsilon_0, \mu_0\} & \text{in } \mathcal{D}_0 \\ \{\epsilon_1, \mu_1\} & \text{in } \mathcal{D}_1 \end{cases} \tag{5.1}$$

The corresponding electromagnetic wave speeds are $c_0 = (\epsilon_0\mu_0)^{-1/2}$ and $c_1 = (\epsilon_1\mu_1)^{-1/2}$.

The antenna aperture is fed by the uniformly distributed, x_2-independent, electric field

$$E_1(x_1, 0, t) = V_0(t)/w \quad \text{in } \mathcal{A} \tag{5.2}$$

where $V_0(t)$ is the feeding 'voltage'. Since the excitation, as well as the configuration, are independent of x_2, the non-zero components of the electric field strength $\{E_1, E_3\}(x_1, x_3, t)$ and the magnetic field strength $H_2(x_1, x_3, t)$ satisfy in $\mathcal{D}_0$ and $\mathcal{D}_1$ the source-free field equations (cf. Eqs. (2.5) – (2.7))

$$\partial_1 H_2 - \epsilon \partial_t E_3 = 0 \tag{5.3}$$

$$\partial_3 H_2 + \epsilon \partial_t E_1 = 0 \tag{5.4}$$

$$\partial_1 E_3 - \partial_3 E_1 - \mu \partial_t H_2 = 0 \tag{5.5}$$

The interface boundary conditions require that

$$\lim_{x_3 \downarrow d} E_1(x_1, x_3, t) = \lim_{x_3 \uparrow d} E_1(x_1, x_3, t) \quad \text{for all } x_1 \text{ and } t \tag{5.6}$$

$$\lim_{x_3 \downarrow d} H_2(x_1, x_3, t) = \lim_{x_3 \uparrow d} H_2(x_1, x_3, t) \quad \text{for all } x_1 \text{ and } t \tag{5.7}$$

while the excitation condition is (cf. Eq. (2.3))

$$\lim_{x_3 \downarrow 0} E_1(x_1, x_3, t) = V_0(t)\delta(x_1) \quad \text{for all } t \tag{5.8}$$

as $w \downarrow 0$ with $\delta(x)$ denoting Dirac's distribution. It is assumed that $V_0(t)$ starts to act at $t = 0$ and that prior to this instant the field vanishes throughout the configuration.

5.3 Field representations

The Cagniard-DeHoop technique employs a unilateral Laplace transformation with respect to time of the type

$$\hat{V}_0(s) = \int_{t=0}^{\infty} \exp(-st) V_0(t) \mathrm{d}t \tag{5.9}$$

in which s is taken to be real-valued and positive relying on Lerch's theorem [27, 44]. The next step is to use the slowness representation of the field quantities

$$\left\{ \hat{E}_1, \hat{E}_3, \hat{H}_2 \right\} (x_1, x_3, s) = \frac{s}{2\pi \mathrm{i}} \int_{p=-\mathrm{i}\infty}^{\mathrm{i}\infty} \exp(-spx_1) \left\{ \tilde{E}_1, \tilde{E}_3, \tilde{H}_2 \right\} (p, x_3, s) \mathrm{d}p \tag{5.10}$$

that involves imaginary values of the complex slowness parameter p. Using (5.9) and (5.10), the field equations (5.3)–(5.5) transform into

$$-sp\tilde{H}_2 - s\epsilon \tilde{E}_3 = 0 \tag{5.11}$$

$$\partial_3 \tilde{H}_2 + s\epsilon \tilde{E}_1 = 0 \tag{5.12}$$

$$-sp\tilde{E}_3 - \partial_3 \tilde{E}_1 - s\mu \tilde{H}_2 = 0 \tag{5.13}$$

the interface boundary conditions (5.6) and (5.7) into

$$\lim_{x_3 \downarrow d} \tilde{E}_1(p, x_3, s) = \lim_{x_3 \uparrow d} \tilde{E}_1(p, x_3, s) \tag{5.14}$$

$$\lim_{x_3 \downarrow d} \tilde{H}_2(p, x_3, s) = \lim_{x_3 \uparrow d} \tilde{H}_2(p, x_3, s) \tag{5.15}$$

and the excitation condition (5.8) into

$$\lim_{x_3 \downarrow 0} \tilde{E}_1(p, x_3, s) = \hat{V}_0(s) \tag{5.16}$$

The slowness-domain field quantities follow from (5.11) – (5.16) by expressing them in the form

$$\left\{ \tilde{E}_1, \tilde{E}_3, \tilde{H}_2 \right\} (p, x_3, s) = \left\{ \gamma_0(p)/\epsilon_0, -p/\epsilon_0, 1 \right\} A_0^+(p, s) \exp\left[-s\gamma_0(p)(x_3 - d) \right] \quad \text{in } \mathcal{D}_0 \tag{5.17}$$

and

$$\left\{ \tilde{E}_1, \tilde{E}_3, \tilde{H}_2 \right\} (p, x_3, s) = \left\{ \gamma_1(p)/\epsilon_1, -p/\epsilon_1, 1 \right\} A_1^+(p, s) \exp\left[-s\gamma_1(p)x_3 \right]$$
$$+ \left\{ -\gamma_1(p)/\epsilon_1, -p/\epsilon_1, 1 \right\} A_1^-(p, s) \exp\left[-s\gamma_1(p)(d - x_3) \right] \quad \text{in } \mathcal{D}_1 \tag{5.18}$$

in which

$$\gamma_{0,1}(p) = \left(1/c_{0,1}^2 - p^2 \right)^{1/2} \quad \text{with } \mathrm{Re}\left[\gamma_{0,1}(p) \right] > 0 \quad \text{for all } p \in \mathbb{C} \tag{5.19}$$

21

Using these expressions in (5.14) – (5.16) it is found that

$$A_1^+(p, s) = \frac{\epsilon_1}{\gamma_1(p)} \frac{\hat{V}_0(s)}{\Delta} \tag{5.20}$$

$$A_1^-(p, s) = \frac{\epsilon_1}{\gamma_1(p)} R_H(p) \frac{\hat{V}_0(s) \exp[-s\gamma_1(p)d]}{\Delta} \tag{5.21}$$

$$A_0^+(p, s) = \frac{\epsilon_1}{\gamma_1(p)} T_H(p) \frac{\hat{V}_0(s) \exp[-s\gamma_1(p)d]}{\Delta} \tag{5.22}$$

in which

$$R_H(p) = \frac{\gamma_1(p)/\epsilon_1 - \gamma_0(p)/\epsilon_0}{\gamma_1(p)/\epsilon_1 + \gamma_0(p)/\epsilon_0} \tag{5.23}$$

$$T_H(p) = \frac{2\,\gamma_1(p)/\epsilon_1}{\gamma_1(p)/\epsilon_1 + \gamma_0(p)/\epsilon_0} \tag{5.24}$$

$$\Delta = 1 - R_H(p) \exp[-2s\gamma_1(p)d] \tag{5.25}$$

Via the convergent expansion

$$\frac{1}{\Delta} = \sum_{n=0}^{\infty} [R_H(p)]^n \exp[-2snd\gamma_1(p)] \tag{5.26}$$

the slowness-domain field quantities can be written as the superposition of constituents each of which admits a closed-form representation attainable with Cagniard-DeHoop method

$$\left\{ \hat{E}_1, \hat{E}_3, \hat{H}_2 \right\}(x_1, x_3, s) = \sum_{n=0}^{\infty} \left\{ \hat{E}_1^{[n]}, \hat{E}_3^{[n]}, \hat{H}_2^{[n]} \right\}(x_1, x_3, s) \tag{5.27}$$

5.4   The time-domain field in the dielectric layer

In this section we focus on the time-domain constituents of the fields components propagating in the dielectric slab $\mathcal{D}_1$. Using the results of Section 5.3 we express them as

$$\begin{aligned}
\left\{ \hat{E}_1^{[n]}, \hat{E}_3^{[n]}, \hat{H}_2^{[n]} \right\}(x_1, x_3, s) &= \frac{s\hat{V}_0(s)}{2\pi i} \int_{p=-i\infty}^{i\infty} \left\{ 1, -\frac{p}{\gamma_1(p)}, \frac{\epsilon_1}{\gamma_1(p)} \right\} [R_H(p)]^n \\
&\quad \times \exp\{-s[px_1 + \gamma_1(p)Z_+]\} dp \\
&\quad + \frac{s\hat{V}_0(s)}{2\pi i} \int_{p=-i\infty}^{i\infty} \left\{ -1, -\frac{p}{\gamma_1(p)}, \frac{\epsilon_1}{\gamma_1(p)} \right\} [R_H(p)]^{n+1} \\
&\quad \times \exp\{-s[px_1 + \gamma_1(p)Z_-]\} dp
\end{aligned} \tag{5.28}$$

where $Z_+ = x_3 + 2nd$, $Z_- = 2(n+1)d - x_3$. Obviously, the expressions represent sets of upgoing and downgoing waves. The latter waves, as well as subsequent reflected upgoing waves, disappear as the contrast in electromagnetic properties between $\mathcal{D}_0$ and $\mathcal{D}_1$ vanishes. Since the propagation terms in (5.28) do not contain the propagation coefficient

$\gamma_0(p)$, which, for the standard case $c_0 > c_1$, implies the possible occurence of head-waves. The corresponding time-domain expressions of each of these constituents follow upon the application of the Cagniard-DeHoop technique as described in Appendix A. In this way, the body-wave time-domain constituents can be written as

$$
\left\{ E_1^{\mathrm{BW};[n]}, E_3^{\mathrm{BW};[n]}, H_2^{\mathrm{BW};[n]} \right\} (x_1, x_3, t) = \partial_t V_0(t) \overset{(t)}{*} \pi^{-1}
$$
$$
\times \left\{ \mathrm{Re} \left(\left\{ \gamma_1 \left(p^{\mathrm{BW}+} \right), -p^{\mathrm{BW}+}, \epsilon_1 \right\} \left[R_H \left(p^{\mathrm{BW}+} \right) \right]^n \right) H \left(t - T_{\mathrm{BW}+}^{[n]} \right) \left(t^2 - T_{\mathrm{BW}+}^{[n]2} \right)^{-1/2} \right.
$$
$$
+ \mathrm{Re} \left(\left\{ -\gamma_1 \left(p^{\mathrm{BW}-} \right), -p^{\mathrm{BW}-}, \epsilon_1 \right\} \left[R_H \left(p^{\mathrm{BW}-} \right) \right]^{n+1} \right)
$$
$$
\left. \times H \left(t - T_{\mathrm{BW}-}^{[n]} \right) \left(t^2 - T_{\mathrm{BW}-}^{[n]2} \right)^{-1/2} \right\} \tag{5.29}
$$

where $p^{\mathrm{BW}\pm} = p^{\mathrm{BW}\pm}(x_1, Z_\pm, t)$ is given as

$$
p^{\mathrm{BW}\pm} = \left\{ x_1 t + \mathrm{i} Z_\pm \left(t^2 - T_{\mathrm{BW}\pm}^{[n]2} \right)^{1/2} \right\} / \left\{ x_1^2 + Z_\pm^2 \right\} \tag{5.30}
$$

with

$$
T_{\mathrm{BW}\pm}^{[n]} = (x_1^2 + Z_\pm^2)^{1/2}/c_1 \tag{5.31}
$$

In the range where $x_1/(x_1^2 + Z_\pm^2)^{1/2} > c_1/c_0$ is satisfied, the head-wave time-domain constituents are present

$$
\left\{ E_1^{\mathrm{HW};[n]}, E_3^{\mathrm{HW};[n]}, H_2^{\mathrm{HW};[n]} \right\} (x_1, x_3, t) = \partial_t V_0(t) \overset{(t)}{*} \pi^{-1}
$$
$$
\times \left\{ \mathrm{Im} \left(\left\{ \gamma_1 \left(p^{\mathrm{HW}+} \right), -p^{\mathrm{HW}+}, \epsilon_1 \right\} \left[R_H \left(p^{\mathrm{HW}+} \right) \right]^n \right) \Pi \left[\left(t - T_{\mathrm{C}+}^{[n]} \right) / T_{\mathrm{L}+}^{[n]} \right] \left(T_{\mathrm{BW}+}^{[n]2} - t^2 \right)^{-1/2} \right.
$$
$$
+ \mathrm{Im} \left(\left\{ -\gamma_1 \left(p^{\mathrm{HW}-} \right), -p^{\mathrm{HW}-}, \epsilon_1 \right\} \left[R_H \left(p^{\mathrm{HW}-} \right) \right]^{n+1} \right)
$$
$$
\left. \times \Pi \left[\left(t - T_{\mathrm{C}-}^{[n]} \right) / T_{\mathrm{L}-}^{[n]} \right] \left(T_{\mathrm{BW}-}^{[n]2} - t^2 \right)^{-1/2} \right\} \tag{5.32}
$$

where $\Pi(x)$ denotes the rectangular function and $p^{\mathrm{HW}\pm} = p^{\mathrm{HW}\pm}(x_1, Z_\pm, t)$ is given as

$$
p^{\mathrm{HW}\pm} = \left\{ x_1 t - Z_\pm \left(T_{\mathrm{BW}\pm}^{[n]2} - t^2 \right)^{1/2} \right\} / \left\{ x_1^2 + Z_\pm^2 \right\} \tag{5.33}
$$

with

$$
T_{\mathrm{HW}\pm}^{[n]} = x_1/c_0 + Z_\pm \left(1/c_1^2 - 1/c_0^2 \right)^{1/2} \tag{5.34}
$$
$$
T_{\mathrm{C}\pm}^{[n]} = \left(T_{\mathrm{HW}\pm}^{[n]} + T_{\mathrm{BW}\pm}^{[n]} \right) /2 \tag{5.35}
$$
$$
T_{\mathrm{L}\pm}^{[n]} = T_{\mathrm{BW}\pm}^{[n]} - T_{\mathrm{HW}\pm}^{[n]} \tag{5.36}
$$

5.5 The time-domain field at the vacuum/dielectric interface

In this section we focus on those field components at the interface $x_3 = d$ that are continuous across this interface, i.e. E_1 and H_2. In fact, the radiated field in $\mathcal{D}_0$ can be easily expressed in terms of these field values. Using the results o f Section 5.3 we express them as

$$\left\{ \hat{E}_1^{[n]}, \hat{H}_2^{[n]} \right\} (x_1, d, s) = \frac{s\hat{V}_0(s)}{2\pi\mathrm{i}} \int_{p=-\mathrm{i}\infty}^{\mathrm{i}\infty} \left\{ \frac{\epsilon_1 \gamma_0(p)}{\epsilon_0 \gamma_1(p)}, \frac{\epsilon_1}{\gamma_1(p)} \right\} T_H(p) [R_H(p)]^n$$
$$\times \exp\{-s[px_1 + \gamma_1(p)(2n+1)d]\}\mathrm{d}p \tag{5.37}$$

Since the propagation terms in (5.37) do not contain the propagation coefficient $\gamma_0(p)$, which for the standard case $c_0 > c_1$, implies the possible occurence of head-waves. The corresponding time-domain expressions of each of these constituents follow upon the application of the Cagniard-DeHoop technique given in Appendix A. In this way, the body-wave time-domain constituents can be written as

$$\left\{ E_1^{\mathrm{BW};[n]}, H_2^{\mathrm{BW};[n]} \right\} (x_1, d, t) = \partial_t V_0(t) \overset{(t)}{*} \pi^{-1}\mathrm{Re}\Big(\left\{ \epsilon_1 \gamma_0 \left(p^{\mathrm{BW}} \right) / \epsilon_0, \epsilon_1 \right\} T_H \left(p^{\mathrm{BW}} \right)$$
$$\times \left[R_H \left(p^{\mathrm{BW}} \right) \right]^n \Big) H \left(t - T_{\mathrm{BW}}^{[n]} \right) \left(t^2 - T_{\mathrm{BW}}^{[n]2} \right)^{-1/2} \tag{5.38}$$

where $p^{\mathrm{BW}} = p^{\mathrm{BW}}[x_1, (2n+1)d, t]$ is given as

$$p^{\mathrm{BW}} = \left\{ x_1 t + \mathrm{i}(2n+1)d \left(t^2 - T_{\mathrm{BW}}^{[n]2} \right)^{1/2} \right\} / \left\{ x_1^2 + [(2n+1)d]^2 \right\} \tag{5.39}$$

with

$$T_{\mathrm{BW}}^{[n]} = \left\{ x_1^2 + [(2n+1)d]^2 \right\}^{1/2} / c_1 \tag{5.40}$$

In the range where $x_1/\{x_1^2 + [(2n+1)d]^2\}^{1/2} > c_1/c_0$ is satisfied, the head-wave time-domain constituents are present

$$\left\{ E_1^{\mathrm{HW};[n]}, H_2^{\mathrm{HW};[n]} \right\} (x_1, d, t) = \partial_t V_0(t) \overset{(t)}{*} \pi^{-1}\mathrm{Im}\Big(\left\{ \epsilon_1 \gamma_0 \left(p^{\mathrm{HW}} \right) / \epsilon_0, \epsilon_1 \right\} T_H \left(p^{\mathrm{HW}} \right)$$
$$\times \left[R_H \left(p^{\mathrm{HW}} \right) \right]^n \Big) \Pi \left[\left(t - T_{\mathrm{C}}^{[n]} \right) / T_{\mathrm{L}}^{[n]} \right] \left(T_{\mathrm{BW}}^{[n]2} - t^2 \right)^{-1/2}$$
$$\tag{5.41}$$

where $p^{\mathrm{HW}} = p^{\mathrm{HW}}[x_1, (2n+1)d, t]$ is given as

$$p^{\mathrm{HW}} = \left\{ x_1 t - (2n+1)d \left(T_{\mathrm{BW}}^{[n]2} - t^2 \right)^{1/2} \right\} / \left\{ x_1^2 + [(2n+1)d]^2 \right\} \tag{5.42}$$

with

$$T_{\mathrm{HW}}^{[n]} = x_1/c_0 + (2n+1)d \left(1/c_1^2 - 1/c_0^2 \right)^{1/2} \tag{5.43}$$
$$T_{\mathrm{C}}^{[n]} = \left(T_{\mathrm{HW}}^{[n]} + T_{\mathrm{BW}}^{[n]} \right) /2 \tag{5.44}$$
$$T_{\mathrm{L}}^{[n]} = T_{\mathrm{BW}}^{[n]} - T_{\mathrm{HW}}^{[n]} \tag{5.45}$$

5.6 The time-domain field in the vacuum

In this section we focus on the time-domain constituents of the fields radiated into the vacuum halfspace $\mathcal{D}_0$. Using the results of Section 5.3 we express them as

$$\left\{ \hat{E}_1^{[n]}, \hat{E}_3^{[n]}, \hat{H}_2^{[n]} \right\}(x_1, x_3, s) = \frac{s\hat{V}_0(s)}{2\pi\mathrm{i}} \int_{p=-\mathrm{i}\infty}^{\mathrm{i}\infty} \left\{ \frac{\epsilon_1\gamma_0(p)}{\epsilon_0\gamma_1(p)}, -\frac{\epsilon_1 p}{\epsilon_0\gamma_1(p)}, \frac{\epsilon_1}{\gamma_1(p)} \right\} T_H(p)[R_H(p)]^n$$
$$\times \exp\{-s[px_1 + \gamma_0(p)(x_3 - d) + \gamma_1(p)(2n+1)d]\}\mathrm{d}p \quad (5.46)$$

The propagation terms as well as the algebraic part of the integrands now contain both propagation coefficients $\gamma_0(p)$ and $\gamma_1(p)$. This has the consequence that the body-wave part of the Cagniard-DeHoop contour intersects the real p-axis between $p = 0$ and $p = 1/c_0$, implying the absence of head-wave constituents in $\mathcal{D}_0$. Note that, in this case, the Cagniard-DeHoop contour does not have a simple parametrization and has to be determined either algebraically via Cardano's formula or via the iterative numerical procedure as described in Appendix D. Once the iterative procedure is terminated, the corresponding time-domain body-wave expressions of each of these constituents result from the procedure as applied in Sections 5.4 and 5.5, i.e.

$$\left\{ E_1^{\mathrm{BW};[n]}, E_3^{\mathrm{BW};[n]}, H_2^{\mathrm{BW};[n]} \right\}(x_1, x_3, t) = \partial_t V_0(t) \overset{(t)}{*} \pi^{-1}$$
$$\times \mathrm{Im}\left(\left\{ \frac{\epsilon_1\gamma_0(p^{\mathrm{BW}})}{\epsilon_0\gamma_1(p^{\mathrm{BW}})}, -\frac{\epsilon_1 p^{\mathrm{BW}}}{\epsilon_0\gamma_1(p^{\mathrm{BW}})}, \frac{\epsilon_1}{\gamma_1(p^{\mathrm{BW}})} \right\} T_H\left(p^{\mathrm{BW}}\right) \left[R_H\left(p^{\mathrm{BW}}\right)\right]^n \partial_t p^{\mathrm{BW}} \right)$$
$$\times H\left(t - T_{\mathrm{BW}}^{[n]}\right) \quad (5.47)$$

where $p^{\mathrm{BW}}(\tau)$ results from solving $\tau = px_1 + \gamma_0(p)(x_3 - d) + \gamma_1(p)(2n+1)d$ such that $\tau \in \mathbb{R}$, $\tau > 0$. The examples of corresponding Cagniard-DeHoop contours are given in Sec. 5.7.3.

5.7 Illustrative numerical examples

This section provides illustrative numerical results for the case of excitation with the power exponential signature with $\nu = 2$ ($t_w/t_r = 1.8473$), as shown in Fig. 5.2a. Fig. 5.2b shows its spectral diagram. In them, the normalized $V_0(t)$ is $V_0(t)/V_{\max}$, the normalized time is t/t_r, the normalized $\hat{V}_0(\mathrm{i}\omega)$ is $\hat{V}_0(\mathrm{i}\omega)/\hat{V}_0(0)$ and the normalized angular frequency is $\omega/\omega_{\mathrm{corner}}$. This activating source signature is used throughout this section.

The rise time of the excitation pulse t_r is taken as half of the free-space travel time across the slab. As described in Appendix E, the pulse time width t_w is related to the pulse rise time t_r via (E.3), which gives $c_0 t_w/d = 0.9236$ for $\nu = 2$. The properties of the slab are taken as $\{\epsilon_1, \mu_1\} = \{4\epsilon_0, \mu_0\}$.

The first part of this section shows pulse shapes of $\{E_1, H_2\}(x_1, d, t)$ at the level of vacuum/dielectric interface, while the second part provides pulse shapes of $E_3(x_1, x_3, t)$ just below and above the interface, across which it jumps. The third subsection gives the time evolution of the Poynting vector within a certain region of space at two successive observation times. The last part is supplemented by examples of Cagniard-DeHoop contours associated with the evaluation of pulse shapes in the vacuum.

All time convolution integrals contain inverse square-root singularities at one of the end-points of the integrals. These are numerically handled via a stretching of the variable of integration according to

$$\tau = T_{\text{BW}}^{[n]} \cosh(u) \quad \text{for } 0 < u < \infty \tag{5.48}$$

with the Jacobian

$$\frac{\partial \tau}{\partial u} = T_{\text{BW}}^{[n]} \sinh(u) = \left(\tau^2 - T_{\text{BW}}^{[n]2} \right)^{1/2} \tag{5.49}$$

for a body-wave constituent with arrival time $T_{\text{BW}}^{[n]}$ and

$$\tau = T_{\text{BW}}^{[n]} \cos(v) \quad \text{for } 0 < v < \pi/2 \tag{5.50}$$

with the Jacobian

$$\frac{\partial \tau}{\partial v} = -T_{\text{BW}}^{[n]} \sin(v) = - \left(T_{\text{BW}}^{[n]2} - \tau^2 \right)^{1/2} \tag{5.51}$$

for a head-wave constituent. The integration limits at the time convolution integrals are subsequently adjusted to the corresponding intervals in u and v.

5.7.1 Examples of pulse shapes at the vacuum/dielectric interface

In any finite time window of observation, only a finite number of time-domain constituents yields a non-zero contribution, while in the range of critical refraction only a subset of these contributions have a head-wave part. The objective of our analysis is to compare the pulse shapes of the different constituents with the ones that the slot antenna would radiate into a half-space with the properties of $\mathcal{D}_0$. This comparison is carried out on the vacuum/dielectric interface.

Four positions of observation at $x_3 = d$ have been selected: (A) $x_1/d = 0$, (B) $x_1/d = 0.5$, (C) $x_1/d = 2.8$, (D) $x_1/d = 5.0$. In accordance with Fig. 5.1, only the last two observation points are in the range of critical refraction. The time window of observation is taken as $0 < c_0 t/d < 20$. The arrival times of the different contributions are shown in Table 5.1.

Figs. 5.3 – 5.6 show the results. In them, the normalized E_1 is $E_1 d/V_{\text{max}}$, the normalized H_2 is $(\mu_0/\epsilon_0)^{1/2} H_2 d/V_{\text{max}}$, the normalized time is $c_0 t/d$. The successive reflections at the interface clearly show up. Especially in the ranges where head-wave contributions occur, the total pulse shape significantly deviates from the one that is excited at the radiating slot.

5.7.2 Examples of pulse shapes just below and above the vacuum/dielectric interface

For the observation of pulse shapes of the electric field component $E_3(x_1, x_3, t)$, six observation points below and above the points (B), (C) and (D) at vertical levels $x_3/d =$

Table 5.1: Arrival times of constituents at the vacuum/dielectric interface.

order	A	B	C	D	A	B	C	D
	Arrival times							
	Head-wave				Body-wave			
$[n]$	$c_0 T_{\mathrm{HW}}^{[n]}/d$				$c_0 T_{\mathrm{BW}}^{[n]}/d$			
0	-	-	4.5321	6.7231	2.0	2.2361	5.9464	10.1980
1	-	-	7.9962	10.1962	6.0	6.0828	8.2073	11.6619
2	-	-	-	13.6603	10.0	10.0499	11.4612	14.1421
3	-	-	-	17.1244	14.0	14.0357	15.0785	17.2047
4	-	-	-	-	18.0	18.0278	18.8510	-

$0.995, 1.005$ have been chosen. The corresponding points just below the interface are labeled with $\uparrow$ and the points just above the interface with $\downarrow$.

In the plots, the normalized time is $c_0 t/d$ and the normalized E_3 stands for $E_3 w/V_{\mathrm{max}}$. Figures 5.7 – 5.9 exhibit the jump in magnitude that is related to the electric contrast ratio $\epsilon_1/\epsilon_0 = 4$. The arrival times corresponding to the pulse shapes in the dielectric layer and in the vacuum are summarized in Tables 5.2 and 5.3, respectively.

5.7.3   Time evolution of the Poynting vector

In the (color) vector density plots we show the time evolution of two-component Poynting vector

$$S_1 = -E_3 H_2 \tag{5.52}$$
$$S_3 = E_1 H_2 \tag{5.53}$$

normalized with respect to

$$|\boldsymbol{S}|_{\mathrm{ref}} = (V_{\mathrm{max}}/d)^2 (\epsilon_0/\mu_0)^{1/2} \tag{5.54}$$

The spatial domain of observation is taken as $\{-3 \leq x_1/d \leq 3, 0 \leq x_3/d \leq 3\}$ and two observation times are chosen as: $c_0 t/d = \{2, 4\}$.

In Fig. 5.10a the cylindrical wavefront just reaches the vacuum/dielectric interface at $c_0 t/d = 2$. Fig. 5.10b illustrates the spatial distribution of the Poynting vector at $c_0 t/d = 4$. At the latter observation time, the reflected wave time-domain constituents and the head-wave time-domain constituents beyond the critical refraction limit are clearly visible.

At two points inside the spatial observation region, the Cagniard-DeHoop paths have been evaluted for the first two successive time-domain constituents $n = \{0, 1\}$. The time-window has been taken as $T_{\mathrm{BW}} \leq c_0 t/d \leq 20$. Fig. 5.11 shows the first quadrant of p-plane with the corresponding Cagniard-DeHoop paths at $x_1 = 0.5d$, $x_3 = 2d$ while Fig. 5.12 shows the Cagniard-DeHoop paths for the observation point at $x_1 = 2.8d$, $x_3 = 2d$.

Table 5.2: Arrival times of constituents in the dielectric slab.

Arrival times						
	Head-wave (upgoing)			Body-wave (upgoing)		
order	$c_0 T_{\mathrm{HW}+}^{[n]}/d$			$c_0 T_{\mathrm{BW}+}^{[n]}/d$		
$[n]$	↑B	↑C	↑D	↑B	↑C	↑D
0	2.7234	4.5234	6.7234	2.8214	5.9431	10.1961
1	-	7.9875	10.1875	6.3151	8.2000	11.6568
2	-	-	13.6516	10.1882	11.4525	14.1351
3	-	-	17.1157	14.1322	15.0692	17.1965
4	-	-	-	18.1008	18.8414	-
	Head-wave (downgoing)			Body-wave (downgoing)		
order	$c_0 T_{\mathrm{HW}-}^{[n]}/d$			$c_0 T_{\mathrm{BW}-}^{[n]}/d$		
$[n]$	↑B	↑C	↑D	↑B	↑C	↑D
0	2.7407	4.5407	6.7407	2.8355	5.9498	10.2000
1	-	8.0048	10.2048	6.3340	8.2146	11.6671
2	-	-	13.6689	10.2078	11.4700	14.1492
3	-	-	17.1330	14.1520	15.0877	17.2128
4	-	-	-	18.1207	18.8605	-

Table 5.3: Arrival times of constituents in the vacuum.

Arrival times			
	Body-wave		
order	$c_0 T_{\mathrm{BW}}^{[n]}/d$		
$[n]$	↓B	↓C	↓D
0	2.7321	4.5321	6.7321
1	6.3284	7.9962	10.1962
2	10.2026	11.4624	13.6603
3	14.1469	15.0818	17.1244
4	18.1156	18.8550	-
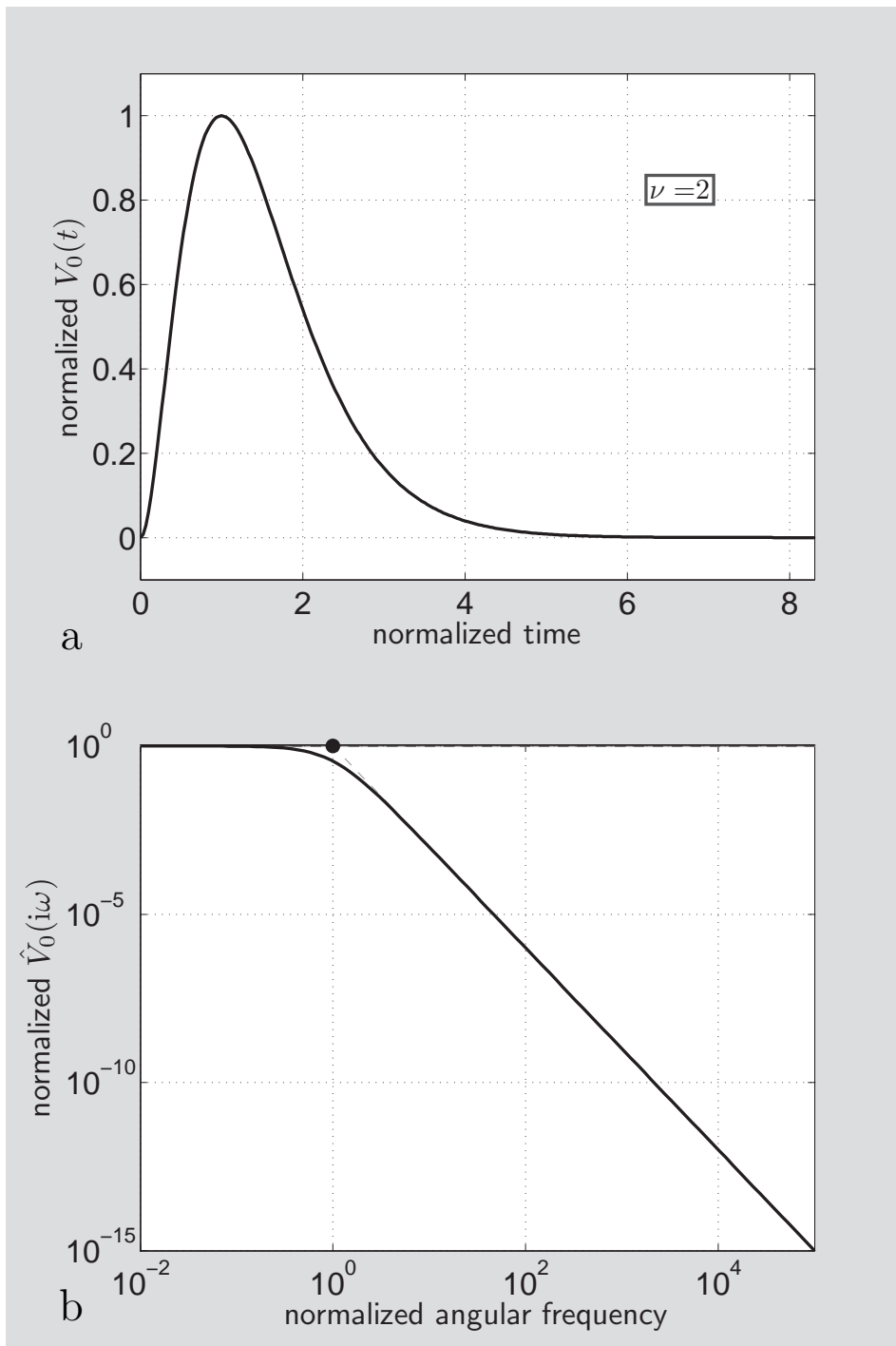
Figure 5.2: The power exponential excitation signature. (a) Pulse shape; (b) Spectral diagram.
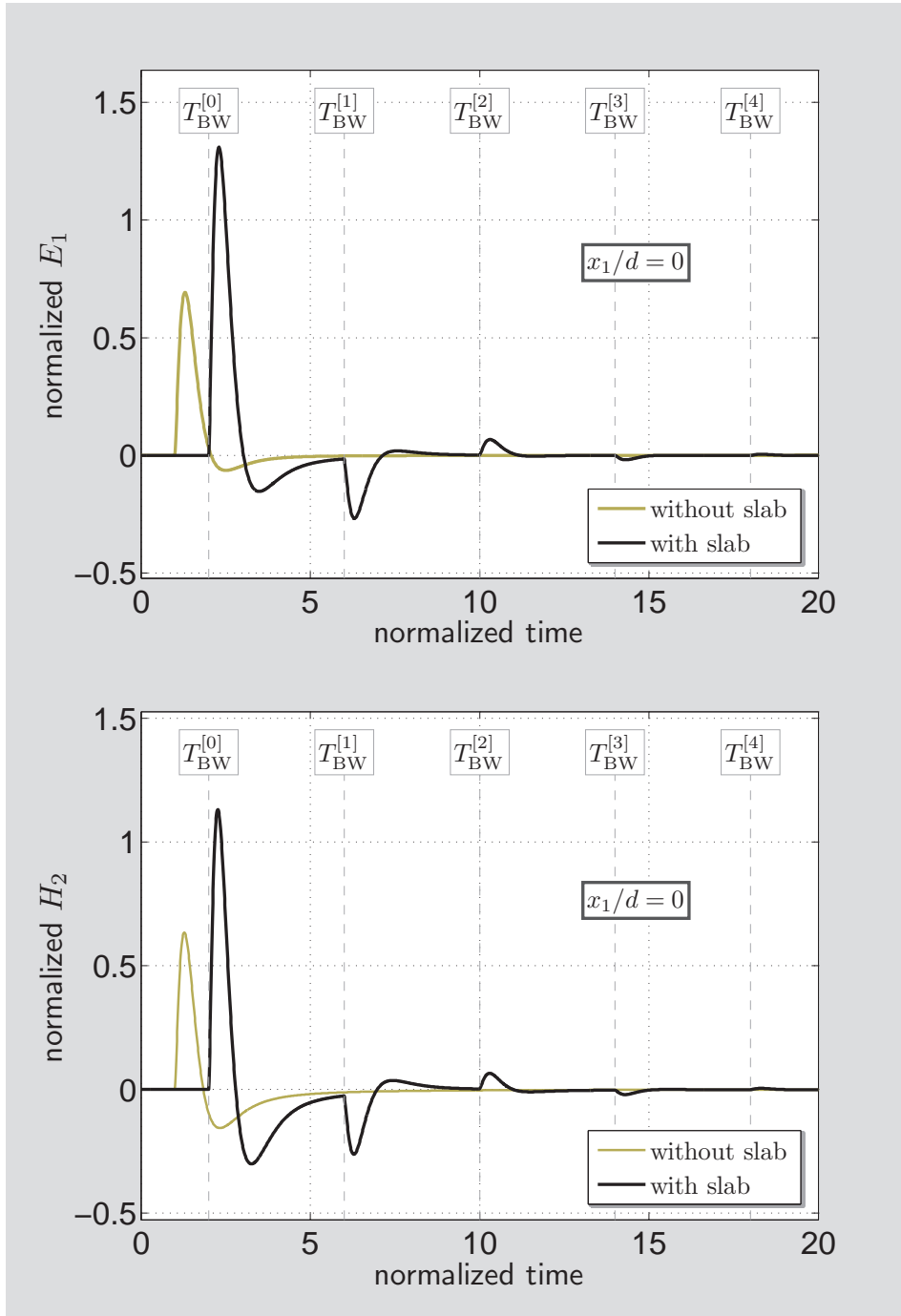
Figure 5.3: Normalized E_1 field time-domain response and normalized H_2 field time-domain response at $x_1/d = 0$.
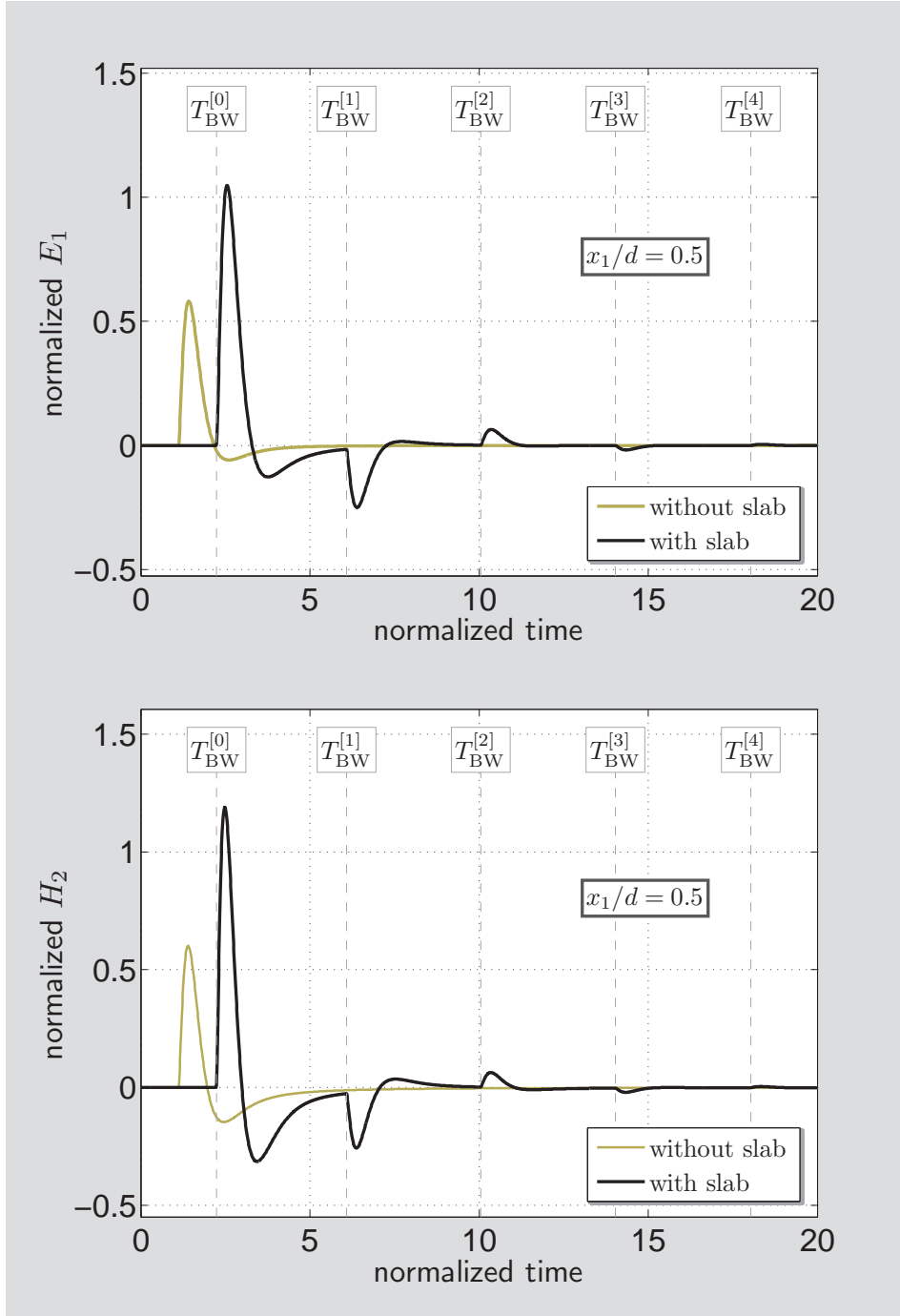
Figure 5.4: Normalized E_1 field time-domain response and normalized H_2 field time-domain response at $x_1/d = 0.5$.
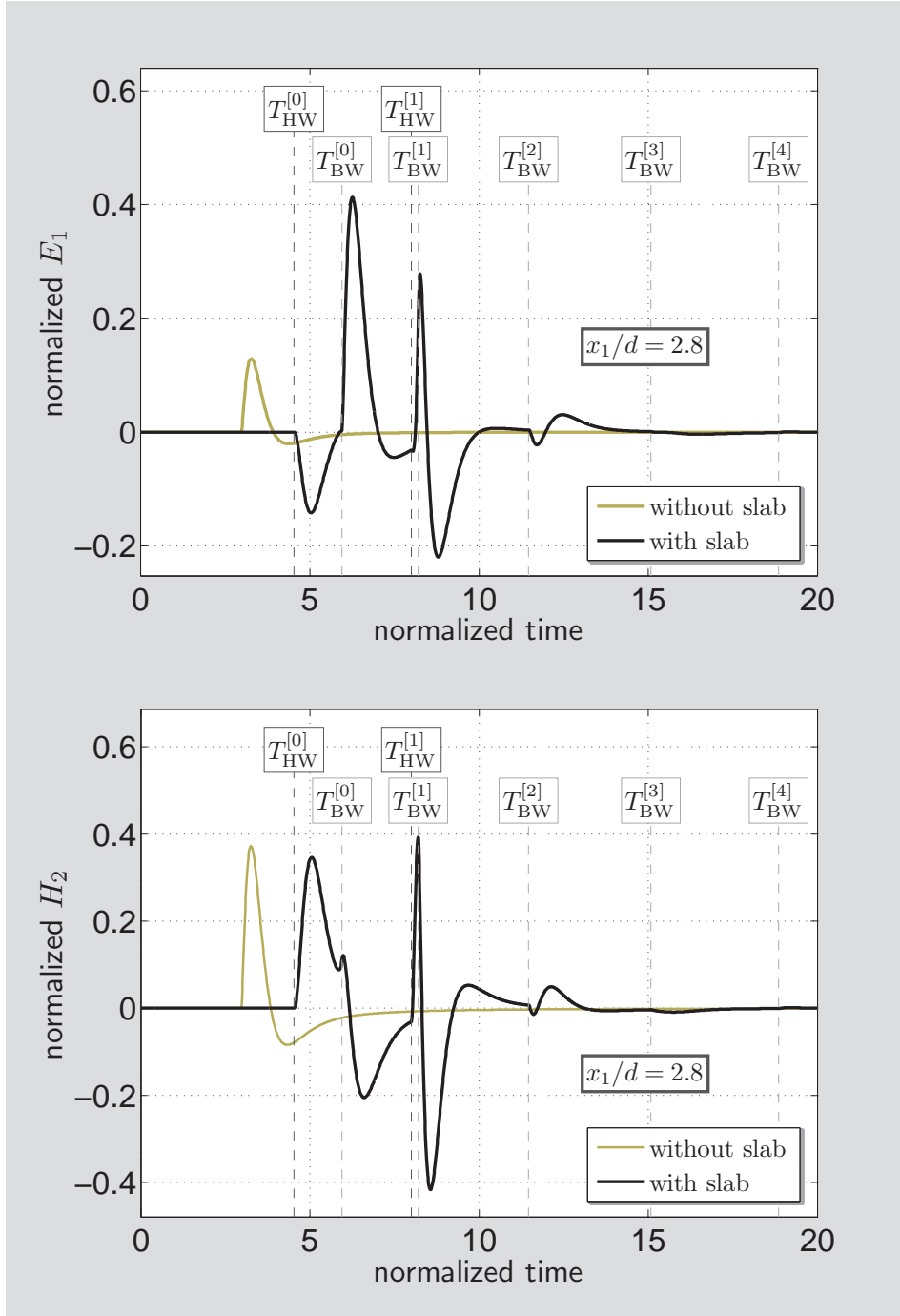
Figure 5.5: Normalized E_1 field time-domain response and normalized H_2 field time-domain response at $x_1/d = 2.8$.
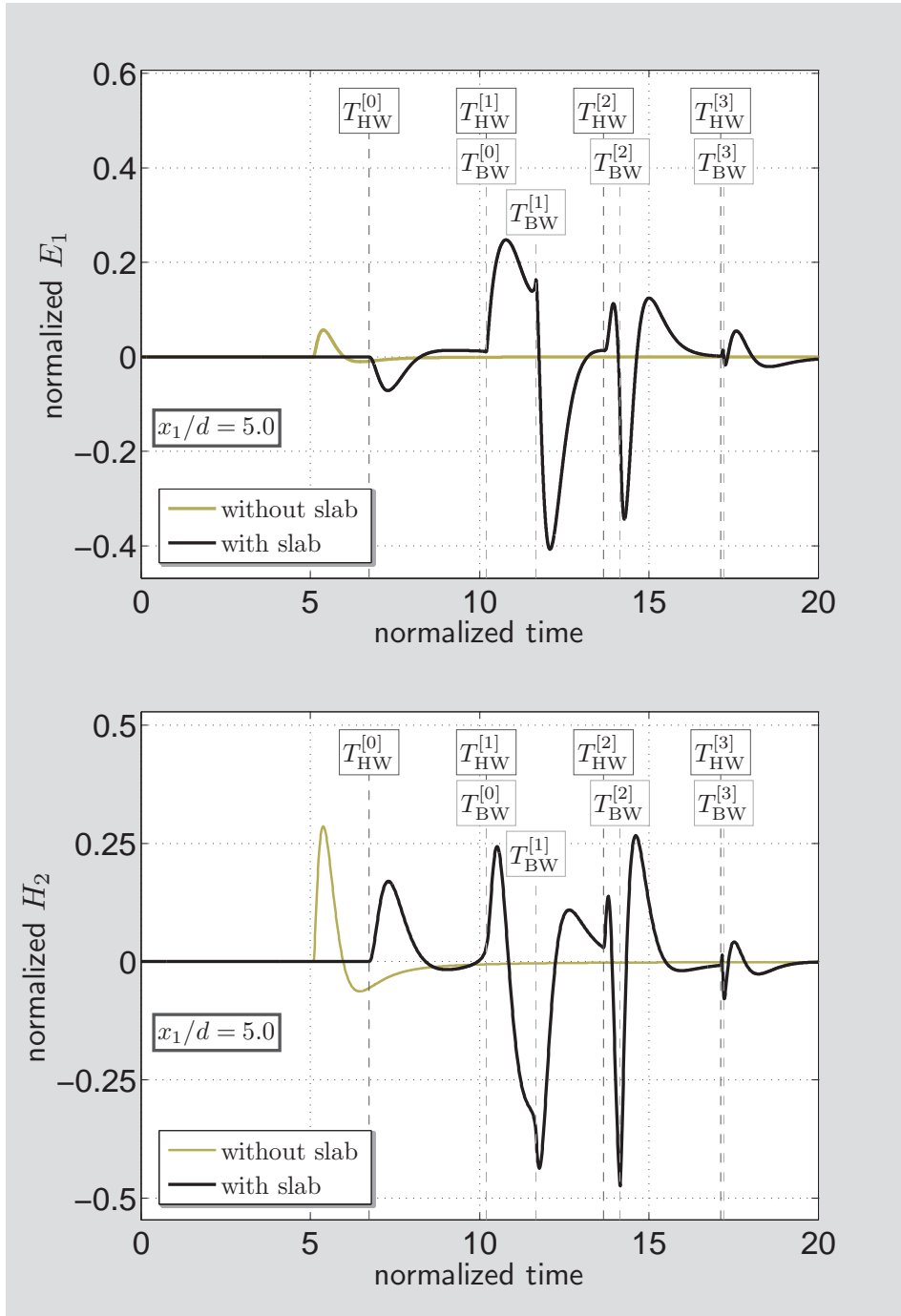
Figure 5.6: Normalized E_1 field time-domain response and normalized H_2 field time-domain response at $x_1/d = 5.0$.
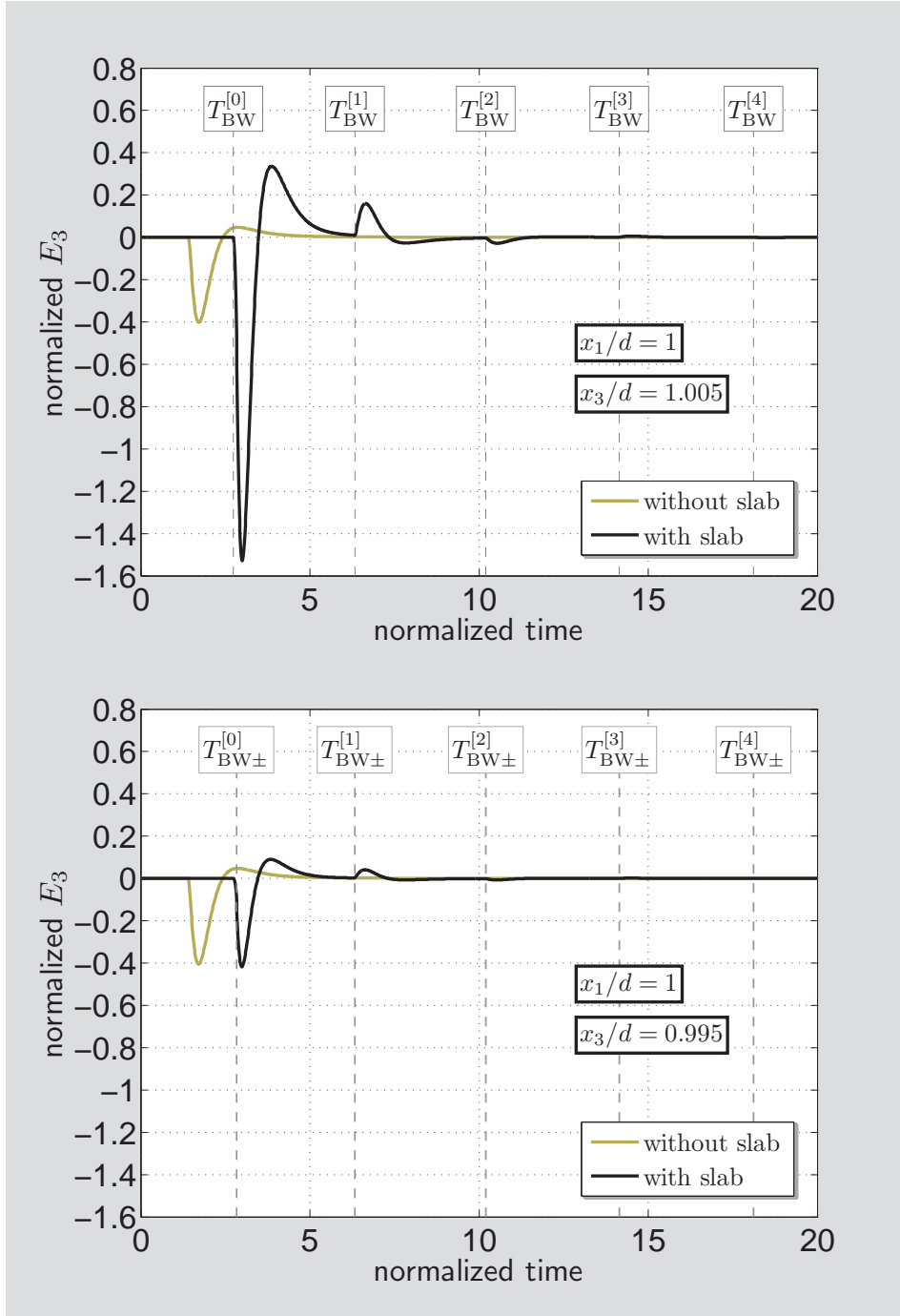
Figure 5.7: Normalized E_3 field time-domain response above ($x_3/d = 1.005$) and below ($x_3/d = 0.995$) the dielectric interface at $x_1/d = 1.0$.
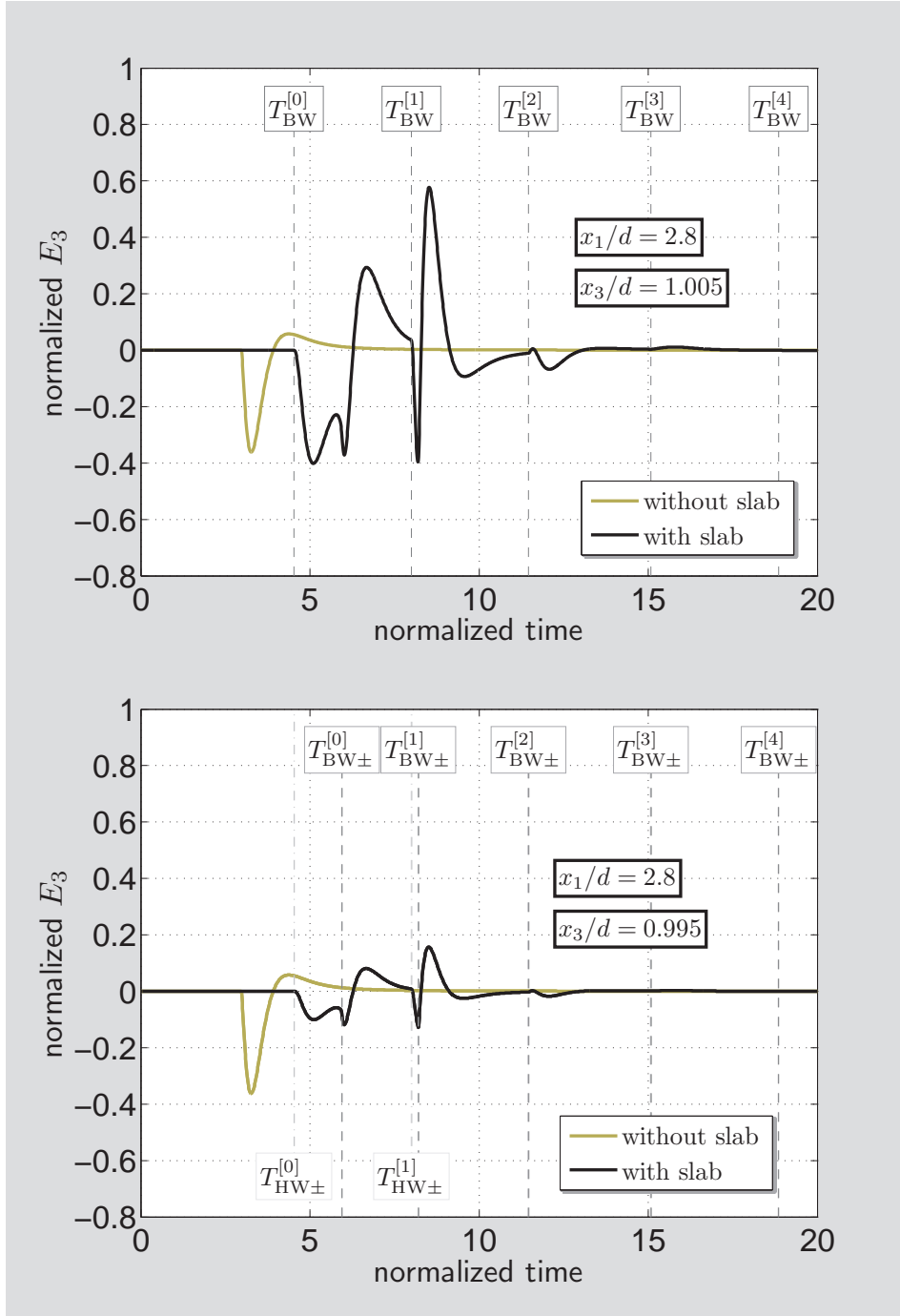
Figure 5.8: Normalized E_3 field time-domain response above ($x_3/d = 1.005$) and below ($x_3/d = 0.995$) the dielectric interface at $x_1/d = 2.8$.
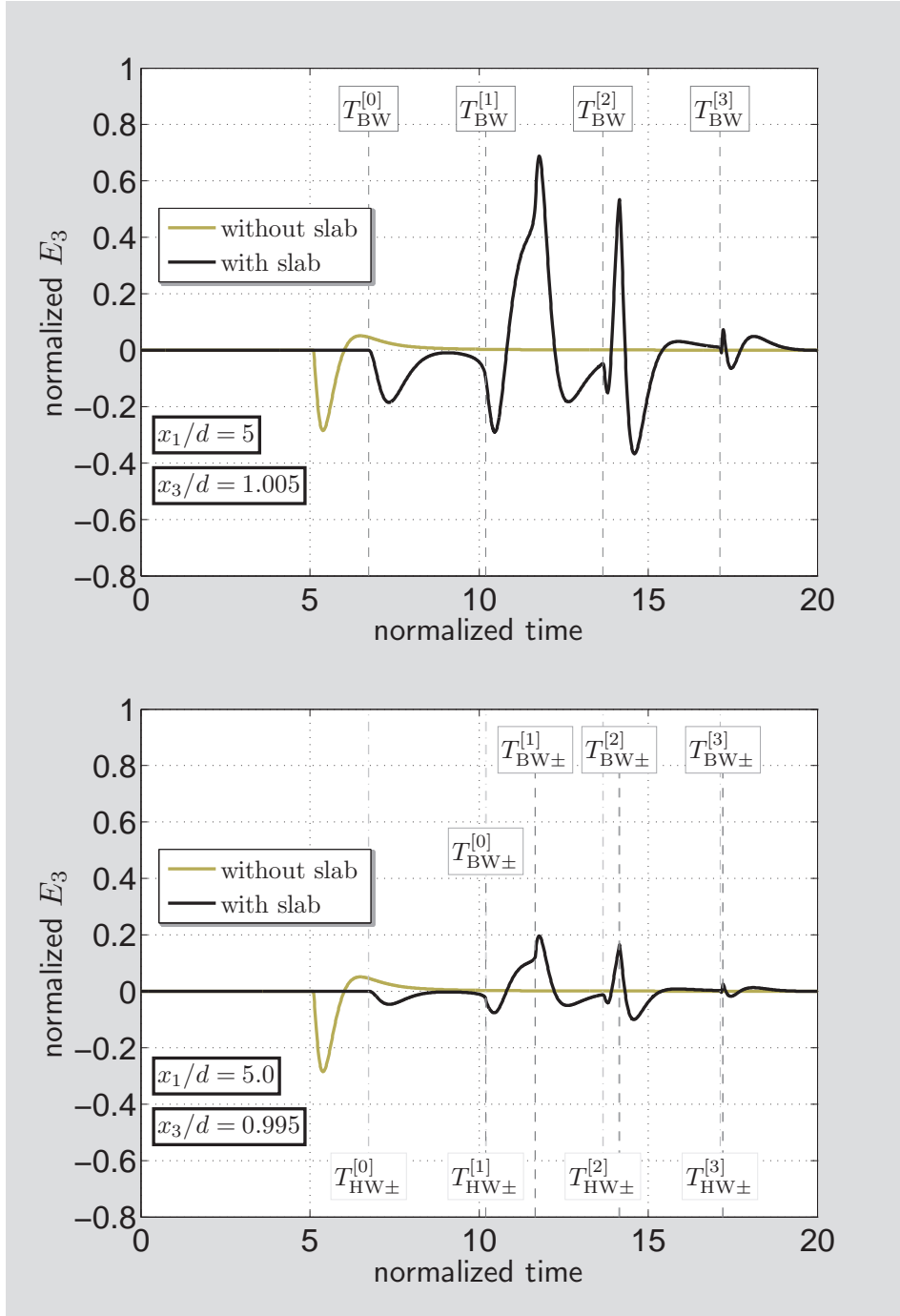
Figure 5.9: Normalized E_3 field time-domain response above ($x_3/d = 1.005$) and below ($x_3/d = 0.995$) the dielectric interface at $x_1/d = 5.0$.
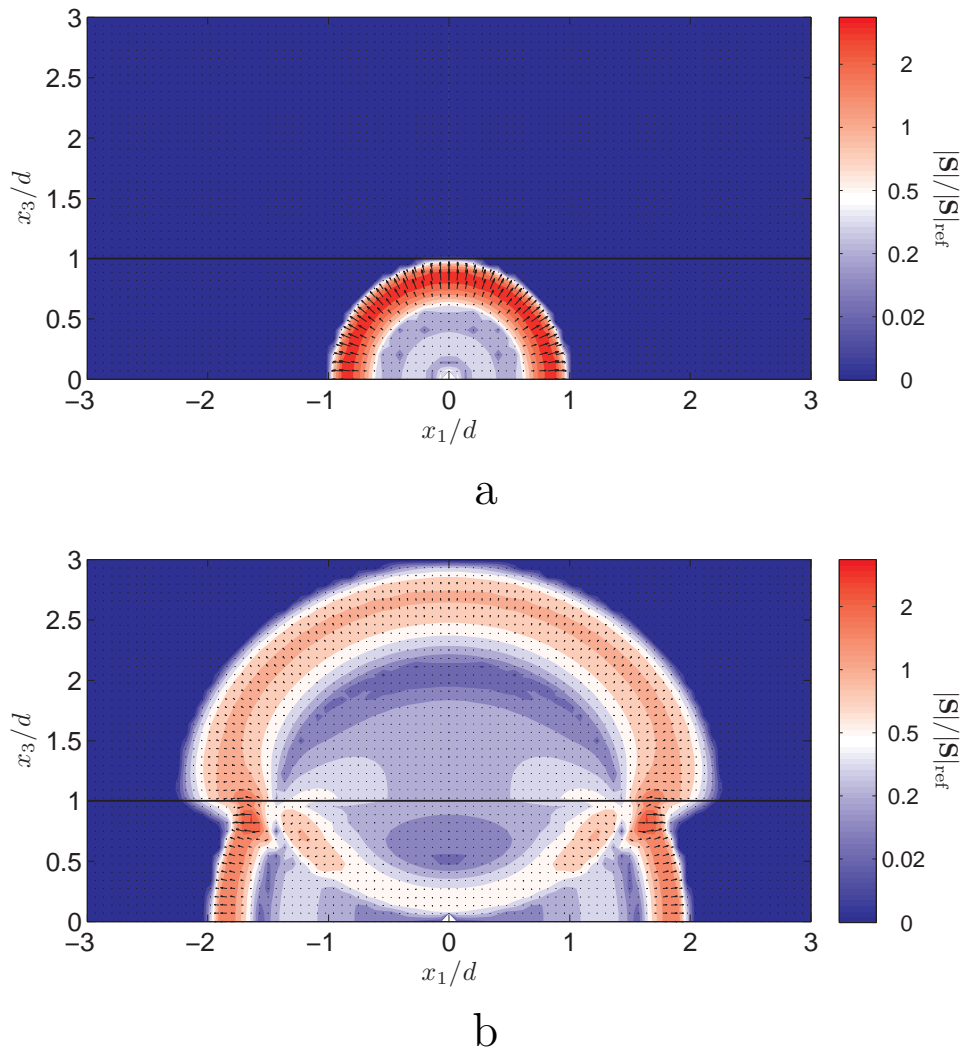
Figure 5.10: Normalized Poynting vector of the field at (a) $c_0t/d = 2$; (b) $c_0t/d = 4$. Electromagnetic parameters of the dielectric slab are $\{\epsilon_1, \mu_1\} = \{4\epsilon_0, \mu_0\}$. Parameters of the excitation pulse are $c_0t_w/d = 0.9236$, $\nu = 2$.
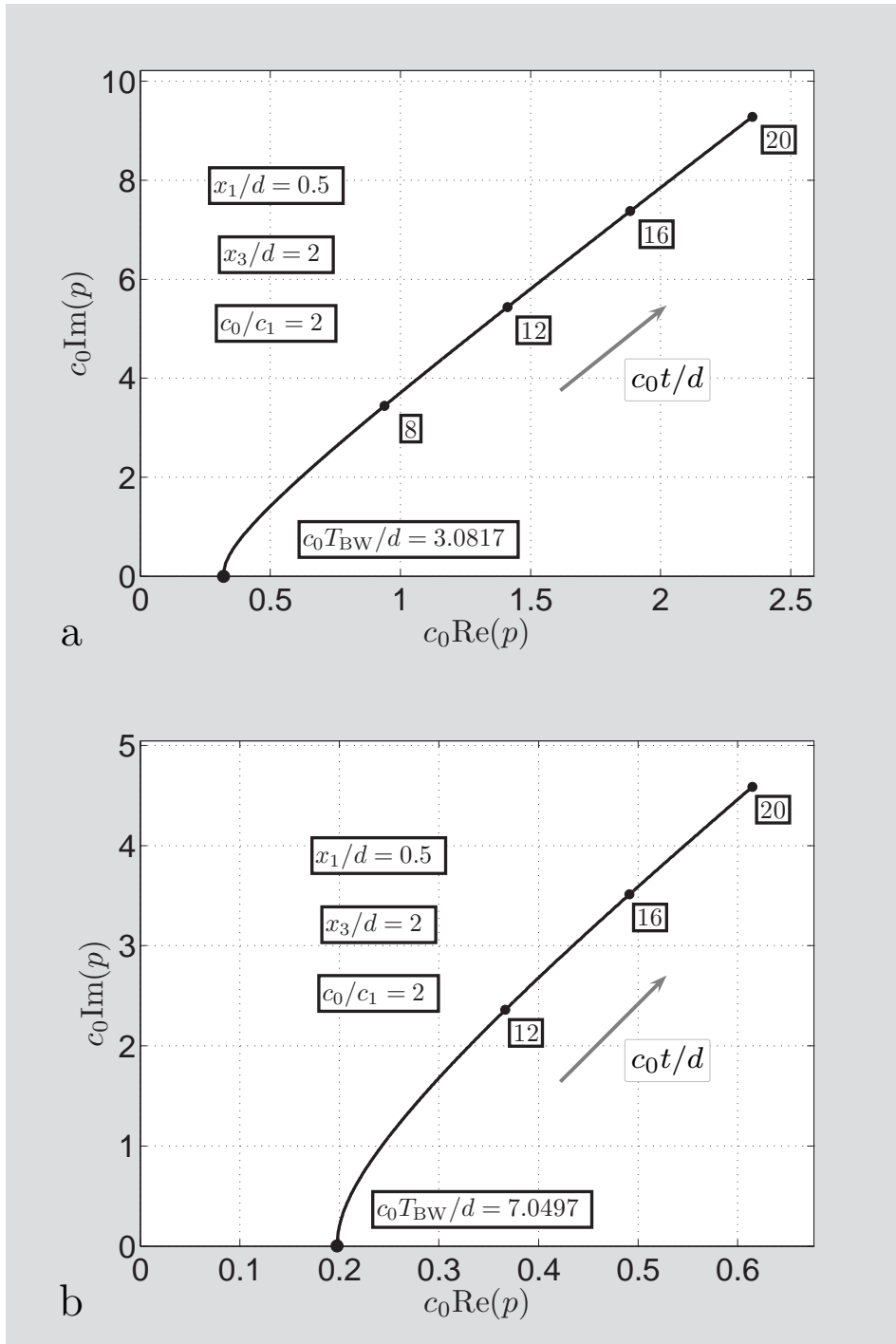
Figure 5.11: Examples of Cagniard-DeHoop contours associated with the first two successive time-domain constituents in vacuum (a) $n = 0$; (b) $n = 1$.
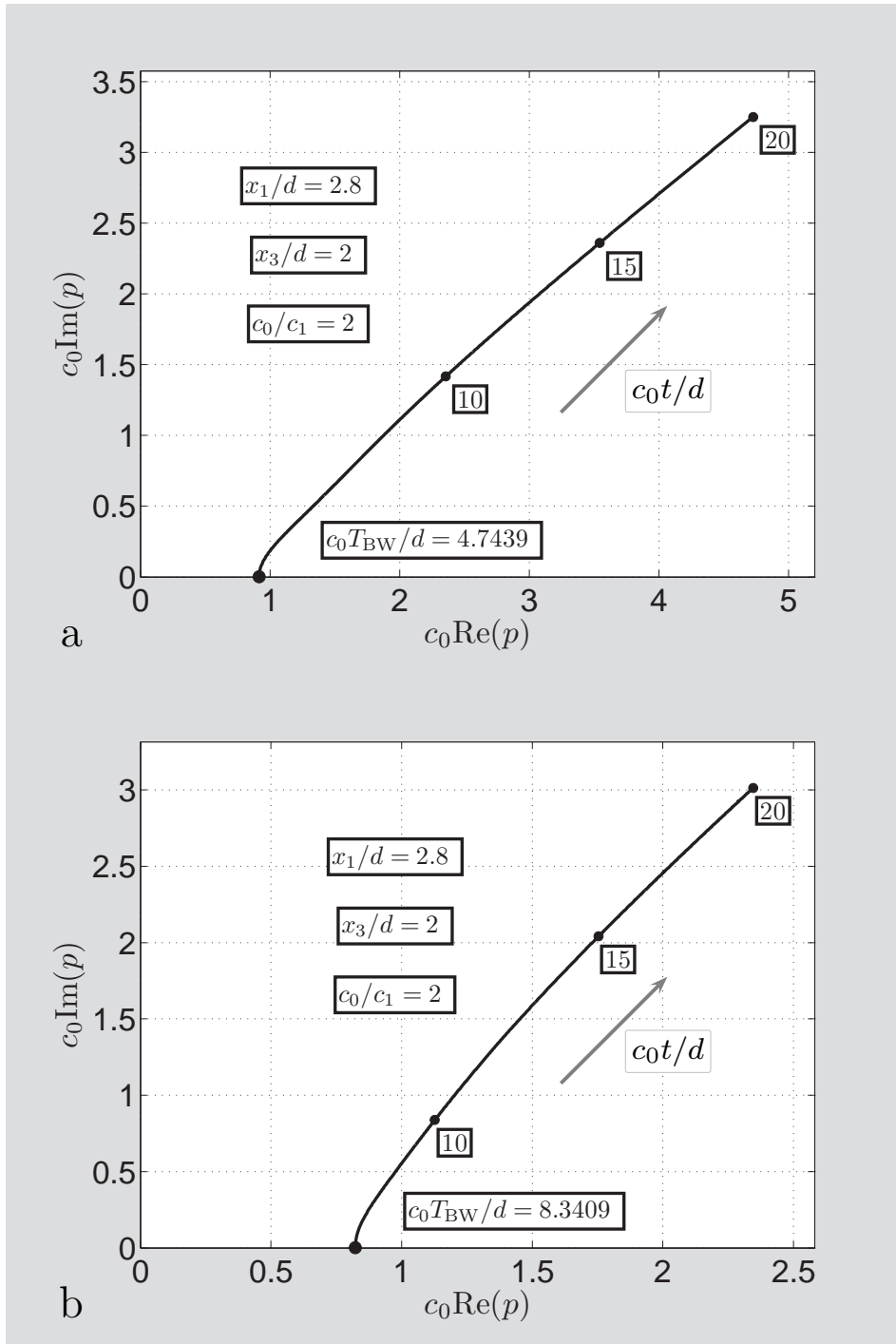
Figure 5.12: Examples of Cagniard-DeHoop contours associated with the first two successive time-domain constituents in vacuum (a) $n = 0$; (b) $n = 1$.

39

Chapter 6

Pulsed electromagnetic field radiation from a wide slot antenna

Summary

The pulsed electromagnetic field radiated by a 2D slot antenna with a finite slot width is analytically investigated via the application of the Cagniard-DeHoop technique. Starting with the description and formulation of the field problem we shall arrive at closed-form expressions describing the pulsed field radiation behavior of a finite slot in an electrically perfectly conducting screen. The closed-form time-domain expressions are consequently used for the studying of time-domain beam-steering and beam-shaping capabilities of a simple antenna array. Illustrative numerical results are also given in Chapter 8, where a pulse distortion due to the presence of a dielectric slab is investigated.[3]

6.1 Introduction

The present chapter aims at providing the description of pulsed electromagnetic field radiation from a slot of a finite width in an unbounded electrically perfectly conducting screen. The source excited the structure is modeled as a prescribed distribution of the transverse electric field across the slot of a uniform and finite width. The structure further radiates into free space. Using the combination of a unilateral Laplace transformation with respect to time and the spatial slowness representation of the field components that is known as the Cagniard-DeHoop method [11, 12], closed-form expressions are obtained for the electric and the magnetic field as a function of position and time.

It is shown that the excitation via a wide slot shows additional features in that the corners of the waveguide feed show a separate diffractive behavior with accompanying wavefronts. In this case, the wave motion radiated from such slot consists of two cylindrical waves emanating from the edges of the slot and of a plane wave coming upward from the slot. Again, as in Sec. 3.4, the radiated electromagnetic field components are also expressed via the appropriate fundamental soultion that is found in two equivalent forms.

The results of this section are used in the investigation of pulsed-field radiation behavior of the array of slot antennas of a finite width [41]. This can be useful in the development of direct time-domain pulsed-field radar return identification methods [8, 33]. First results of these methods typically deal with responses from certain classes of objects to an incident, linearly polarized, plane wave with a ramp function electric field pulse shape, observed in the far-field region of the scatterer, under the application of some physical-optics field approximation on the boundary surface of the object. One of the first generalizations of the method involves the taking into account of the properties of the transmitting antenna and allowing the scattering object not necessarily to be in the far-field region of the antenna (where a local plane-wave approximation applies). The interaction of the pulsed transmitted field with the scatterer can then be analyzed through the time-domain field/source reciprocity theorem [17]. For this, the time-domain expression of the field transmitted by the radar antenna is needed. With this kind of application in mind, the pulsed EM field radiated by a planar array of slot antennas in a 2D setting are given. Neglecting the mutual coupling between the slots, the Cagniard-DeHoop technique provides closed-form analytic expressions for all field components, expressed in terms of the transverse electric field distibution in the apertures. By exciting the slots with pulse shapes of various amplitudes, pulse rise times, pulse time widths and mutual time delays, beam steering and beam shaping can be influenced. Combined with the mutual geometrical positioning of the slots, there is a substantial amount of parameters whose influence on the antenna's time-domain performance can be studied with the expressions obtained.

The illustrative numerical examples of antenna beam-steering and beam-shaping are presented in the last section of this chapter. The illustrative numerical examples concerning a pulsed electromagnetic field radiation behavior of a single slot are provided in Chapter 8, where the pulse distortion due to the presence of a dielectric slab is investigated.

6.2 Description of the configuration and formulation of the field problem

The configuration examined is shown in Fig. 6.1. The configuration consists of an unbounded electrically perfectly conducting screen $\mathcal{S} = \{(-\infty < x_1 < -w/2) \cup (w/2 < x_1 < \infty), -\infty < x_2 < \infty, x_3 = 0\}$ with a feeding aperture $\mathcal{A} = \{-w/2 < x_1 < w/2, -\infty < x_2 < \infty, x_3 = 0\}$ of the finite width $w > 0$. The structure radiates into the vacuum half-space $\mathcal{D}_0 = \{-\infty < x_1 < \infty, -\infty < x_2 < \infty, 0 < x_3 < \infty\}$ with vacuum electric permittivity and magnetic permeability $\{\epsilon_0, \mu_0\}$ and corresponding electromagnetic wave speed $c_0 = (\epsilon_0 \mu_0)^{-1/2}$.

The antenna aperture is fed by the uniformly distributed, x_2-independent, electric field

$$E_1(x_1, 0, t) = V_0(t)/w \quad \text{in } \mathcal{A} \tag{6.1}$$

Since the excitation, as well as the configuration, are independent of x_2, the non-zero components of the electric field strength $\{E_1, E_3\}(x_1, x_3, t)$ and the magnetic field strength
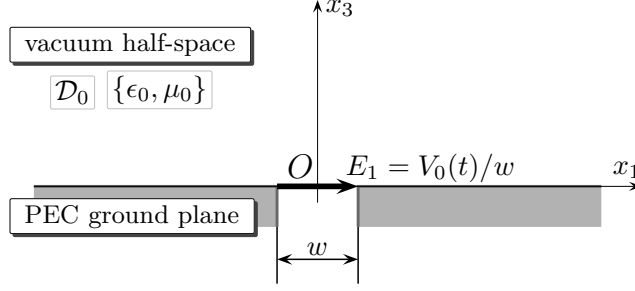
Figure 6.1: Configuration with indication of the aperture feeding.

$H_2(x_1, x_3, t)$ satisfy in $\mathcal{D}_0$ the source-free field equations (cf. Eqs. (2.5) – (2.7))

$$\partial_1 H_2 - \epsilon_0 \partial_t E_3 = 0 \tag{6.2}$$

$$\partial_3 H_2 + \epsilon_0 \partial_t E_1 = 0 \tag{6.3}$$

$$\partial_1 E_3 - \partial_3 E_1 - \mu_0 \partial_t H_2 = 0 \tag{6.4}$$

with the excitation condition (cf. Eq. (2.3))

$$\lim_{x_3 \downarrow 0} E_1(x_1, x_3, t) = [V_0(t)/w]\Pi(x_1/w) \quad \text{for all } t \tag{6.5}$$

where $\Pi(x)$ is the rectangular function (see Eq. 2.4). It is assumed that $V_0(t)$ starts to act at $t = 0$ and that prior to this instant the field vanishes throughout the configuration.

6.3   Field representations

In view of the Cagniard-DeHoop technique we employ the unilateral Laplace transformation with respect to time

$$\hat{V}_0(s) = \int_{t=0}^{\infty} \exp(-st)V_0(t)\mathrm{d}t \tag{6.6}$$

in which s is taken to be real-valued and positive relying on Lerch's theorem [27], [44]. Further we use the wave slowness field representation

$$\left\{ \hat{E}_1, \hat{E}_3, \hat{H}_2 \right\}(x_1, x_3, s) = \frac{s}{2\pi\mathrm{i}} \int_{p=-\mathrm{i}\infty}^{\mathrm{i}\infty} \exp(-spx_1) \left\{ \tilde{E}_1, \tilde{E}_3, \tilde{H}_2 \right\}(p, x_3, s)\mathrm{d}p \tag{6.7}$$

Under these transformations, the field equations (6.2) – (6.4) and the excitation condition (6.5) transform into

$$-sp\tilde{H}_2 - s\epsilon_0 \tilde{E}_3 = 0 \tag{6.8}$$

$$\partial_3 \tilde{H}_2 + s\epsilon_0 \tilde{E}_1 = 0 \tag{6.9}$$

$$-sp\tilde{E}_3 - \partial_3 \tilde{E}_1 - s\mu_0 \tilde{H}_2 = 0 \tag{6.10}$$

and

$$\lim_{x_3 \downarrow 0} \tilde{E}_1(p, x_3, s) = \frac{\hat{V}_0(s)}{w} \frac{\exp(spw/2) - \exp(-spw/2)}{sp} \tag{6.11}$$

respectively. The bounded slowness-domain field quantities follow from (6.8) – (6.10) by expressing them in the form

$$\left\{\tilde{E}_1, \tilde{E}_3, \tilde{H}_2\right\}(p, x_3, s) = \{\gamma_0(p)/\epsilon_0, -p/\epsilon_0, 1\} A(p, s) \exp\left[-s\gamma_0(p)x_3\right] \quad \text{in } \mathcal{D}_0 \tag{6.12}$$

The unknown $A(p, s)$ results from the application of the excitation condition (6.11) as

$$A(p, s) = \frac{\hat{V}_0(s)}{w} \frac{\epsilon_0}{\gamma_0(p)} \frac{\exp(spw/2) - \exp(-spw/2)}{sp} \tag{6.13}$$

6.4 The time-domain radiated fields

In this section we focus on the time-domain fields radiated into the vacuum halfspace $\mathcal{D}_0$. Using the results of Section 6.3 we express them as

$$\{\hat{E}_1, \hat{E}_3, \hat{H}_2\}(x_1, x_3, s) = \frac{\hat{V}_0(s)}{2\pi w \mathrm{i}} \int_{p=-\mathrm{i}\infty}^{\mathrm{i}\infty} \left\{\frac{1}{p}, -\frac{1}{\gamma_0(p)}, \frac{\epsilon_0}{p\gamma_0(p)}\right\}$$
$$\times \left\{\exp\{-s[p(x_1 - w/2) + \gamma_0(p)x_3]\} - \exp\{-s[p(x_1 + w/2) + \gamma_0(p)x_3]\}\right\} \mathrm{d}p \tag{6.14}$$

The algebraic parts of the integrands do not contain any propagation coefficient that differs from the propagation coefficient $\gamma_0(p)$ in the propagation factors. This has the consequence that the corresponding Cagniard-DeHoop contours for a positive horizontal offset intersect the real p-axis in between $p = 0$ and $p = 1/c_0$, implying the absence of head-waves. Following the recipe given in Appendix B for $c_0 = c_1$, the corresponding time-domain expressions can be found as

$$\{E_1, E_3, H_2\}(x_1, x_3, t) = \frac{V_0(t)}{w} \overset{(t)}{*} \frac{1}{\pi}\left[\left\{\frac{x_3(x_1 - w/2)}{c_0^2 t^2 - x_3^2}, -1, \frac{1}{\mu_0}\frac{(x_1 - w/2)t}{c_0^2 t^2 - x_3^2}\right\}\frac{H(t - T_{\mathrm{b}})}{(t^2 - T_{\mathrm{b}}^2)^{1/2}}\right.$$
$$\left. - \left\{\frac{x_3(x_1 + w/2)}{c_0^2 t^2 - x_3^2}, -1, \frac{1}{\mu_0}\frac{(x_1 + w/2)t}{c_0^2 t^2 - x_3^2}\right\}\frac{H(t - T_{\mathrm{a}})}{(t^2 - T_{\mathrm{a}}^2)^{1/2}}\right]$$
$$+ [V_0(t - x_3/c_0)/w]\left\{1, 0, (\epsilon_0/\mu_0)^{1/2}\right\} \Pi(x_1/w) \tag{6.15}$$

with

$$T_{\mathrm{b}} = [(x_1 - w/2)^2 + x_3^2]^{1/2}/c_0 \tag{6.16}$$
$$T_{\mathrm{a}} = [(x_1 + w/2)^2 + x_3^2]^{1/2}/c_0 \tag{6.17}$$

The first two terms can be interpreted as cylindrical waves emanating from the edges of the slot, while the last term represents the plane wave progressing upward from the slot.

Still, electromagnetic field components (6.15) can be expressed via the scalar Green's function as

$$\{E_1, E_3, H_2\}(x_1, x_3, t) = V_0(t) \overset{(t)}{*} \{-\partial_3 G, \partial_1 G, \epsilon_0 \partial_t G\}(x_1, x_3, t) \tag{6.18}$$

where $G(x_1, x_3, t)$ is a solution of

$$(\partial_1^2 + \partial_3^2 - \partial_t^2/c_0^2)G = 0 \tag{6.19}$$

$$\lim_{x_3 \downarrow 0} \partial_3 G = -\delta(t)\Pi(x_1/w)/w \tag{6.20}$$

From (6.15) and (6.18) it is straightforward to show that solution of (6.19)–(6.20) can be written as

$$\begin{aligned}
G(x_1, x_3, t) = &\frac{1}{\pi w} \int_{\tau=T_{\mathrm{b}}}^{t} \frac{x_1 - w/2}{\tau^2 - x_3^2/c_0^2} \frac{\tau \mathrm{d}\tau}{(\tau^2 - T_{\mathrm{b}}^2)^{1/2}} \\
&- \frac{1}{\pi w} \int_{\tau=T_{\mathrm{a}}}^{t} \frac{x_1 + w/2}{\tau^2 - x_3^2/c_0^2} \frac{\tau \mathrm{d}\tau}{(\tau^2 - T_{\mathrm{a}}^2)^{1/2}} \\
&+ c_0 H(t - x_3/c_0)\Pi(x_1/w)/w
\end{aligned} \tag{6.21}$$

An alternative approach includes the spatial convolution of the two-dimensional fundamental solution (3.20) with the spatial source distribution $\Pi(x_1/w)/w$ given as

$$G(x_1, x_3, t) = \frac{1}{\pi w} \int_{x=x_1-w/2}^{x_1+w/2} \frac{H(t - r/c_0)}{(t^2 - r^2/c_0^2)^{1/2}} \mathrm{d}x \tag{6.22}$$

where $r = (x^2 + x_3^2)^{1/2} > 0$. Applying the integration by parts and noting that $\delta[f(x)] = [\delta(x - x_0) + \delta(x + x_0)]/|f'(x_0)|$, $f(\pm x_0) = 0$, we arrive at

$$\begin{aligned}
G(x_1, x_3, t) = \frac{c_0}{\pi w} \Bigg\{ &\arcsin\left[\frac{x_1 + w/2}{(c_0^2 t^2 - x_3^2)^{1/2}}\right] H(t - T_{\mathrm{a}}) \\
&- \arcsin\left[\frac{x_1 - w/2}{(c_0^2 t^2 - x_3^2)^{1/2}}\right] H(t - T_{\mathrm{b}}) \Bigg\} \\
&+ c_0 H(t - x_3/c_0)\Pi(x_1/w)/w
\end{aligned} \tag{6.23}$$

The Eq. (6.23) can be connected with Eq. (6.21) through the following relation

$$-c_0\partial_t \arcsin\left[\frac{x_1 \pm w/2}{(c_0^2 t^2 - x_3^2)^{1/2}}\right] = \frac{(x_1 \pm w/2)t}{t^2 - x_3^2/c_0^2} \frac{1}{(t^2 - T_{\mathrm{a,b}}^2)^{1/2}} \tag{6.24}$$

that validates our results.

6.5 Illustrative numerical examples

This section contains some illustrative numerical results concerning the antenna array configuration (Fig. 6.2) consisting of radiating slots that are excited by mutually delayed power exponential pulses.
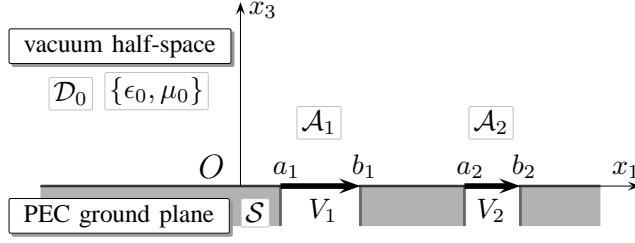
Figure 6.2: Antenna array configuration.

The antenna array consists of an electrically perfectly conducting screen $\mathcal{S}$ with the collection of N non-overlapping feeding slots $\cup_{n=1}^{N}\mathcal{A}_n$, with $\mathcal{A}_n = \{a_n < x_1 < b_n, -\infty < x_2 < \infty, x_3 = 0\}$, subject to the condition $a_1 < b_1 < \ldots < a_N < b_N$. The antenna radiates into the vacuum half-space $\mathcal{D}_0 = \{-\infty < x_1 < \infty, -\infty < x_2 < \infty, x_3 > 0\}$. We neglect mutual coupling. Under this condition, the radiated field is the superposition of the fields radiated by the different slots

$$\{E_1, E_3, H_2\}(x_1, x_3, t) = \sum_{n=1}^{N} \frac{V_n(t)}{b_n - a_n} \overset{(t)}{*} \left[\frac{1}{\pi} \left\{ \frac{x_3(x_1 - b_n)}{c_0^2 t^2 - x_3^2}, 1, \frac{1}{\mu_0} \frac{(x_1 - b_n)t}{c_0^2 t^2 - x_3^2} \right\} \frac{H(t - T_{b;n})}{(t^2 - T_{b;n}^2)^{1/2}} \right.$$
$$- \frac{1}{\pi} \left\{ \frac{x_3(x_1 - a_n)}{c_0^2 t^2 - x_3^2}, 1, \frac{1}{\mu_0} \frac{(x_1 - a_n)t}{c_0^2 t^2 - x_3^2} \right\} \frac{H(t - T_{a;n})}{(t^2 - T_{a;n}^2)^{1/2}}$$
$$\left. + \left\{ 1, 0, (\epsilon_0/\mu_0)^{1/2} \right\} [H(x_1 - a_n) - H(x_1 - b_n)]\delta(t - x_3/c_0) \right]$$

$$(6.25)$$

in which

$$T_{a;n} = [(x_1 - a_n)^2 + x_3^2]^{1/2}/c_0 \qquad (6.26)$$
$$T_{b;n} = [(x_1 - b_n)^2 + x_3^2]^{1/2}/c_0 \qquad (6.27)$$

All cylindrical wave field constituents contain time-convolution integrals with inverse square-root singularities at the arrival time of the wave. These are numerically handled via a stretching of the variable of integration according to

$$\tau = T_{a;n} \cosh(u) \quad \text{for } 0 < u < \infty \qquad (6.28)$$

with the Jacobian

$$\frac{\partial \tau}{\partial u} = T_{a;n} \sinh(u) = (\tau^2 - T_{a;n}^2)^{1/2} \qquad (6.29)$$

For an array with $N = 5$, $b_n - a_n = w$ ($n = 1, \ldots, 5$) and $a_{n+1} = b_n + w/2$ ($n = 1, \ldots, 4$), the (color) vector density plots Figs. 6.4 – 6.11 show the time evolution of the two-component Poynting vector

$$S_1 = -E_3 H_2 \qquad (6.30)$$
$$S_3 = E_1 H_2 \qquad (6.31)$$

45
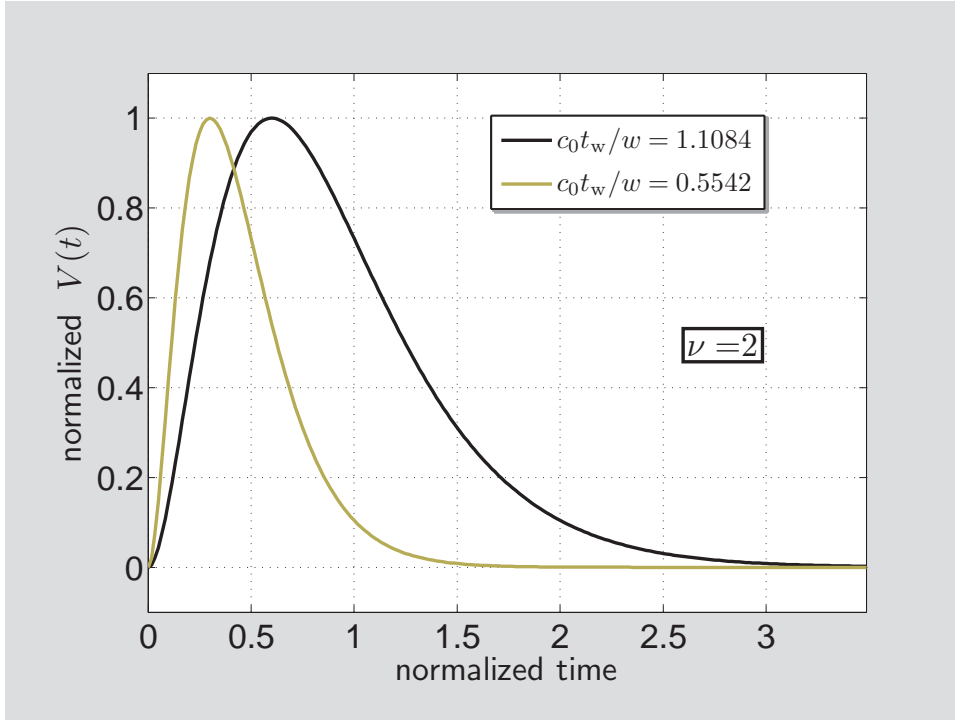
Figure 6.3: Excitation pulse shapes.

normalized to the magnitude $|\boldsymbol{S}|_{\text{ref}}$ of the maximum value of the Poynting vector as it would be carried by a TEM-mode in a parallel-plate waveguide that would be feeding the radiating apertures, i.e.

$$|\boldsymbol{S}|_{\text{ref}} = (\epsilon_0/\mu_0)^{1/2} \max_n [V_{\text{max};n}/(b_n - a_n)]^2 \quad \text{for } n = 1, \ldots, N \tag{6.32}$$

Two sets of excitation pulses are taken to have all the same amplitudes and different shapes with $c_0 t_r = \{0.3, 0.6\}w$, which gives the spatial supports of pulses (a) $c_0 t_w = 0.5542w$ and (b) $c_0 t_w = 1.1084w$ for $\nu = 2$. These activating pulses are shown in Fig. 6.3, where the normalized time is $c_0 t/w$ and normalized $V(t)$ is $V(t)/V_{\text{max}}$.

Four different time delays between the pulse starting values have been considered: (A) $c_0(T_{n+1} - T_n)/w = 0$, (B) $c_0(T_{n+1} - T_n)/w = 0.5$, (C) $c_0(T_{n+1} - T_n)/w = 1.0$, (D) $c_0(T_{n+1} - T_n)/w = 1.5$, all for $n = 1 \ldots, 4$ and $T_1 = 0$, and two observation times $c_0 t/w = \{4, 8\}$.

The plots clearly show the beam-steering associated with the time delays in excitation and the beam-shaping associated with the spatial supports of activating pulses. In Figures 6.4a–6.11a that correspond to the narrower excitation pulse shape, the particular cylidrical wave components are more distinguishable in comparison with Figs. 6.4b–6.11b connected with the excitation pulses whose spatial support sligthly exceeds beyond the slot width. In the latter, the particular components of the pertaining wave motion are mutually blurred. If the spatial support of activating pulses is further increased then the (time-varying) spatial distribution of the Poynting vector becomes more 'homogenous' and for zero excitation delays, the wave motion resembles one that would be radiated from a single wide slot.
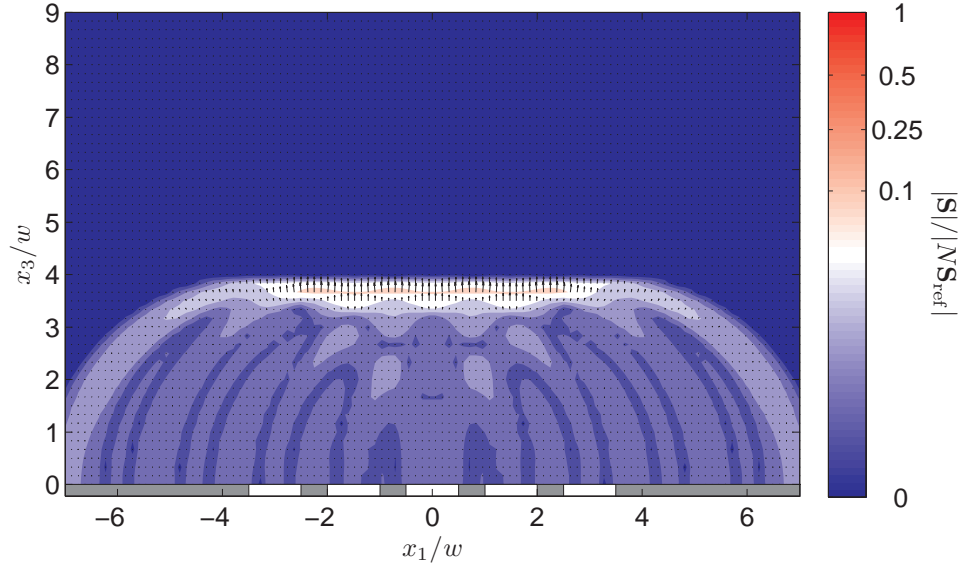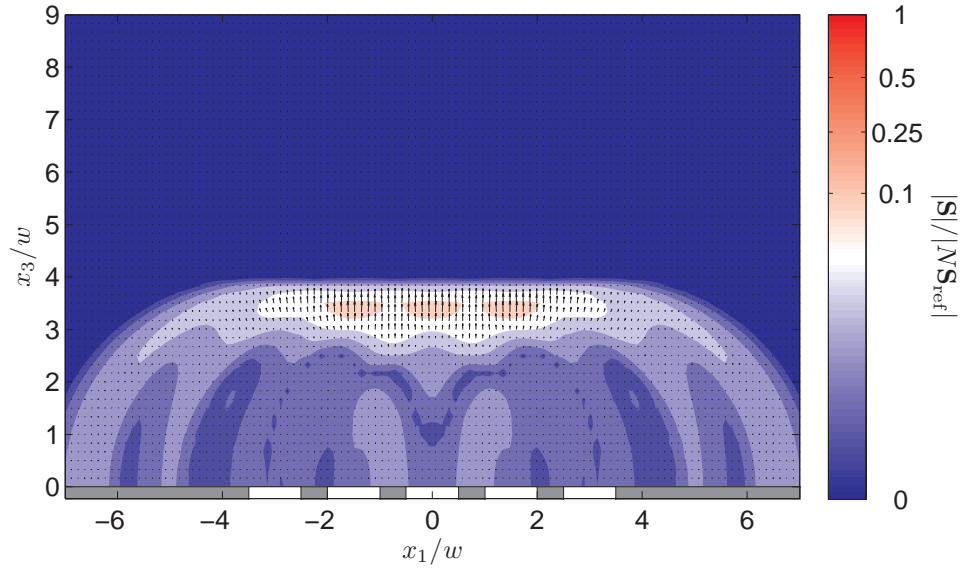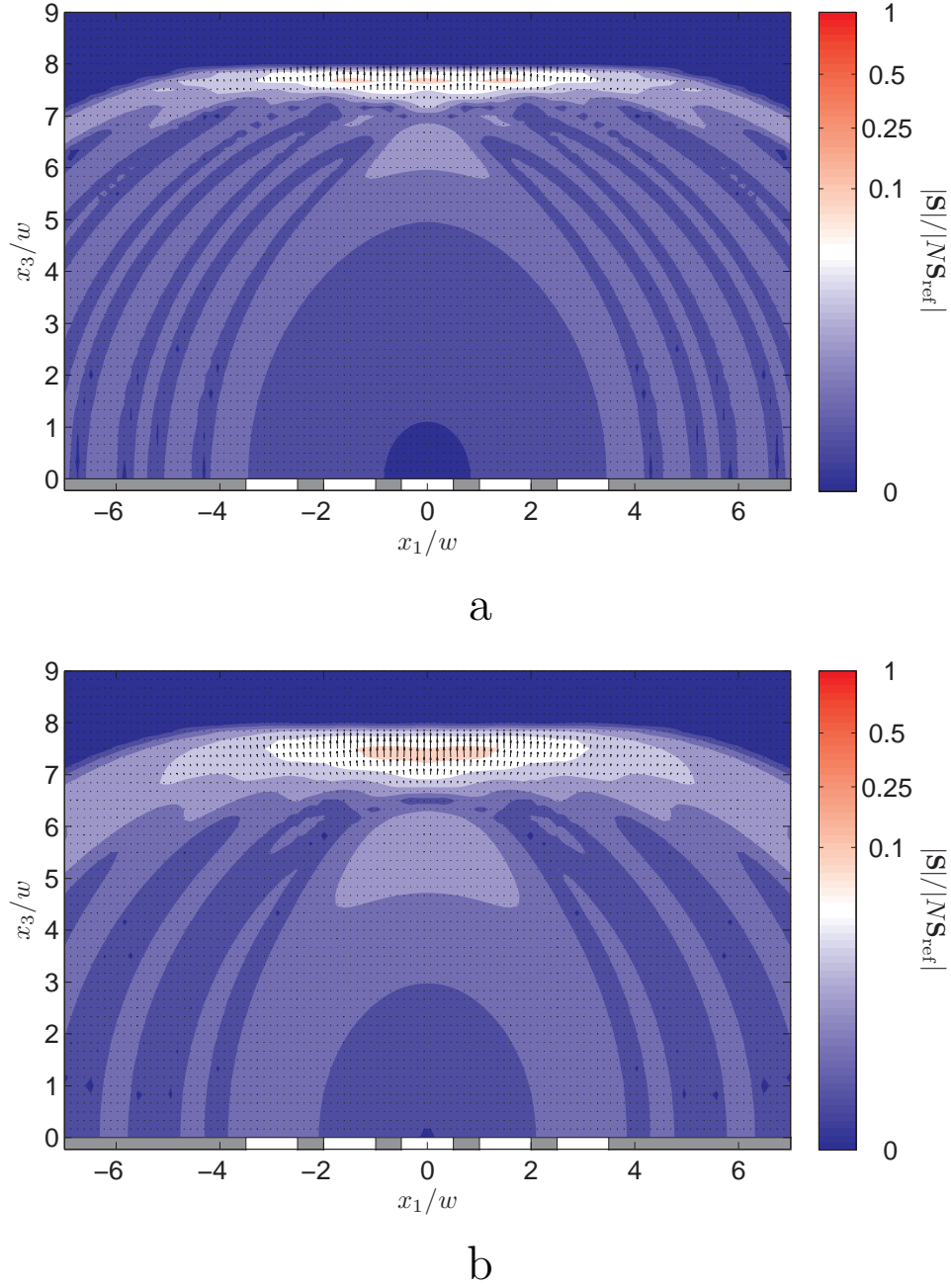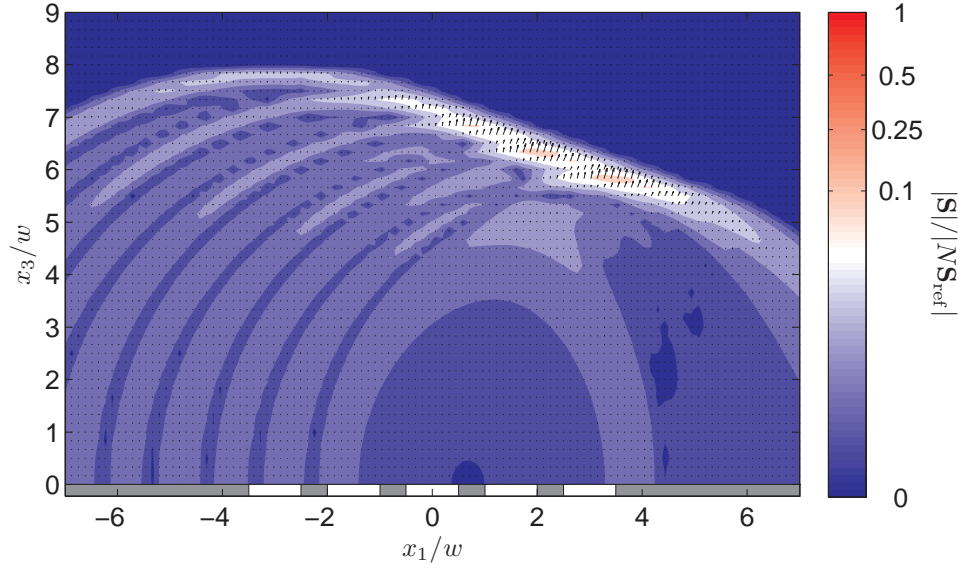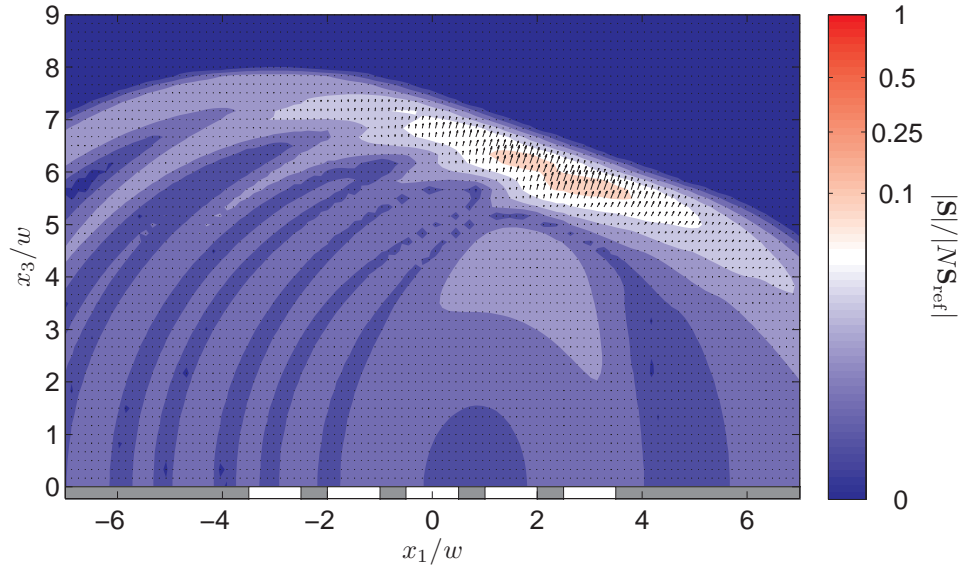
Figure 6.4: Normalized Poynting vectors of EM fields at $c_0 t/w = 4$ for an array of $N = 5$ equally spaced slots of width w and spacing $(a_{n+1} - b_n)/w = 0.5$ for $n = \{1, \ldots, 4\}$, excited with zero time delays and with two sets of excitation pulses with different spatial supports. (a) $c_0 t_w = 0.5542w$; (b) $c_0 t_w = 1.1084w$.
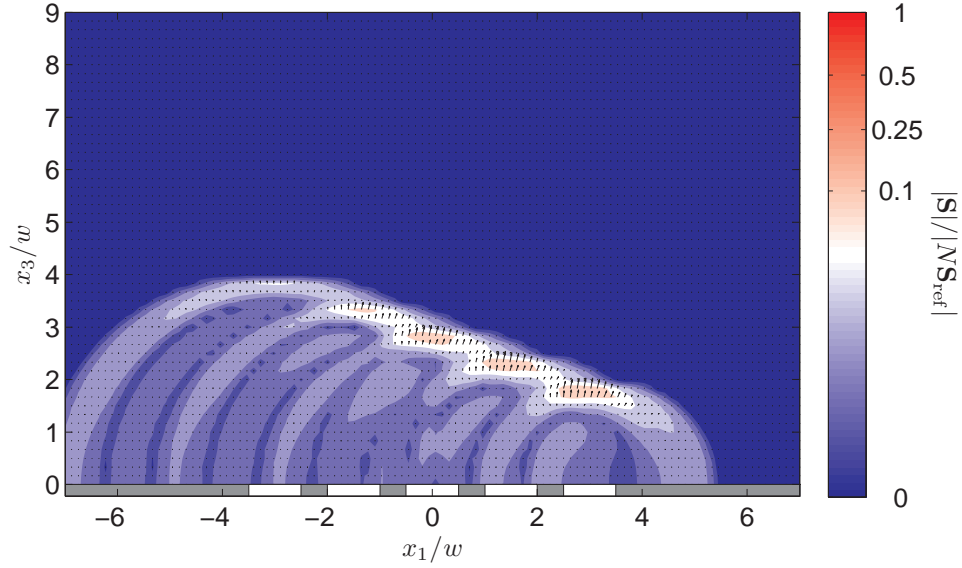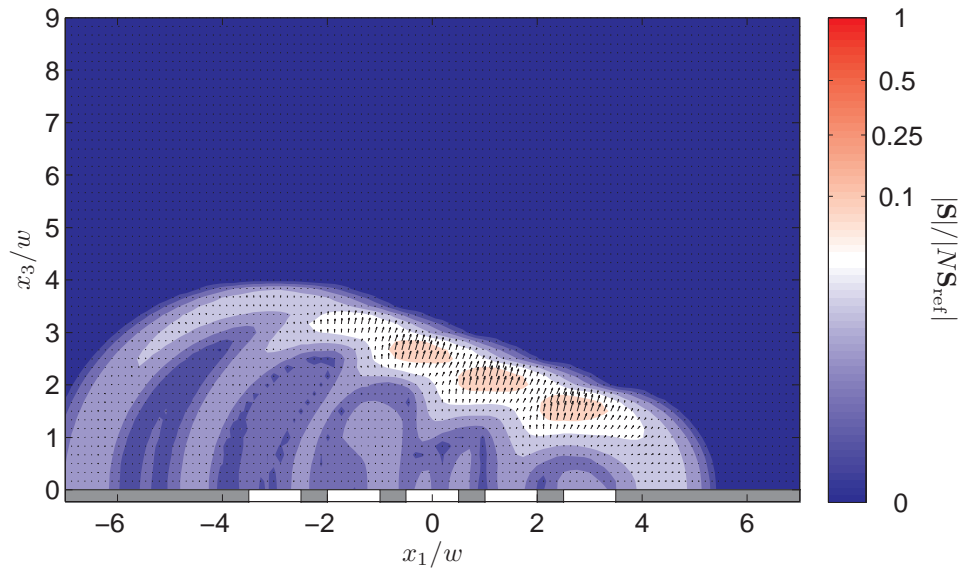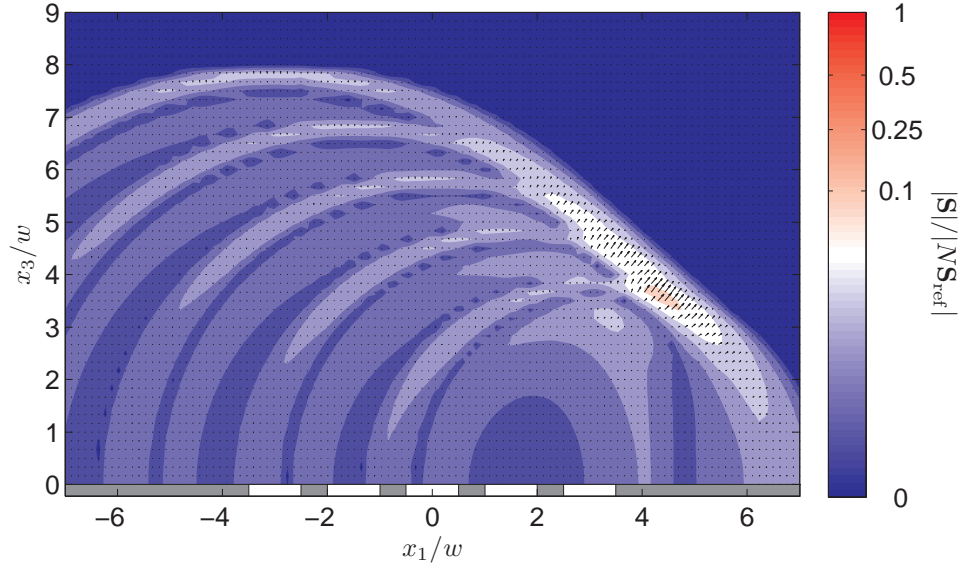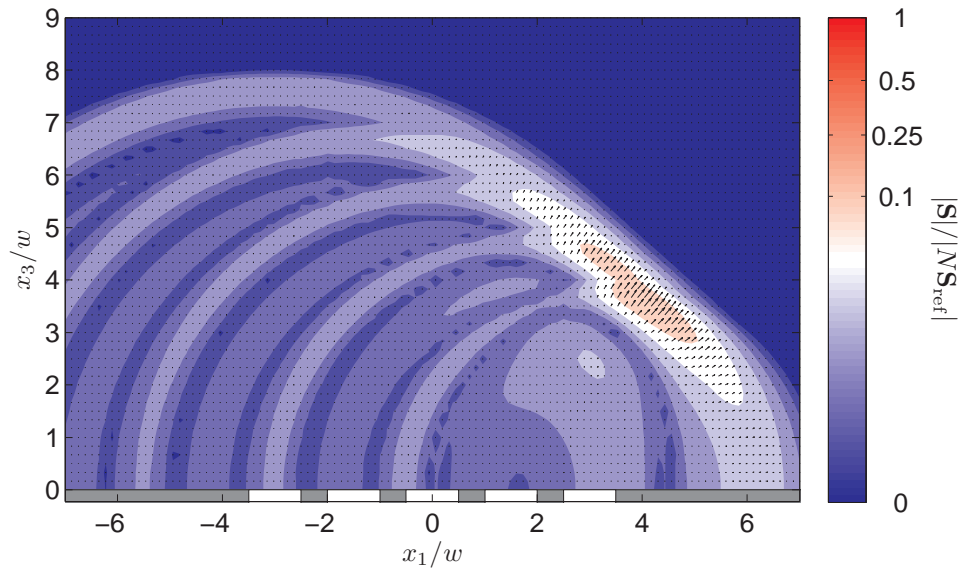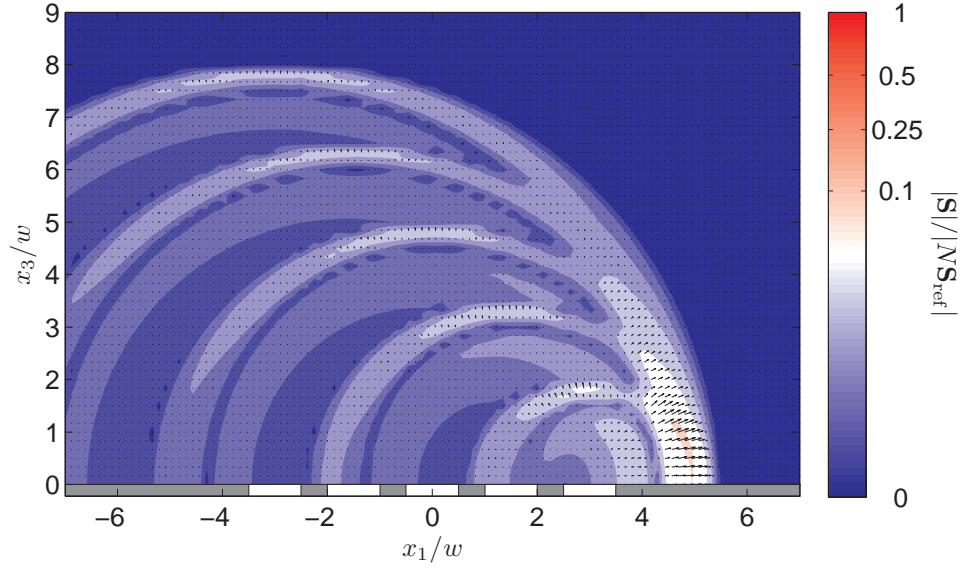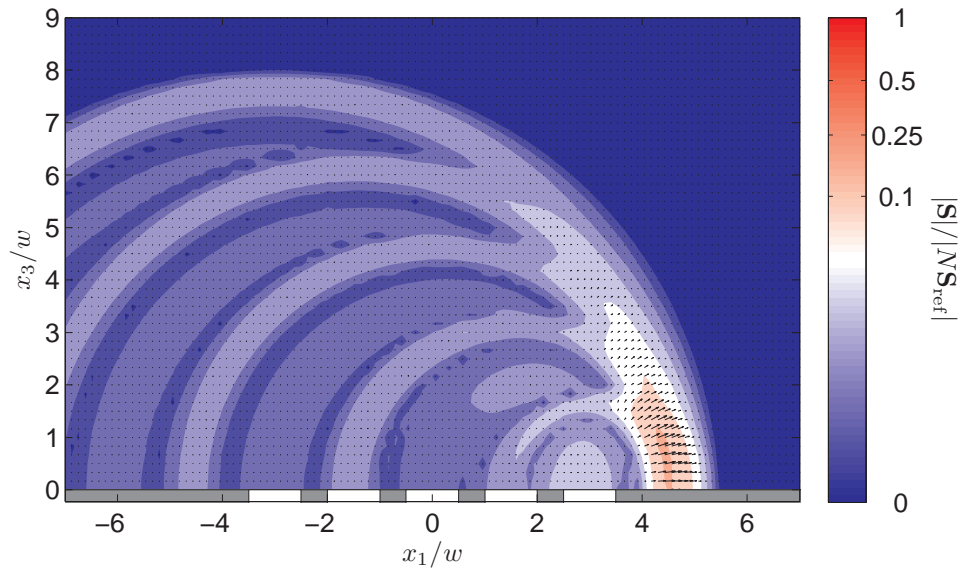
Figure 6.5: Normalized Poynting vectors of EM fields at $c_0 t/w = 4$ for an array of $N = 5$ equally spaced slots of width w and spacing $(a_{n+1} - b_n)/w = 0.5$, excited with $c_0(T_{n+1} - T_n)/w = 0.5$ time delays for $n = \{1, \ldots, 4\}$ and with two sets of excitation pulses with different spatial supports. (a) $c_0 t_{\mathrm{w}} = 0.5542w$; (b) $c_0 t_{\mathrm{w}} = 1.1084w$.
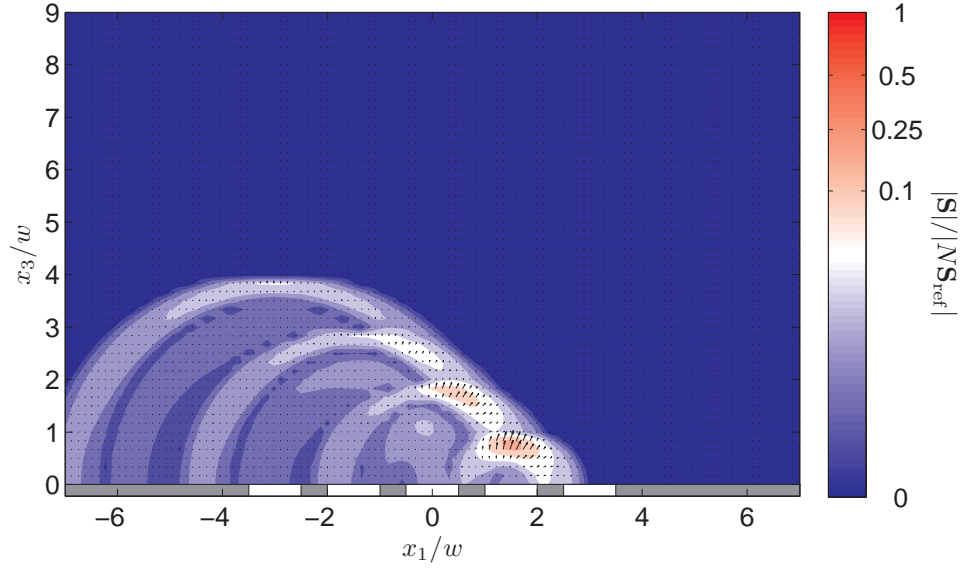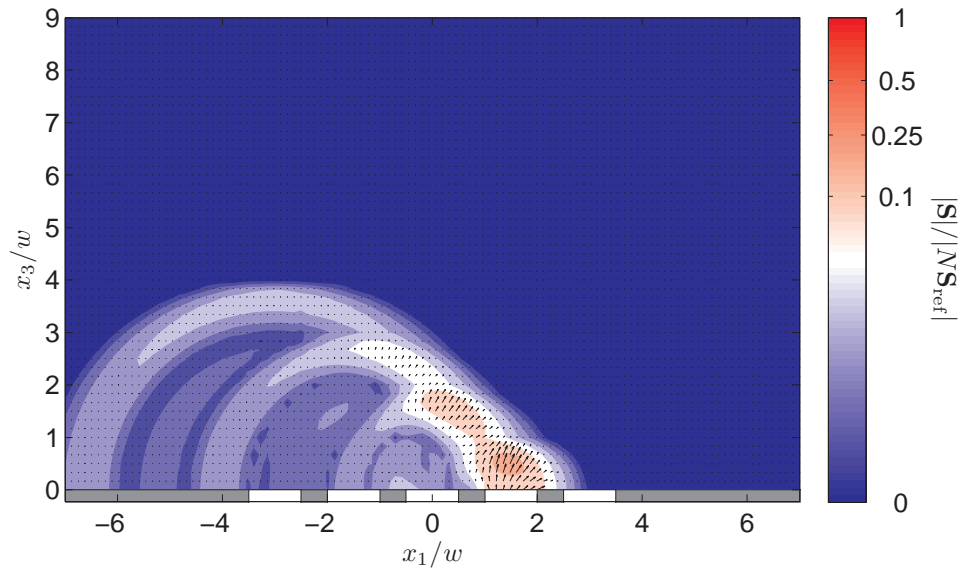
Figure 6.6: Normalized Poynting vectors of EM fields at $c_0 t/w = 4$ for an array of $N = 5$ equally spaced slots of width w and spacing $(a_{n+1} - b_n)/w = 0.5$, excited with $c_0(T_{n+1} - T_n)/w = 1.0$ time delays for $n = \{1, \ldots, 4\}$ and with two sets of excitation pulses with different spatial supports. (a) $c_0 t_{\mathrm{w}} = 0.5542w$; (b) $c_0 t_{\mathrm{w}} = 1.1084w$.
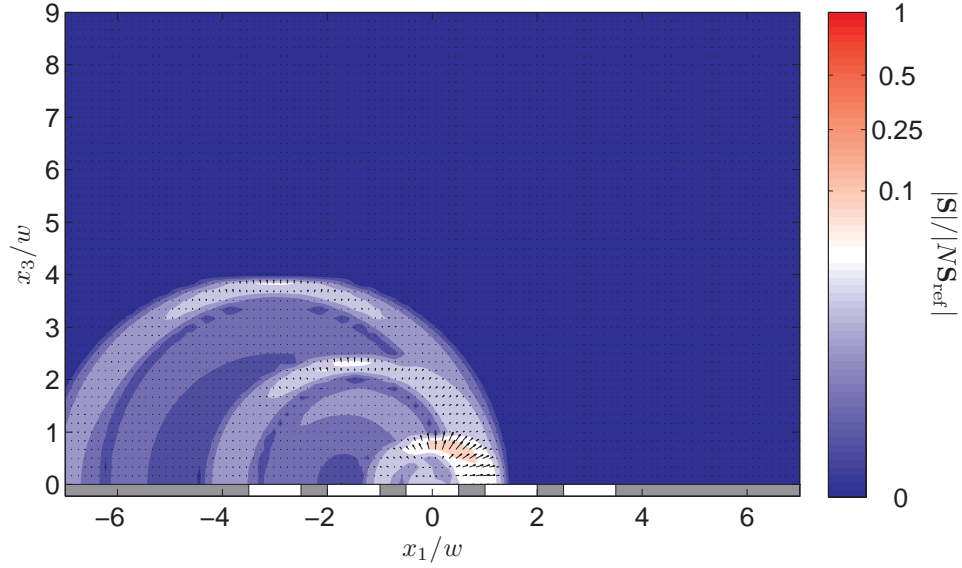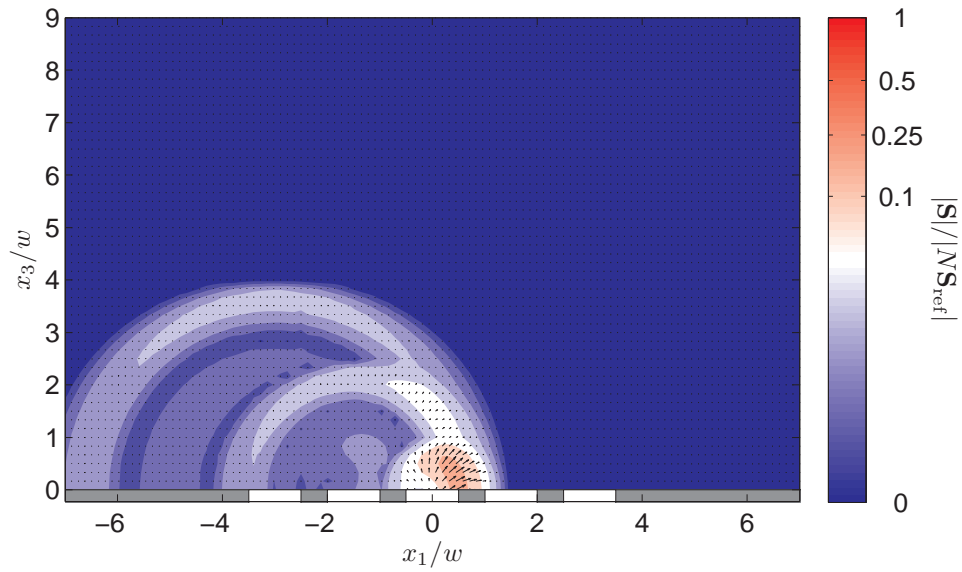
Figure 6.7: Normalized Poynting vectors of EM fields at $c_0 t/w = 4$ for an array of $N = 5$ equally spaced slots of width w and spacing $(a_{n+1} - b_n)/w = 0.5$, excited with $c_0(T_{n+1} - T_n)/w = 1.5$ time delays for $n = \{1, \ldots, 4\}$ and with two sets of excitation pulses with different spatial supports. (a) $c_0 t_w = 0.5542w$; (b) $c_0 t_w = 1.1084w$.

a

b

Figure 6.8: Normalized Poynting vectors of EM fields at $c_0 t/w = 8$ for an array of $N = 5$ equally spaced slots of width w and spacing $(a_{n+1} - b_n)/w = 0.5$ for $n = \{1, \ldots, 4\}$, excited with zero time delays and with two sets of excitation pulses with different spatial supports. (a) $c_0 t_{\mathrm{w}} = 0.5542w$; (b) $c_0 t_{\mathrm{w}} = 1.1084w$.

51

a

b

Figure 6.9: Normalized Poynting vectors of EM fields at $c_0 t/w = 8$ for an array of $N = 5$ equally spaced slots of width w and spacing $(a_{n+1} - b_n)/w = 0.5$, excited with $c_0(T_{n+1} - T_n)/w = 0.5$ time delays for $n = \{1, \ldots, 4\}$ and with two sets of excitation pulses with different spatial supports. (a) $c_0 t_w = 0.5542w$; (b) $c_0 t_w = 1.1084w$.

Figure 6.10: Normalized Poynting vectors of EM fields at $c_0 t/w = 8$ for an array of $N = 5$ equally spaced slots of width w and spacing $(a_{n+1} - b_n)/w = 0.5$, excited with $c_0(T_{n+1} - T_n)/w = 1.0$ time delays for $n = \{1, \ldots, 4\}$ and with two sets of excitation pulses with different spatial supports. (a) $c_0 t_w = 0.5542w$; (b) $c_0 t_w = 1.1084w$.

a

b

Figure 6.11: Normalized Poynting vectors of EM fields at $c_0 t/w = 8$ for an array of $N = 5$ equally spaced slots of width w and spacing $(a_{n+1} - b_n)/w = 0.5$, excited with $c_0(T_{n+1} - T_n)/w = 1.5$ time delays for $n = \{1, \ldots, 4\}$ and with two sets of excitation pulses with different spatial supports. (a) $c_0 t_{\mathrm{w}} = 0.5542w$; (b) $c_0 t_{\mathrm{w}} = 1.1084w$.

Chapter 7

Pulsed electromagnetic field radiation from a wide slot antenna between two parallel planes

Summary

The pulsed electromagnetic field in between two paralell planes excited by a 2D wide slot is analytically investigated via the application of the Cagniard-DeHoop technique. Starting with the description and formulation of the field problem we shall construct the exact pulse shapes for the radiated electromagnetic field components. In conclusion, illustrative numerical examples are presented.

7.1 Introduction

The present chapter aims at providing the description of pulsed electromagnetic field radiation from a wide slot in an unbounded perfectly electrically conducting (PEC) screen. The source excited the structure is modeled as a prescribed distribution of the transverse electric field across the slot of a uniform and finite width. The structure further radiates into the domain in between two PEC parallel planes. If the upper plane is moved far away from the radiating slot, all reflected time-domain constituents become negligible and only outgoing radiated constituents are relevant. In this sense, the solved problem can be considered as a certain generalization of the problem from Chapter 6.

Reflections occur due to the additional screen, and the slowness-domain quantities have to be written as a superposition of constituents each of which admits a closed-form representation attainable with the Cagniard-DeHoop technique as described in Appendix B. It is shown that the wave motion consists of two sets of upgoing and downgoing waves connected with the right and left radiating edges supplemented with the upgoing and downgoing plane waves propagating above the slot.

The problem solved in this chapter was studied by Schelkunoff in the frequency domain [36]. In it, electromagnetic waves between two parallel, perfectly electrically conducting screens are investigated with the aid of the 'Laplace transform method'. In view of the

latter, the electromagnetic field in between the planes is excited by an a-c voltage applied across the slot and the time dependence of electromagnetic field components is supressed by assuming $\exp(\mathrm{i}\omega t)$ time behavior. The excited electromagnetic field components are subsequently represented via the Bromwich contour inversion integral that is solved by means of the residue theorem. This leads to the result consisting of a sum of direct upgoing wave and infinite series of reflected ones, which is intricate from the numerical point of view. Moreover, as the distance between the plates increases, convergence properties of the series become worse. This is usually solved with the help of some of extrapolation techniques [30].

The aproach presented in this chapter is somewhat more general in the sense that the electromagnetic field components are found in the space-time domain, without anticipation of the time-domain behavior of excited electromagnetic field. As a main tool, the combination of a unilateral Laplace transformation with the spatial wave slowness representation is used, which is known as the Cagniard-DeHoop technique. This technique provides the space-time domain expressions that are possible to evaluate within a finite time-window with any prescribed accuracy. Numerical examples that illustrates the influence of the excitation and configurational paramaters are given.

7.2 Description of the configuration and formulation of the field problem

The configuration examined is shown in Fig. 7.1. The configuration consists of two unbounded electrically perfectly conducting screens $\mathcal{S}_1 = \{-\infty < x_1 < \infty, -\infty < x_2 < \infty, x_3 = h\}$ and $\mathcal{S}_2 = \{(-\infty < x_1 < -w/2) \cup (w/2 < x_1 < \infty), -\infty < x_2 < \infty, x_3 = 0\}$ with a feeding aperture $\mathcal{A} = \{-w/2 < x_1 < w/2, -\infty < x_2 < \infty, x_3 = 0\}$ of the finite width $w > 0$. The structure radiates into the domain $\mathcal{D} = \{-\infty < x_1 < \infty, -\infty < x_2 < \infty, 0 < x_3 < h\}$ with scalar electric permittivity and magnetic permeability $\{\epsilon, \mu\}$ and corresponding electromagnetic wave speed $c = (\epsilon\mu)^{-1/2}$.

The antenna aperture is fed by the uniformly distributed, x_2-independent, electric field

$$E_1(x_1, 0, t) = V_0(t)/w \quad \text{in } \mathcal{A} \tag{7.1}$$

where $V_0(t)$ is the feeding 'voltage'. Since the excitation, as well as the configuration, are
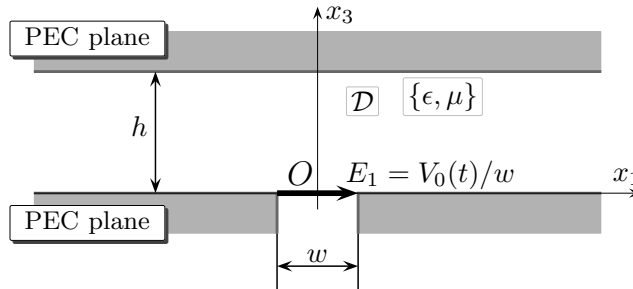
Figure 7.1: Configuration with indication of the aperture feeding.

independent of x_2, the non-zero components of the electric field strength $\{E_1, E_3\}(x_1, x_3, t)$ and the magnetic field strength $H_2(x_1, x_3, t)$ satisfy in $\mathcal{D}$ the source-free field equations (cf. Eqs. (2.5) – (2.7))

$$\partial_1 H_2 - \epsilon \partial_t E_3 = 0 \tag{7.2}$$

$$\partial_3 H_2 + \epsilon \partial_t E_1 = 0 \tag{7.3}$$

$$\partial_1 E_3 - \partial_3 E_1 - \mu \partial_t H_2 = 0 \tag{7.4}$$

The boundary condition of the explicit type requires that

$$\lim_{x_3 \uparrow h} E_1(x_1, x_3, t) = 0 \quad \text{for all } t \text{ and for all } x_1 \tag{7.5}$$

while the excitation condition is (cf. Eq. (2.3))

$$\lim_{x_3 \downarrow 0} E_1(x_1, x_3, t) = [V_0(t)/w]\Pi(x_1/w) \quad \text{for all } t \tag{7.6}$$

where $\Pi(x)$ is the rectangular function (see Eq. (2.4)). It is assumed that $V_0(t)$ starts to act at $t = 0$ and that prior to this instant the field vanishes throughout the configuration.

7.3   Field representations

In view of the Cagniard-DeHoop technique we employ the unilateral Laplace transformation with respect to time

$$\hat{V}_0(s) = \int_{t=0}^{\infty} \exp(-st)V_0(t)\mathrm{d}t \tag{7.7}$$

in which s is taken to be real-valued and positive relying on Lerch's theorem [27], [44]. Further we use the wave slowness field representation

$$\left\{\hat{E}_1, \hat{E}_3, \hat{H}_2\right\}(x_1, x_3, s) = \frac{s}{2\pi\mathrm{i}} \int_{p=-\mathrm{i}\infty}^{\mathrm{i}\infty} \exp(-spx_1) \left\{\tilde{E}_1, \tilde{E}_3, \tilde{H}_2\right\}(p, x_3, s)\mathrm{d}p \tag{7.8}$$

Under these transformations, the field equations (7.2) – (7.4) and the boundary conditions (7.5) – (7.6) transform into

$$-sp\tilde{H}_2 - s\epsilon\tilde{E}_3 = 0 \tag{7.9}$$

$$\partial_3 \tilde{H}_2 + s\epsilon\tilde{E}_1 = 0 \tag{7.10}$$

$$-sp\tilde{E}_3 - \partial_3 \tilde{E}_1 - s\mu\tilde{H}_2 = 0 \tag{7.11}$$

and

$$\lim_{x_3 \uparrow h} \tilde{E}_1(p, x_3, s) = 0 \tag{7.12}$$

$$\lim_{x_3 \downarrow 0} \tilde{E}_1(p, x_3, s) = \frac{\hat{V}_0(s)}{w} \frac{\exp(spw/2) - \exp(-spw/2)}{sp} \tag{7.13}$$

The bounded slowness-domain field quantities follow from (7.9) – (7.13) by expressing them in the form

$$\left\{\tilde{E}_1, \tilde{E}_3, \tilde{H}_2, \right\}(p, x_3, s) = \{\gamma(p)/\epsilon, -p/\epsilon, 1\} A^+(p, s) \exp\left[-s\gamma(p)(x_3 - h)\right]$$
$$+ \{-\gamma(p)/\epsilon, -p/\epsilon, 1\} A^-(p, s) \exp\left[-s\gamma(p)(h - x_3)\right] \qquad (7.14)$$

in which

$$\gamma(p) = (1/c^2 - p^2)^{1/2} \quad \text{with } \mathrm{Re}[\gamma(p)] > 0 \qquad (7.15)$$

for all $p \in \mathbb{C}$. The unknown coefficients result from the application of the boundary conditions (7.12) – (7.13) as

$$A^+(p, s) = A^-(p, s) = \frac{\epsilon}{\gamma(p)} \frac{\tilde{E}_1(p, 0, s)}{\exp[s\gamma(p)h] - \exp[-s\gamma(p)h]} \qquad (7.16)$$

Via the convergent expansion

$$\frac{\exp[s\gamma(p)h]}{\exp[s\gamma(p)h] - \exp[-s\gamma(p)h]} = \sum_{n=0}^{\infty} \exp[-2ns\gamma(p)h] \qquad (7.17)$$

the slowness-domain field quantities can be written as the superposition of constituents each of which admits a closed-form representation attainable with Cagniard-DeHoop technique.

7.4 The time-domain radiated fields

In this section we provide the time-domain fields radiated into the domain $\mathcal{D}$. Using the results of Section 7.3 we express them as

$$\left\{\hat{E}_1, \hat{E}_3, \hat{H}_2\right\}(x_1, x_3, s) = \sum_{n=0}^{\infty} \left\{\hat{E}_1^{[n]}, \hat{E}_3^{[n]}, \hat{H}_2^{[n]}\right\}(x_1, x_3, s) \qquad (7.18)$$

with

$$\left\{\hat{E}_1^{[n]}, \hat{E}_3^{[n]}, \hat{H}_2^{[n]}\right\}(x_1, x_3, s) = \frac{\hat{V}_0(s)}{w} \frac{1}{2\pi\mathrm{i}} \int_{p=-\mathrm{i}\infty}^{\mathrm{i}\infty} \left\{\frac{1}{p}, -\frac{1}{\gamma(p)}, \frac{\epsilon}{p\gamma(p)}\right\}$$
$$\times \left(\exp\{-s[pX_\mathrm{b} + \gamma(p)Z_+]\} - \exp\{-s[pX_\mathrm{a} + \gamma(p)Z_+]\}\right)\mathrm{d}p$$
$$+ \frac{\hat{V}_0(s)}{w} \frac{1}{2\pi\mathrm{i}} \int_{p=-\mathrm{i}\infty}^{\mathrm{i}\infty} \left\{-\frac{1}{p}, -\frac{1}{\gamma(p)}, \frac{\epsilon}{p\gamma(p)}\right\}$$
$$\times \left(\exp\{-s[pX_\mathrm{b} + \gamma(p)Z_-]\} - \exp\{-s[pX_\mathrm{a} + \gamma(p)Z_-]\}\right)\mathrm{d}p \qquad (7.19)$$

where $X_\mathrm{a} = x_1 + w/2$, $X_\mathrm{b} = x_1 - w/2$ and $Z_+ = x_3 + 2nh$, $Z_- = 2(n + 1)h - x_3$. The algebraic parts of the integrands do not contain any propagation coefficient that

differs from the propagation coefficient $\gamma(p)$ in the propagation factors. This has the consequence that the corresponding Cagniard-DeHoop contours for a positive horizontal offset intersect the real p-axis in between $p = 0$ and $p = 1/c$, implying the absence of head-waves. Following the recipe given in Appendix B for $c = c_0 = c_1$, the corresponding time-domain expressions in $\mathcal{D}$ can be found as

$$
\left\{ E_1^{[n]}, E_3^{[n]}, H_2^{[n]} \right\} (x_1, x_3, t) = \frac{V_0(t)}{w} \overset{(t)}{*} \frac{1}{\pi}
$$

$$
\left[\left\{ \frac{Z_+ X_{\mathrm{b}}}{c^2 t^2 - Z_+^2}, -1, \frac{1}{\mu} \frac{X_{\mathrm{b}} t}{c^2 t^2 - Z_+^2} \right\} \frac{H(t - T_{\mathrm{b};+})}{(t^2 - T_{\mathrm{b};+}^2)^{1/2}} \right.
$$

$$
- \left\{ \frac{Z_+ X_{\mathrm{a}}}{c^2 t^2 - Z_+^2}, -1, \frac{1}{\mu} \frac{X_{\mathrm{a}} t}{c^2 t^2 - Z_+^2} \right\} \frac{H(t - T_{\mathrm{a};+})}{(t^2 - T_{\mathrm{a};+}^2)^{1/2}}
$$

$$
+ \left\{ -\frac{Z_- X_{\mathrm{b}}}{c^2 t^2 - Z_-^2}, -1, \frac{1}{\mu} \frac{X_{\mathrm{b}} t}{c^2 t^2 - Z_-^2} \right\} \frac{H(t - T_{\mathrm{b};-})}{(t^2 - T_{\mathrm{b};-}^2)^{1/2}}
$$

$$
- \left\{ -\frac{Z_- X_{\mathrm{a}}}{c^2 t^2 - Z_-^2}, -1, \frac{1}{\mu} \frac{X_{\mathrm{a}} t}{c^2 t^2 - Z_-^2} \right\} \frac{H(t - T_{\mathrm{a};-})}{(t^2 - T_{\mathrm{a};-}^2)^{1/2}} \right]
$$

$$
+ [V_0(t - Z_+/c)/w] \left\{ 1, 0, (\epsilon/\mu)^{1/2} \right\} \Pi(x_1/w)
$$

$$
+ [V_0(t - Z_-/c)/w] \left\{ -1, 0, (\epsilon/\mu)^{1/2} \right\} \Pi(x_1/w) \tag{7.20}
$$

where

$$
T_{\mathrm{a,b};\pm} = (X_{\mathrm{a,b}}^2 + Z_\pm^2)^{1/2}/c. \tag{7.21}
$$

Obviously, the wave motion consists of two sets of upgoing (+) and downgoing (-) time-domain constituents connected with the left (a) and right (b) radiating edge. In the limit $h \to \infty$, i.e. as the upper plane is moved towards infinity, the reflected time-domain constituents become negligible and only the zero-order ($n = 0$) upgoing constituents are relevant. These are consistent with the expressions (6.15) derived in the Chapter 6.

7.5 Illustrative numerical examples

This section provides illustrative numerical examples for the case of two excitation pulses with the same amplitudes and different pulse shapes: $c_0 t_{\mathrm{w}} = 0.9236w$ ($t_r = 0.5h/c_0$) and $c_0 t_{\mathrm{w}} = 0.1847w$ ($t_r = 0.1h/c_0$) for $\nu = 2$ ($t_w/t_r = 1.8473$). These activating pulses are shown in Fig. 7.2, where the normalized time is $c_0 t/w$ and normalized $V(t)$ is $V(t)/V_{\max}$.

All cylindrical wave field constituents contain time-convolution integrals with inverse square-root singularities at the arrival time of the wave. These are numerically handled via a stretching of the variable of integration according to

$$
\tau = T_{\mathrm{a};\pm} \cosh(u) \quad \text{for } 0 < u < \infty \tag{7.22}
$$

with the Jacobian

$$
\frac{\partial \tau}{\partial u} = T_{\mathrm{a};\pm} \sinh(u) = (\tau^2 - T_{\mathrm{a};\pm}^2)^{1/2} \tag{7.23}
$$
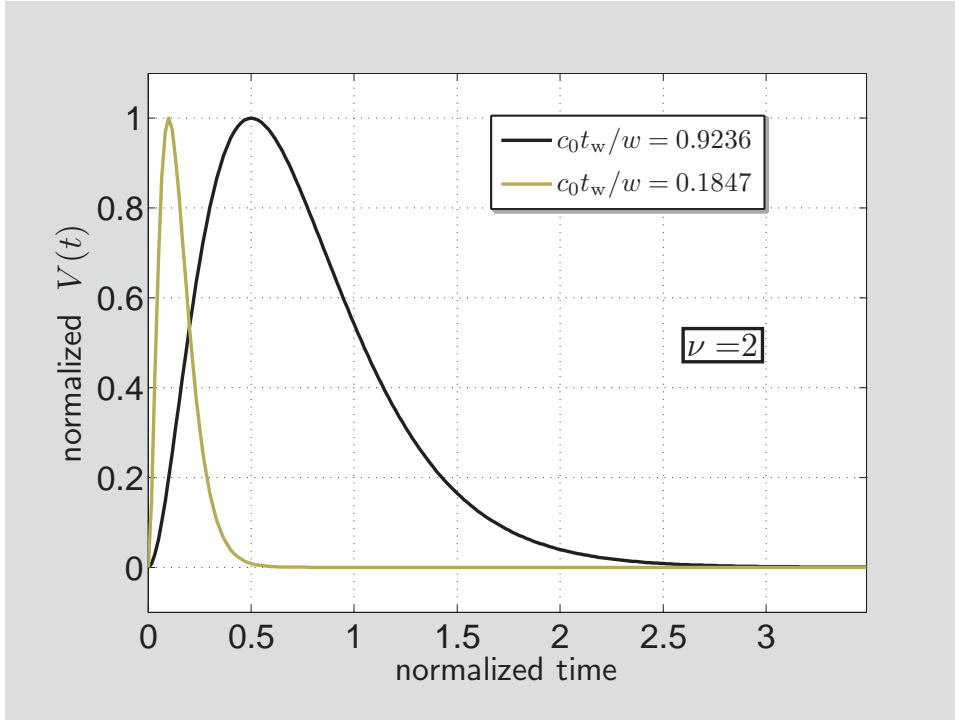
Figure 7.2: Excitation pulse shapes.

The (color) vector density plots Figs. 7.3 – 7.6 show the time snaps of the two-component Poynting vector

$$S_1 = -E_3 H_2 \tag{7.24}$$
$$S_3 = E_1 H_2 \tag{7.25}$$

normalized with respect to

$$|\boldsymbol{S}|_{\text{ref}} = (V_{\text{max}}/w)^2 (\epsilon_0/\mu_0)^{1/2} \tag{7.26}$$

The reference magnitude $|\boldsymbol{S}|_{\text{ref}}$ corresponds to the maximum value of the Poynting vector as it would be carried by a TEM-mode in a parallel-plate waveguide that would be a feeding of the radiating aperture. The spatial domain of observation is taken as $\{-2 \leq x_1/h \leq 2, 0 \leq x_3/h \leq 1\}$ and two observation times are chosen as the vacuum travel time across the distance between the plates (a) $c_0 t/h = 1$ and its double (b) $c_0 t/h = 2$. The width of the slot w and the distance between the parallel plates h are interrelated via $h/w = 1$. Two configurations with different electric permittivity are considered: vacuum $\{\epsilon, \mu\} = \{\epsilon_0, \mu_0\}$ and the dielectric filling with $\{\epsilon, \mu\} = \{4\epsilon_0, \mu_0\}$.

In Fig. 7.3 and Fig. 7.4 we present the time evolution of the Poynting vector in the domain $\mathcal{D}$ filled by vacuum $\{\epsilon, \mu\} = \{\epsilon_0, \mu_0\}$ for two different excitation pulse shapes with different supports $c_0 t_w = 0.9236w$ and $c_0 t_w = 0.1847w$, respectively. In Fig. 7.3a and Fig. 7.4a the wavefront just reaches the upper screen while in Figs. 7.3b and 7.4b the reflected wavefront arrives back at level of the radiating slot. This is more apparent

from the case with the narrower excitation pulse where the radiated beam is spatially more localized and the particular components of the wave motion are therefore more distinguishable.

In order to illustrate the effect of a dielectric filling, the electromagnetic properties of the solution domain $\mathcal{D}$ have been changed to $\{\epsilon, \mu\} = \{4\epsilon_0, \mu_0\}$. Upon comparison of Fig. 7.3 with Fig. 7.5 and Fig. 7.4 with Fig. 7.6 the decrease of wave-speed as well as focusing phenomenom are obvious.
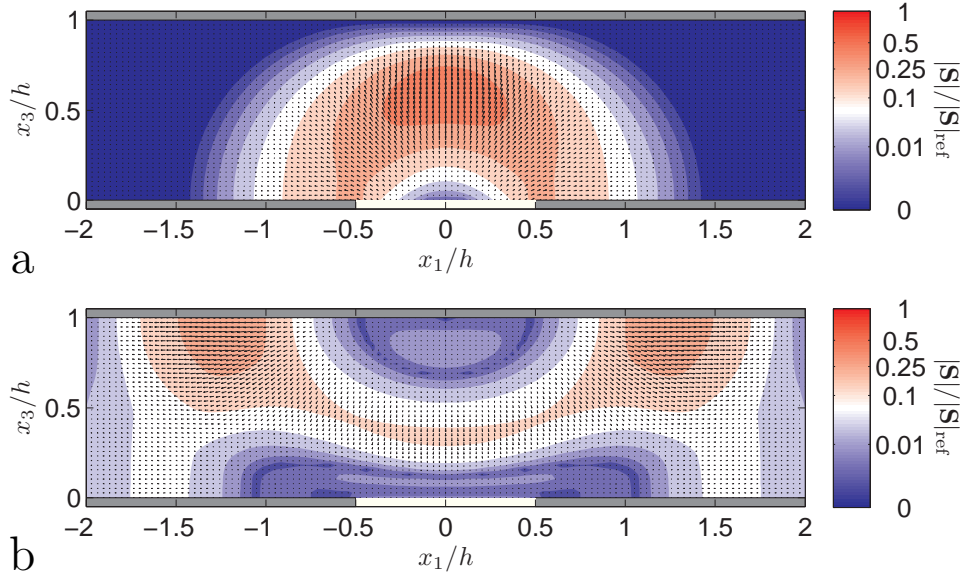
Figure 7.3: Normalized Poynting vector of the EM field at (a) $c_0 t/h = 1.0$; (b) $c_0 t/h = 2.0$. Distance between screens versus slot width is $h/w = 1$ and electromagnetic parameters are $\{\epsilon, \mu\} = \{\epsilon_0, \mu_0\}$ (vacuum). Parameters of the excitation pulse are $c_0 t_w/w = 0.9236$, $\nu = 2$.
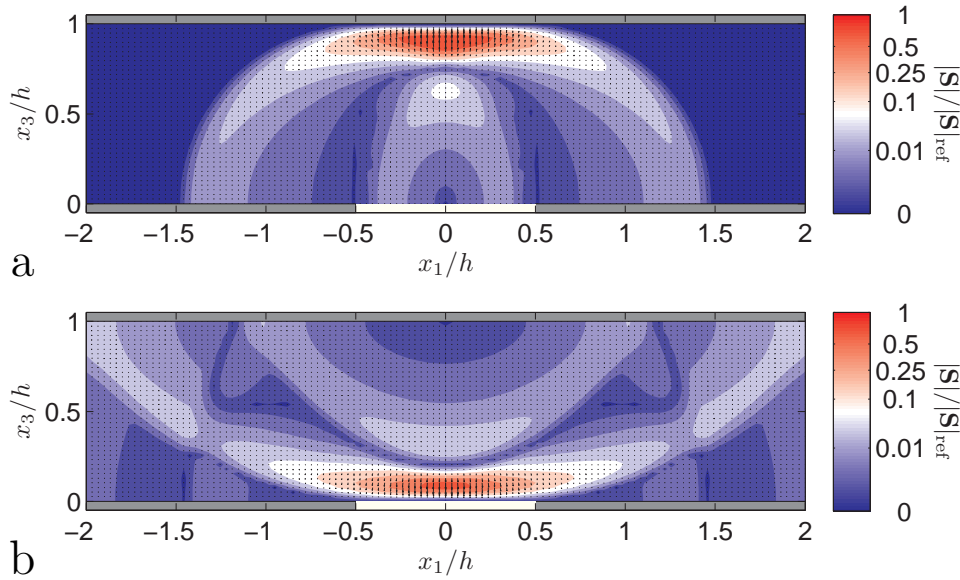
Figure 7.4: Normalized Poynting vector of the EM field at (a) $c_0 t/h = 1.0$; (b) $c_0 t/h = 2.0$. Distance between screens versus slot width is $h/w = 1$ and electromagnetic parameters are $\{\epsilon, \mu\} = \{\epsilon_0, \mu_0\}$ (vacuum). Parameters of the excitation pulse are $c_0 t_w/w = 0.1847$, $\nu = 2$.
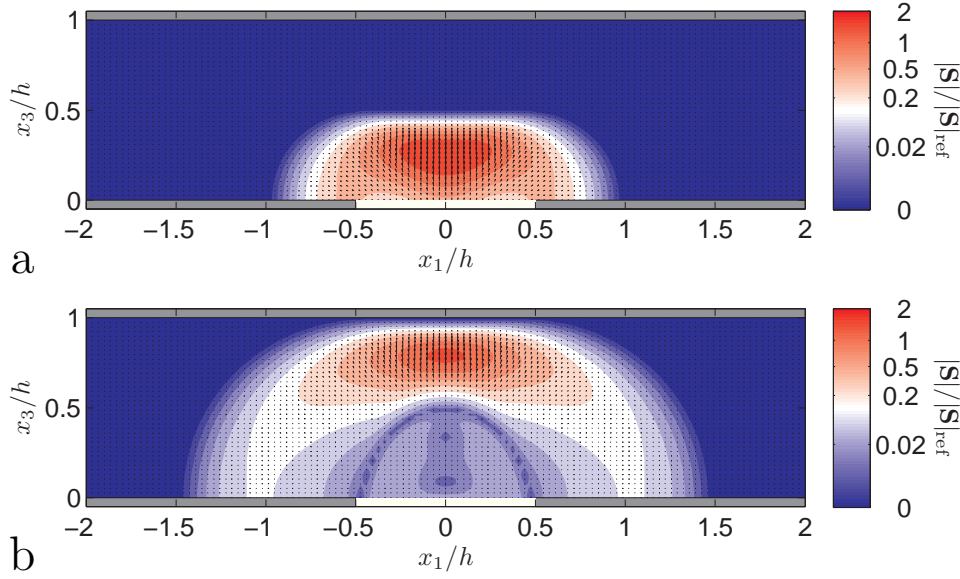
Figure 7.5: Normalized Poynting vector of the EM field at (a) $c_0t/h = 1.0$; (b) $c_0t/h = 2.0$. Distance between screens versus slot width is $h/w = 1$ and electromagnetic parameters are $\{\epsilon, \mu\} = \{4\epsilon_0, \mu_0\}$ (dielectric). Parameters of the excitation pulse are $c_0t_w/w = 0.9236$, $\nu = 2$.
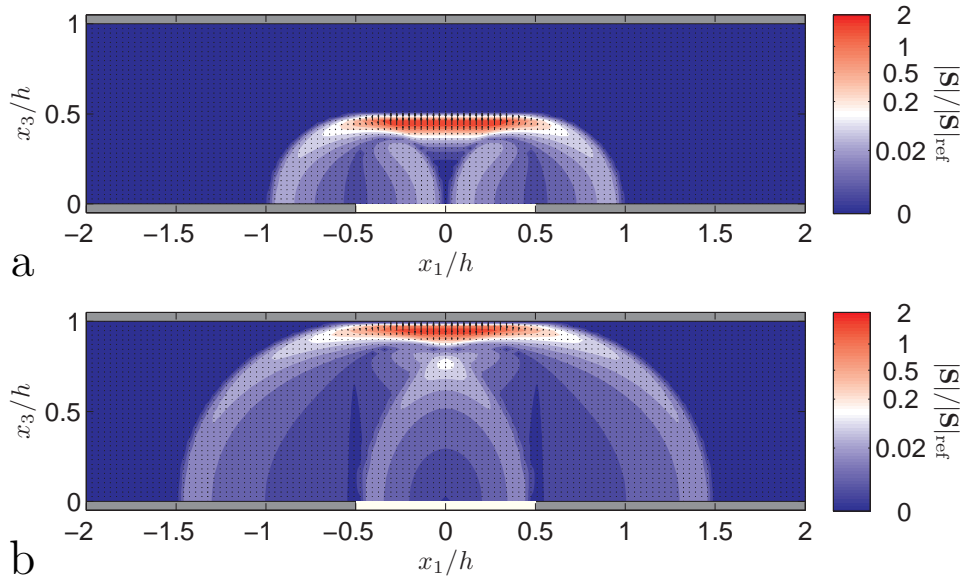
Figure 7.6: Normalized Poynting vector of the EM field at (a) $c_0t/h = 1.0$; (b) $c_0t/h = 2.0$. Distance between screens versus slot width is $h/w = 1$ and electromagnetic parameters are $\{\epsilon, \mu\} = \{4\epsilon_0, \mu_0\}$ (dielectric). Parameters of the excitation pulse are $c_0t_w/w = 0.1847$, $\nu = 2$.

Chapter 8

Pulsed electromagnetic field radiation from a wide slot antenna with a dielectric layer

Summary

The pulsed electromagnetic field radiated by a 2D slot antenna of a finite width covered by a dielectric layer is analytically investigated via the application of the Cagniard-DeHoop technique. Starting with the description and formulation of the field problem we shall arrive at closed-form expressions describing the pulsed field radiation behavior of such problem configuration. In order to illustrate the pulse distortion that results from the presence of the dielectric slab, the conclusions of this chapter are compared with ones from Chapter 6.[4]

8.1   Introduction

With the rapid development of communication systems whose operation is based upon the transfer of pulsed electromagnetic fields and the detection and subsequent interpretation of the pertaining digital signals, there is a need for the mathematical analysis of model configurations where the influence of (a number of) the system parameters on the performance shows up in closed-form analytic expressions that characterize the physical behavior. Parameters in this respect are: the pulse shape of the excitation (characterized by the pulse rise time and the pulse time width of a unipolar pulse), the thickness and the dielectric properties of the slab, the width of the slot, as well as the position of observation relative to the exciting slot. The present chapter aims at providing such a tool with regard to the pulsed radiation behavior of a wide slot antenna covered with a dielectric layer in a two-dimensional setting.

   More precisely, we consider a slot in a perfectly electrically conducting planar screen with a uniform finite width. Across the slot a prescribed distribution of the transverse

electric field is applied. The pulse shape of the exciting field is arbitrary. In front of the slotted plane there is a homogeneous, isotropic dielectric slab of uniform thickness. The structure further radiates into free space.

Upon application of the Cagniard-DeHoop technique, the closed-form and exact expressions describing the radiated pulsed fields as functions of position and time are obtained [19]. It is shown that the excitation via a wide slot shows additional features in that the corners of the waveguide feed show a separate diffractive behavior with accompanying wavefronts. In this case, the wave motion radiated from such slot consists of two sets of upgoing and downgoing cylindrical waves emanating from the edges of the slot in addition to the plane waves propagating and reflecting above the wide slot.

The obtained expressions can serve a purpose of benchmarking the performance of purely computational techniques that have to called upon in the more complicated configurations met in practice, in particular the ones in patch antenna design, where the field in the present chapter represents the field 'incident' on the geometry of the patches located on the dielectric/free-space interface.

The last section provides a number of illustrative numerical examples for a variety of parameters, all chosen such that the pulse time width is smaller than the travel time needed to traverse the slab and such that the separate arrivals from the two edges can be distinguished. This section is divided into three subsections. At first, numerical examples that illustrate the distortion of pulse shapes (of continuous components across the interface) at the vacuum/dielectric interface due to the presence of a dielectric layer are given. The next subsection shows the pulse shapes (of component that jumps across the interface) just below and above the vacuum/dielectric interface. Finally, the time-evolution of the Poynting vector in the dielectric layer, dielectric/vacuum interface and in vacuum is given. This example is further supplemented with the illustration of Cagniard-DeHoop paths connected with the observation point in the vacuum half-space for the first two wave constituents.

8.2   Description of the configuration and formulation of the field problem

The configuration examined is shown in Fig. 8.1. The configuration consists of an unbounded electrically perfectly conducting screen $\mathcal{S} = \{(-\infty < x_1 < -w/2) \cup (w/2 < x_1 < \infty), -\infty < x_2 < \infty, x_3 = 0\}$ with a feeding aperture $\mathcal{A} = \{-w/2 < x_1 < w/2, -\infty < x_2 < \infty, x_3 = 0\}$ of the finite width $w > 0$. The covering dielectric slab occupies the domain $\mathcal{D}_1 = \{-\infty < x_1 < \infty, -\infty < x_2 < \infty, 0 < x_3 < d\}$. The structure radiates into the vacuum half-space $\mathcal{D}_0 = \{-\infty < x_1 < \infty, -\infty < x_2 < \infty, d < x_3 < \infty\}$. The spatial distribution of electric permittivity and magnetic permeability is

$$\{\epsilon, \mu\} = \begin{cases} \{\epsilon_0, \mu_0\} & \text{in } \mathcal{D}_0 \\ \{\epsilon_1, \mu_1\} & \text{in } \mathcal{D}_1 \end{cases} \tag{8.1}$$

The corresponding electromagnetic wave speeds and characteristic admitances are $c_0 = (\epsilon_0 \mu_0)^{-1/2}$, $c_1 = (\epsilon_1 \mu_1)^{-1/2}$ and $\eta_0 = (\epsilon_0/\mu_0)^{1/2}$, $\eta_1 = (\epsilon_1/\mu_1)^{1/2}$, respectively. The antenna
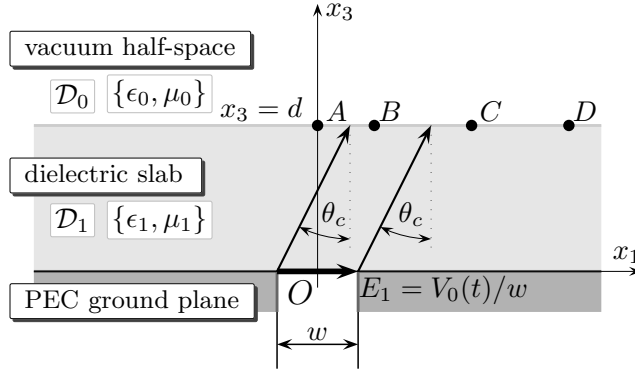
Figure 8.1: Configuration with indication of the critical angle $\theta_c = \arcsin(c_1/c_0)$. Positions of the observation points $\{B, C, D\}$ are not true-to-scale with those chosen in Section 8.5.

aperture is fed by the uniformly distributed, x_2-independent, electric field

$$E_1(x_1, 0, t) = V_0(t)/w \quad \text{in } \mathcal{A} \tag{8.2}$$

where $V_0(t)$ is the feeding 'voltage'. Since the excitation, as well as the configuration, are independent of x_2, the non-zero components of the electric field strength $\{E_1, E_3\}(x_1, x_3, t)$ and the magnetic field strength $H_2(x_1, x_3, t)$ satisfy in $\mathcal{D}_0$ and $\mathcal{D}_1$ the source-free field equations (cf. Eqs. (2.5) – (2.7))

$$\partial_1 H_2 - \epsilon \partial_t E_3 = 0 \tag{8.3}$$

$$\partial_3 H_2 + \epsilon \partial_t E_1 = 0 \tag{8.4}$$

$$\partial_1 E_3 - \partial_3 E_1 - \mu \partial_t H_2 = 0 \tag{8.5}$$

The interface boundary conditions require that

$$\lim_{x_3 \downarrow d} E_1(x_1, x_3, t) = \lim_{x_3 \uparrow d} E_1(x_1, x_3, t) \quad \text{for all } x_1 \text{ and } t \tag{8.6}$$

$$\lim_{x_3 \downarrow d} H_2(x_1, x_3, t) = \lim_{x_3 \uparrow d} H_2(x_1, x_3, t) \quad \text{for all } x_1 \text{ and } t \tag{8.7}$$

while the excitation condition is (cf. Eq. (2.3))

$$\lim_{x_3 \downarrow 0} E_1(x_1, x_3, t) = [V_0(t)/w]\Pi(x_1/w) \quad \text{for all } t \tag{8.8}$$

with $\Pi(x)$ denoting the rectangular function (see Eq. (2.4)). It is assumed that $V_0(t)$ starts to act at $t = 0$ and that prior to this instant the field vanishes throughout the configuration.

8.3 Field representations

The Cagniard-DeHoop technique employs a unilateral Laplace transformation with respect to time of the type

$$\hat{V}_0(s) = \int_{t=0}^{\infty} \exp(-st)V_0(t)\mathrm{d}t \tag{8.9}$$

66

in which s is taken to be real-valued and positive relying on Lerch's theorem [27, 44] . The next step is to use the slowness representation of the field quantities

$$\left\{\hat{E}_1, \hat{E}_3, \hat{H}_2\right\}(x_1, x_3, s) = \frac{s}{2\pi\mathrm{i}} \int_{p=-\mathrm{i}\infty}^{\mathrm{i}\infty} \exp(-spx_1) \left\{\tilde{E}_1, \tilde{E}_3, \tilde{H}_2\right\}(p, x_3, s)\mathrm{d}p \qquad (8.10)$$

that involves imaginary values of the complex slowness parameter p. Using (8.9) and (8.10), the field equations (8.3)–(8.5) transform into

$$-sp\tilde{H}_2 - s\epsilon\tilde{E}_3 = 0 \qquad (8.11)$$

$$\partial_3\tilde{H}_2 + s\epsilon\tilde{E}_1 = 0 \qquad (8.12)$$

$$-sp\tilde{E}_3 - \partial_3\tilde{E}_1 - s\mu\tilde{H}_2 = 0 \qquad (8.13)$$

the interface boundary conditions (8.6) and (8.7) into

$$\lim_{x_3\downarrow d} \tilde{E}_1(p, x_3, s) = \lim_{x_3\uparrow d} \tilde{E}_1(p, x_3, s) \qquad (8.14)$$

$$\lim_{x_3\downarrow d} \tilde{H}_2(p, x_3, s) = \lim_{x_3\uparrow d} \tilde{H}_2(p, x_3, s) \qquad (8.15)$$

and the excitation condition (8.8) into

$$\lim_{x_3\downarrow 0} \tilde{E}_1(p, x_3, s) = \frac{\hat{V}_0(s)}{w} \frac{\exp(spw/2) - \exp(-spw/2)}{sp} \qquad (8.16)$$

The slowness-domain field quantities follow from (8.11) – (8.16) by expressing them in the form

$$\left\{\tilde{E}_1, \tilde{E}_3, \tilde{H}_2\right\}(p, x_3, s) = \left\{\gamma_0(p)/\epsilon_0, -p/\epsilon_0, 1\right\} A_0^+(p, s) \exp\left[-s\gamma_0(p)(x_3 - d)\right] \quad \text{in } \mathcal{D}_0 \qquad (8.17)$$

and

$$\left\{\tilde{E}_1, \tilde{E}_3, \tilde{H}_2\right\}(p, x_3, s) = \left\{\gamma_1(p)/\epsilon_1, -p/\epsilon_1, 1\right\} A_1^+(p, s) \exp\left[-s\gamma_1(p)x_3\right]$$
$$+ \left\{-\gamma_1(p)/\epsilon_1, -p/\epsilon_1, 1\right\} A_1^-(p, s) \exp\left[-s\gamma_1(p)(d - x_3)\right] \quad \text{in } \mathcal{D}_1 \qquad (8.18)$$

in which

$$\gamma_{0,1}(p) = \left(1/c_{0,1}^2 - p^2\right)^{1/2} \quad \text{with } \mathrm{Re}\left[\gamma_{0,1}(p)\right] > 0 \quad \text{for all } p \in \mathbb{C} \qquad (8.19)$$

Using these expressions in (8.14) – (8.16) it is found that

$$A_1^+(p, s) = \frac{\epsilon_1}{\gamma_1(p)} \tilde{E}_1(p, 0, s) \frac{1}{\Delta} \qquad (8.20)$$

$$A_1^-(p, s) = \frac{\epsilon_1}{\gamma_1(p)} \tilde{E}_1(p, 0, s) \frac{R_H(p) \exp[-s\gamma_1(p)d]}{\Delta} \qquad (8.21)$$

$$A_0^+(p, s) = \frac{\epsilon_1}{\gamma_1(p)} \tilde{E}_1(p, 0, s) \frac{T_H(p) \exp[-s\gamma_1(p)d]}{\Delta} \qquad (8.22)$$

in which

$$R_H(p) = \frac{\gamma_1(p)/\epsilon_1 - \gamma_0(p)/\epsilon_0}{\gamma_1(p)/\epsilon_1 + \gamma_0(p)/\epsilon_0} \tag{8.23}$$

$$T_H(p) = \frac{2\,\gamma_1(p)/\epsilon_1}{\gamma_1(p)/\epsilon_1 + \gamma_0(p)/\epsilon_0} \tag{8.24}$$

$$\Delta = 1 - R_H(p)\exp[-2s\gamma_1(p)d] \tag{8.25}$$

Via the convergent expansion

$$\frac{1}{\Delta} = \sum_{n=0}^{\infty} [R_H(p)]^n \exp\left[-2snd\gamma_1(p)\right] \tag{8.26}$$

the slowness-domain field quantities can be written as the superposition of constituents each of which admits a closed-form representation attainable with Cagniard-DeHoop method

$$\left\{\hat{E}_1, \hat{E}_3, \hat{H}_2\right\}(x_1, x_3, s) = \sum_{n=0}^{\infty} \left\{\hat{E}_1^{[n]}, \hat{E}_3^{[n]}, \hat{H}_2^{[n]}\right\}(x_1, x_3, s) \tag{8.27}$$

8.4 The time-domain field in the dielectric layer

In this section we focus on the time-domain constituents of the fields components propagating in the dielectric slab $\mathcal{D}_1$. Using the results of Section 8.3 we express them as

$$\left\{\hat{E}_1^{[n]}, \hat{E}_3^{[n]}, \hat{H}_2^{[n]}\right\}(x_1, x_3, s) = \frac{\hat{V}_0(s)}{w}\frac{1}{2\pi\mathrm{i}}\int_{p=-\mathrm{i}\infty}^{\mathrm{i}\infty} \left\{\frac{1}{p}, -\frac{1}{\gamma_1(p)}, \frac{\epsilon_1}{p\gamma_1(p)}\right\}[R_H(p)]^n$$

$$\times \left(\exp\{-s[pX_\mathrm{b} + \gamma_1(p)Z_+]\} - \exp\{-s[pX_\mathrm{a} + \gamma_1(p)Z_+]\}\right)\mathrm{d}p$$

$$+ \frac{\hat{V}_0(s)}{w}\frac{1}{2\pi\mathrm{i}}\int_{p=-\mathrm{i}\infty}^{\mathrm{i}\infty} \left\{-\frac{1}{p}, -\frac{1}{\gamma_1(p)}, \frac{\epsilon_1}{p\gamma_1(p)}\right\}[R_H(p)]^{n+1}$$

$$\times \left(\exp\{-s[pX_\mathrm{b} + \gamma_1(p)Z_-]\} - \exp\{-s[pX_\mathrm{a} + \gamma_1(p)Z_-]\}\right)\mathrm{d}p \tag{8.28}$$

where $X_\mathrm{a} = x_1 + w/2$, $X_\mathrm{b} = x_1 - w/2$ and $Z_+ = x_3 + 2nd$, $Z_- = 2(n+1)d - x_3$. Obviously, the expressions represent two sets of upgoing and two sets of downgoing waves. The latter waves, as well as subsequent reflected upgoing waves, disappear as the contrast in electromagnetic properties between $\mathcal{D}_0$ and $\mathcal{D}_1$ vanishes. Since the propagation terms in (8.28) do not contain the propagation coefficient $\gamma_0(p)$, which, for the standard case $c_0 > c_1$, implies the possible occurence of head-waves. The corresponding time-domain expressions of each of these constituents follow upon the application of the Cagniard-DeHoop technique as described in Appendix B. In this way, the body-wave time-domain constituents can be written as

$$\left\{E_1^{\mathrm{BW};[n]}, E_3^{\mathrm{BW};[n]}, H_2^{\mathrm{BW};[n]}\right\}(x_1, x_3, t) = [V_0(t)/w] \overset{(t)}{*} \pi^{-1}$$

$$\times \left(\left\{e_{1\mathrm{b}}^{\mathrm{BW};[n]+} - e_{1\mathrm{a}}^{\mathrm{BW};[n]+}, e_{3\mathrm{b}}^{\mathrm{BW};[n]+} - e_{3\mathrm{a}}^{\mathrm{BW};[n]+}, h_{2\mathrm{b}}^{\mathrm{BW};[n]+} - h_{2\mathrm{a}}^{\mathrm{BW};[n]+}\right\}(x_1, x_3, t)\right.$$

$$\left. + \left\{e_{1\mathrm{b}}^{\mathrm{BW};[n]-} - e_{1\mathrm{a}}^{\mathrm{BW};[n]-}, e_{3\mathrm{b}}^{\mathrm{BW};[n]-} - e_{3\mathrm{a}}^{\mathrm{BW};[n]-}, h_{2\mathrm{b}}^{\mathrm{BW};[n]-} - h_{2\mathrm{a}}^{\mathrm{BW};[n]-}\right\}(x_1, x_3, t)\right) \tag{8.29}$$

with

$$
\left\{ e_{1a}^{\text{BW};[n]+}, e_{3a}^{\text{BW};[n]+}, h_{2a}^{\text{BW};[n]+} \right\} (x_1, x_3, t)
$$
$$
= \text{Re} \left(\left\{ \gamma_1 \left(p_a^{\text{BW}+} \right) / p_a^{\text{BW}+}, -1, \epsilon_1 / p_a^{\text{BW}+} \right\} \left[R_H \left(p_a^{\text{BW}+} \right) \right]^n \right)
$$
$$
\times H \left(t - T_{\text{BWa}+}^{[n]} \right) \left(t^2 - T_{\text{BWa}+}^{[n]2} \right)^{-1/2}
\tag{8.30}
$$

$$
\left\{ e_{1a}^{\text{BW};[n]-}, e_{3a}^{\text{BW};[n]-}, h_{2a}^{\text{BW};[n]-} \right\} (x_1, x_3, t)
$$
$$
= \text{Re} \left(\left\{ -\gamma_1 \left(p_a^{\text{BW}-} \right) / p_a^{\text{BW}-}, -1, \epsilon_1 / p_a^{\text{BW}-} \right\} \left[R_H \left(p_a^{\text{BW}-} \right) \right]^{n+1} \right)
$$
$$
\times H \left(t - T_{\text{BWa}-}^{[n]} \right) \left(t^2 - T_{\text{BWa}-}^{[n]2} \right)^{-1/2}
\tag{8.31}
$$

where $p_a^{\text{BW}\pm} = p_a^{\text{BW}\pm}(X_a, Z_\pm, t)$ is given as

$$
p_a^{\text{BW}\pm} = \left\{ X_a t + \mathrm{i} Z_\pm \left(t^2 - T_{\text{BWa}\pm}^{[n]2} \right)^{1/2} \right\} / \left\{ X_a^2 + Z_\pm^2 \right\}
\tag{8.32}
$$

with

$$
T_{\text{BWa}\pm}^{[n]} = (X_a^2 + Z_\pm^2)^{1/2} / c_1
\tag{8.33}
$$

In the range where $X_{a,b}/(X_{a,b}^2 + Z_\pm^2)^{1/2} > c_1/c_0$ is satisfied, the head-wave time-domain constituents are present

$$
\left\{ E_1^{\text{HW};[n]}, E_3^{\text{HW};[n]}, H_2^{\text{HW};[n]} \right\} (x_1, x_3, t) = [V_0(t)/w] \overset{(t)}{*} \pi^{-1}
$$
$$
\times \Bigg(\left\{ e_{1b}^{\text{HW};[n]+} - e_{1a}^{\text{HW};[n]+}, e_{3b}^{\text{HW};[n]+} - e_{3a}^{\text{HW};[n]+}, h_{2b}^{\text{HW};[n]+} - h_{2a}^{\text{HW};[n]+} \right\} (x_1, x_3, t)
$$
$$
+ \left\{ e_{1b}^{\text{HW};[n]-} - e_{1a}^{\text{HW};[n]-}, e_{3b}^{\text{HW};[n]-} - e_{3a}^{\text{HW};[n]-}, h_{2b}^{\text{HW};[n]-} - h_{2a}^{\text{HW};[n]-} \right\} (x_1, x_3, t) \Bigg)
\tag{8.34}
$$

with

$$
\left\{ e_{1a}^{\text{HW};[n]+}, e_{3a}^{\text{HW};[n]+}, h_{2a}^{\text{HW};[n]+} \right\} (x_1, x_3, t)
$$
$$
= \text{Im} \left[\left\{ \gamma_1 \left(p_a^{\text{HW}+} \right) / p_a^{\text{HW}+}, -1, \epsilon_1 / p_a^{\text{HW}+} \right\} \left[R_H \left(p_a^{\text{HW}+} \right) \right]^n \right]
$$
$$
\times \Pi \left[\left(t - T_{\text{Ca}+}^{[n]} \right) / T_{\text{La}+}^{[n]} \right] \left(T_{\text{BWa}+}^{[n]2} - t^2 \right)^{-1/2}
\tag{8.35}
$$

and

$$
\left\{ e_{1a}^{\text{HW};[n]-}, e_{3a}^{\text{HW};[n]-}, h_{2a}^{\text{HW};[n]-} \right\} (x_1, x_3, t)
$$
$$
= \text{Im} \left[\left\{ -\gamma_1 \left(p_a^{\text{HW}-} \right) / p_a^{\text{HW}-}, -1, \epsilon_1 / p_a^{\text{HW}-} \right\} \left[R_H \left(p_a^{\text{HW}-} \right) \right]^{n+1} \right]
$$
$$
\times \Pi \left[\left(t - T_{\text{Ca}-}^{[n]} \right) / T_{\text{La}-}^{[n]} \right] \left(T_{\text{BWa}-}^{[n]2} - t^2 \right)^{-1/2}
\tag{8.36}
$$

69

where $\Pi(x)$ denotes the rectangular function and $p_{\mathrm{a}}^{\mathrm{HW}\pm} = p_{\mathrm{a}}^{\mathrm{HW}\pm}(X_{\mathrm{a}}, Z_{\pm}, t)$ is given as

$$p_{\mathrm{a}}^{\mathrm{HW}\pm} = \left\{ X_{\mathrm{a}} t - Z_{\pm} \left(T_{\mathrm{BWa}\pm}^{[n]2} - t^2 \right)^{1/2} \right\} / \left\{ X_{\mathrm{a}}^2 + Z_{\pm}^2 \right\} \tag{8.37}$$

with

$$T_{\mathrm{HWa}\pm}^{[n]} = X_{\mathrm{a}}/c_0 + Z_{\pm} \left(1/c_1^2 - 1/c_0^2 \right)^{1/2} \tag{8.38}$$

$$T_{\mathrm{Ca}\pm}^{[n]} = \left(T_{\mathrm{HWa}\pm}^{[n]} + T_{\mathrm{BWa}\pm}^{[n]} \right) / 2 \tag{8.39}$$

$$T_{\mathrm{La}\pm}^{[n]} = T_{\mathrm{BWa}\pm}^{[n]} - T_{\mathrm{HWa}\pm}^{[n]} \tag{8.40}$$

The expressions connected with the edge $x_1 = b = w/2$ are similar with those corresponding to $x_1 = a = -w/2$, only with 'a' replaced with 'b'. In addition, if the observer is above the slot, i.e. if $|x_1| \leq w/2$, then upgoing and downgoing plane-waves have to be included

$$\left\{ E_1^{\mathrm{PW};[n]}, E_3^{\mathrm{PW};[n]}, H_2^{\mathrm{PW};[n]} \right\} (x_1, x_3, t) = \left\{ [R_H(0)]^n \{1, 0, \eta_1\} V_0(t - Z_+/c_1)/w \right.$$
$$\left. + [R_H(0)]^{n+1} \{-1, 0, \eta_1\} V_0(t - Z_-/c_1)/w \right\} \Pi(x_1/w) \tag{8.41}$$

8.5 The time-domain field at the vacuum/dielectric interface

In this section we focus on those field components at the interface $x_3 = d$ that are continuous across this interface, i.e. E_1 and H_2. In fact, the radiated field in $\mathcal{D}_0$ can be easily expressed in terms of these field values. Using the results of Section 8.3 we express them as

$$\left\{ \hat{E}_1^{[n]}, \hat{H}_2^{[n]} \right\} (x_1, d, s) = \frac{\hat{V}_0(s)}{w} \frac{1}{2\pi\mathrm{i}} \int_{p=-\mathrm{i}\infty}^{\mathrm{i}\infty} \left\{ \frac{\epsilon_1 \gamma_0(p)}{\epsilon_0 p \gamma_1(p)}, \frac{\epsilon_1}{p \gamma_1(p)} \right\} T_H(p) [R_H(p)]^n$$
$$\times \left(\exp\{-s[pX_{\mathrm{b}} + \gamma_1(p)(2n+1)d]\} - \exp\{-s[pX_{\mathrm{a}} + \gamma_1(p)(2n+1)d]\} \right) \mathrm{d}p \tag{8.42}$$

Since the propagation terms in (8.42) do not contain the propagation coefficient $\gamma_0(p)$, which for the standard case $c_0 > c_1$, implies the possible occurence of head-waves. The corresponding time-domain expressions of each of these constituents follow upon the application of the Cagniard-DeHoop technique given in Appendix B. In this way, the body-wave time-domain constituents can be written as

$$\left\{ E_1^{\mathrm{BW};[n]}, H_2^{\mathrm{BW};[n]} \right\} (x_1, d, t) = [V_0(t)/w] \overset{(t)}{*} \pi^{-1}$$
$$\times \left\{ e_{1\mathrm{b}}^{\mathrm{BW};[n]} - e_{1\mathrm{a}}^{\mathrm{BW};[n]}, h_{2\mathrm{b}}^{\mathrm{BW};[n]} - h_{2\mathrm{a}}^{\mathrm{BW};[n]} \right\} (x_1, d, t) \tag{8.43}$$

with

$$\left\{ e_{1\mathrm{a}}^{\mathrm{BW};[n]}, h_{2\mathrm{a}}^{\mathrm{BW};[n]} \right\} (x_1, d, t)$$
$$= \mathrm{Re}\left(\left\{ \epsilon_1 \gamma_0 \left(p_{\mathrm{a}}^{\mathrm{BW}} \right) / \epsilon_0 p_{\mathrm{a}}^{\mathrm{BW}}, \epsilon_1 / p_{\mathrm{a}}^{\mathrm{BW}} \right\} T_H \left(p_{\mathrm{a}}^{\mathrm{BW}} \right) \left[R_H \left(p_{\mathrm{a}}^{\mathrm{BW}} \right) \right]^n \right)$$
$$\times H \left(t - T_{\mathrm{BWa}}^{[n]} \right) \left(t^2 - T_{\mathrm{BWa}}^{[n]2} \right)^{-1/2} \tag{8.44}$$

in which $p_\mathrm{a}^\mathrm{BW} = p_\mathrm{a}^\mathrm{BW}[X_\mathrm{a}, (2n+1)d, t]$

$$p_\mathrm{a}^\mathrm{BW} = \left\{ X_\mathrm{a}t + \mathrm{i}(2n+1)d \left(t^2 - T_\mathrm{BWa}^{[n]2} \right)^{1/2} \right\} \bigg/ \left\{ X_\mathrm{a}^2 + [(2n+1)d]^2 \right\} \tag{8.45}$$

with

$$T_\mathrm{BWa}^{[n]} = \left\{ X_\mathrm{a}^2 + [(2n+1)d]^2 \right\}^{1/2} / c_1 \tag{8.46}$$

In the range where $X_\mathrm{a,b} / \{ X_\mathrm{a,b}^2 + [(2n+1)d]^2 \}^{1/2} > c_1/c_0$ is satisfied, the head-wave time-domain constituents are present

$$
\begin{aligned}
\left\{ E_1^{\mathrm{HW};[n]}, H_2^{\mathrm{HW};[n]} \right\} (x_1, d, t) &= [V_0(t)/w] \overset{(t)}{*} \pi^{-1} \\
&\times \left\{ e_{1\mathrm{b}}^{\mathrm{HW};[n]} - e_{1\mathrm{a}}^{\mathrm{HW};[n]}, h_{2\mathrm{b}}^{\mathrm{HW};[n]} - h_{2\mathrm{a}}^{\mathrm{HW};[n]} \right\} (x_1, d, t)
\end{aligned}
\tag{8.47}
$$

where

$$
\begin{aligned}
&\left\{ e_{1\mathrm{a}}^{\mathrm{HW};[n]}, h_{2\mathrm{a}}^{\mathrm{HW};[n]} \right\} (x_1, d, t) \\
&= \mathrm{Im} \left[\left\{ \epsilon_1 \gamma_0 \left(p_\mathrm{a}^\mathrm{HW} \right) / \epsilon_0 p_\mathrm{a}^\mathrm{HW}, \epsilon_1 / p_\mathrm{a}^\mathrm{HW} \right\} T_H \left(p_\mathrm{a}^\mathrm{HW} \right) \left[R_H \left(p_\mathrm{a}^\mathrm{HW} \right) \right]^n \right] \\
&\times \Pi \left[\left(t - T_\mathrm{Ca}^{[n]} \right) / T_\mathrm{La}^{[n]} \right] \left(T_\mathrm{BWa}^{[n]2} - t^2 \right)^{-1/2}
\end{aligned}
\tag{8.48}
$$

in which $p_\mathrm{a}^\mathrm{HW} = p_\mathrm{a}^\mathrm{HW}[X_\mathrm{a}, (2n+1)d, t]$

$$p_\mathrm{a}^\mathrm{HW} = \left\{ X_\mathrm{a}t - (2n+1)d \left(T_\mathrm{BWa}^{[n]2} - t^2 \right)^{1/2} \right\} \bigg/ \left\{ X_\mathrm{a}^2 + [(2n+1)d]^2 \right\} \tag{8.49}$$

with

$$T_\mathrm{HWa}^{[n]} = X_\mathrm{a}/c_0 + (2n+1)d \left(1/c_1^2 - 1/c_0^2 \right)^{1/2} \tag{8.50}$$

$$T_\mathrm{Ca}^{[n]} = \left(T_\mathrm{HWa}^{[n]} + T_\mathrm{BWa}^{[n]} \right) / 2 \tag{8.51}$$

$$T_\mathrm{La}^{[n]} = T_\mathrm{BWa}^{[n]} - T_\mathrm{HWa}^{[n]} \tag{8.52}$$

In addition, if the observer is above the slot, i.e. if $|x_1| \leq w/2$, then the plane-wave has to be included

$$\left\{ E_1^{\mathrm{PW};[n]}, H_2^{\mathrm{PW};[n]} \right\} (x_1, d, t) = T_H(0)[R_H(0)]^n \{ \eta_1/\eta_0, \eta_1 \} V_0[t - (2n+1)d/c_1] \Pi(x_1/w)/w \tag{8.53}$$

71

8.6 The time-domain field in the vacuum half-space

In this section we focus on the time-domain constituents of the fields radiated into the vacuum half-space $\mathcal{D}_0$. Using the results of Section 8.3 we express them as

$$
\left\{ \hat{E}_1^{[n]}, \hat{E}_3^{[n]}, \hat{H}_2^{[n]} \right\} (x_1, x_3, s)
$$
$$
= \frac{\hat{V}_0(s)}{w} \frac{1}{2\pi\mathrm{i}} \int_{p=-\mathrm{i}\infty}^{\mathrm{i}\infty} \left\{ \frac{\epsilon_1 \gamma_0(p)}{\epsilon_0 p \gamma_1(p)}, -\frac{\epsilon_1}{\epsilon_0 \gamma_1(p)}, \frac{\epsilon_1}{p \gamma_1(p)} \right\} T_H(p)[R_H(p)]^n
$$
$$
\times \Big(\exp\{-s[pX_{\mathrm{b}} + \gamma_0(p)(x_3 - d) + \gamma_1(p)(2n+1)d]\}
$$
$$
- \exp\{-s[pX_{\mathrm{a}} + \gamma_0(p)(x_3 - d) + \gamma_1(p)(2n+1)d]\} \Big) \mathrm{d}p \tag{8.54}
$$

The propagation terms as well as the algebraic part of integrands now contain both propagation coefficients $\gamma_0(p)$ and $\gamma_1(p)$. This has the consequence that the body-wave part of the Cagniard-DeHoop contour intersects the real p-axis in between $p = 0$ and $p = 1/c_0$, implying the absence of head-wave constituents in $\mathcal{D}_0$. Note that, in this case, the Cagniard-DeHoop contour does not have a simple parametrization and has to be determined either algebraically via Cardano's formula or via the iterative numerical procedure as described in Appendix D. Once the iterative procedure is terminated, the corresponding time-domain body-wave expressions of each of these constituents result from the procedure as applied in Sections 8.4 and 8.5, i.e.

$$
\left\{ E_1^{\mathrm{BW};[n]}, E_3^{\mathrm{BW};[n]}, H_2^{\mathrm{BW};[n]} \right\} (x_1, x_3, t) = [V_0(t)/w] \overset{(t)}{*} \pi^{-1}
$$
$$
\times \left\{ e_{1\mathrm{b}}^{\mathrm{BW};[n]} - e_{1\mathrm{a}}^{\mathrm{BW};[n]}, e_{3\mathrm{b}}^{\mathrm{BW};[n]} - e_{3\mathrm{a}}^{\mathrm{BW};[n]}, h_{2\mathrm{b}}^{\mathrm{BW};[n]} - h_{2\mathrm{a}}^{\mathrm{BW};[n]} \right\} (x_1, x_3, t) \tag{8.55}
$$

with

$$
\left\{ e_{1\mathrm{a}}^{\mathrm{BW};[n]}, e_{3\mathrm{a}}^{\mathrm{BW};[n]}, h_{2\mathrm{a}}^{\mathrm{BW};[n]} \right\} (x_1, x_3, t)
$$
$$
= \mathrm{Im} \Big[\left[\epsilon_1 / \gamma_1 \left(p_{\mathrm{a}}^{\mathrm{BW}} \right) \right] \left\{ \gamma_0 \left(p_{\mathrm{a}}^{\mathrm{BW}} \right) / \epsilon_0 p_{\mathrm{a}}^{\mathrm{BW}}, -1/\epsilon_0, 1/p_{\mathrm{a}}^{\mathrm{BW}} \right\}
$$
$$
\times T_H \left(p_{\mathrm{a}}^{\mathrm{BW}} \right) \left[R_H \left(p_{\mathrm{a}}^{\mathrm{BW}} \right) \right]^n \partial_t p_{\mathrm{a}}^{\mathrm{BW}} \Big] \tag{8.56}
$$

where $p_{\mathrm{a,b}}^{\mathrm{BW}}(\tau)$ result from solving $\tau = pX_{\mathrm{a,b}} + \gamma_0(p)(x_3 - d) + \gamma_1(p)(2n+1)d$ such that $\tau \in \mathbb{R}$, $\tau > 0$. The examples of corresponding Cagniard-DeHoop contours are given in Sec. 8.7.3.

In addition, if $|x_1| \leq w/2$ the plane-wave time-domain constituents are present

$$
\left\{ E_1^{\mathrm{PW};[n]}, E_3^{\mathrm{PW};[n]}, H_2^{\mathrm{PW};[n]} \right\} (x_1, x_3, t) = T_H(0)[R_H(0)]^n \{\eta_1/\eta_0, 0, \eta_1\}
$$
$$
\times V_0[t - (x_3 - d)/c_0 - (2n+1)d/c_1]\Pi(x_1/w)/w \tag{8.57}
$$

8.7 Illustrative numerical examples

This section provides illustrative numerical results for the case of excitation with the power exponential pulse with parameter $\nu = 2$ ($t_w/t_r = 1.8473$), shown in Fig. 5.2a. (Fig. 5.2b

shows its spectral diagram). This activating pulse is used throughout this section. The properties of the slab are taken as $\{\epsilon_1, \mu_1\} = \{4\epsilon_0, \mu_0\}$.

The first part of this section shows pulse shapes of $\{E_1, H_2\}(x_1, d, t)$ at the level of vacuum/dielectric interface, while the second part provides pulse shapes of $E_3(x_1, x_3, t)$ just below and above the interface, across which it jumps. The third subsection gives the time evolution of the Poynting vector within a certain region of space at successive observation times. The last part is supplemented by examples of Cagniard-DeHoop contours associated with the evaluation of pulse shapes in the vacuum.

All time convolution integrals contain inverse square-root singularities at one of the end-points of the integrals. These are numerically handled via a stretching of the variable of integration according to

$$\tau = T_{\text{BWa}}^{[n]} \cosh(u) \quad \text{for } 0 < u < \infty \tag{8.58}$$

with the Jacobian

$$\frac{\partial \tau}{\partial u} = T_{\text{BWa}}^{[n]} \sinh(u) = \left(\tau^2 - T_{\text{BWa}}^{[n]2}\right)^{1/2} \tag{8.59}$$

for a body-wave constituent with arrival time $T_{\text{BWa}}^{[n]}$ and

$$\tau = T_{\text{BWa}}^{[n]} \cos(v) \quad \text{for } 0 < v < \pi/2 \tag{8.60}$$

with the Jacobian

$$\frac{\partial \tau}{\partial v} = -T_{\text{BWa}}^{[n]} \sin(v) = -\left(T_{\text{BWa}}^{[n]2} - \tau^2\right)^{1/2} \tag{8.61}$$

for a head-wave constituent. The integration limits at the time convolution integrals are subsequently adjusted to the corresponding intervals in u and v.

8.7.1 Examples of pulse shapes at the vacuum/dielectric interface

In any finite time window of observation, only a finite number of time-domain constituents yields a non-zero contribution, while in the range of critical refraction only a subset of these contributions have a head-wave part. The objective of our analysis is to compare the pulse shapes of the different constituents with the ones that the slot antenna would radiate into a half-space with the properties of $\mathcal{D}_0$. The latter can be found in Section 6.4. The comparison is carried out on the vacuum/dielectric interface.

Four positions of observation at $x_3 = d$ have been selected: (A) $x_1/d = 0$, (B) $x_1/d = 1$, (C) $x_1/d = 3$, (D) $x_1/d = 5$ (indicated, not to scale, in Fig. 8.1). The observation point (A) lies right in front of the radiating slot. The observation point (B) is within the range of critical refraction associated with the left edge of the slot and outside the range of critical refraction associated with the right edge of the slot, while the observation points (C) and (D) are within the range of critical refraction associated with both edges of the slot. The time window of observation is taken as $0 < c_0 t/d < 20$. The width of the slot w and the thickness of the dielectric slab d are interrelated as $d/w = 1$. The rise time of the excitation pulse t_r is taken as half of the free-space travel time across

Table 8.1: Arrival times of time-domain constituents at the vacuum/dielectric interface.

	A	B	C	D	A	B	C	D
	Arrival times							
order	Head-wave (left edge)				Body-wave (left edge)			
$[n]$	$c_0 T_{\mathrm{HWa}}^{[n]}/d$				$c_0 T_{\mathrm{BWa}}^{[n]}/d$			
0	-	3.2321	5.2321	7.2321	2.2361	3.6056	7.2801	11.1803
1	-	-	8.6962	10.6962	6.0828	6.7082	9.2195	12.5300
2	-	-	12.1603	14.1603	10.0499	10.4403	12.2066	14.8661
3	-	-	-	17.6244	14.0357	14.3178	15.6525	17.8045
4	-	-	-	-	18.0278	18.2483	19.3132	-
order	Head-wave (right edge)				Body-wave (right edge)			
$[n]$	$c_0 T_{\mathrm{HWb}}^{[n]}/d$				$c_0 T_{\mathrm{BWb}}^{[n]}/d$			
0	-	-	4.2321	6.2321	2.2361	2.2361	5.3852	9.2195
1	-	-	7.6962	9.6962	6.0828	6.0828	7.8102	10.8167
2	-	-	-	13.1603	10.0499	10.0499	11.1803	13.4536
3	-	-	-	16.6244	14.0357	14.0357	14.8661	16.6433
4	-	-	-	-	18.0278	18.0278	18.6815	-

the slab. As described in Appendix E, the pulse time width t_w is related to the pulse rise time t_r via (E.3), which gives $c_0 t_w/d = 0.9236$ for $\nu = 2$. The arrival times of the different contributions are collected in Table 8.1. Figures 8.2 – 8.5 show the results. In them, the normalized time is $c_0 t/d$, the normalized electric field is $E_1 w/V_{\max}$ while the normalized magnetic field is $(\mu_0/\epsilon_0)^{1/2} H_2 w/V_{\max}$. The observation point (A) lies outside the range of critical refraction range of both radiating edges. Here, the wave motion consists of a superposition of a plane-wave contribution emanating from the radiating slot and cylindrical waves emanating from the edges of the slot. No head-wave contribution occurs. The observation point (B) lies within the range of critical refraction of the left edge of the slot and outside the one associated with the right edge. Here, the wave motion consists of a superposition of cylindrical waves emanating from both edges of the slot and head-wave contributions emanating form the right edge of the slot. The observation points (C) and (D) lie within the range of critical refraction of both edges of the slot. Here, the wave motion consists of a superposition of cylindrical waves emanating from both edges of the slot and head-wave contributions emanating form both edges of the slot. In all those regions where head-wave contributions occur pulse shapes show up that drastically differ from the excitation.

8.7.2 Examples of pulse shapes just below and above the vacuum/dielectric interface

For the observation of pulse shapes of the electric field component $E_3(x_1, x_3, t)$, six observation points below and above the points (B), (C) and (D) at vertical levels $x_3/d = 0.995, 1.005$ have been chosen. The corresponding points just below the interface are

labeled with ↑ and the points just above the interface with ↓.

In the plots, the normalized time is c_0t/d and the normalized E_3 stands for $E_3 w/V_{\max}$. Figures 8.6 – 8.8 exhibit the jump in magnitude that is related to the electric contrast ratio $\epsilon_1/\epsilon_0 = 4$. The arrival times corresponding to the pulse shapes in the dielectric layer and in the vacuum are summarized in Tables 5.2 and 5.3, respectively.

8.7.3   Time evolution of the Poynting vector

The (color) vector density plots Figs. 8.9 – 8.12 show the time snaps of the two-component Poynting vector

$$S_1 = -E_3H_2 \tag{8.62}$$
$$S_3 = E_1H_2 \tag{8.63}$$

normalized with respect to

$$|\boldsymbol{S}|_{\mathrm{ref}} = (V_{\max}/w)^2(\epsilon_0/\mu_0)^{1/2} \tag{8.64}$$

The reference magnitude $|\boldsymbol{S}|_{\mathrm{ref}}$ corresponds to the maximum value of the Poynting vector as it would be carried by a TEM-mode in a parallel-plate waveguide that would be a feeding of the radiating aperture. The spatial domain of observation is taken as $\{-3 \le x_1/d \le 3, 0 \le x_3/d \le 3\}$ and two observation times are chosen as $c_0t/d = \{2, 4\}$. The width of the slot w and the thickness of the dielectric slab d are interrelated via $d/w = 1$.

Figure 8.9 shows the time evolution of the Poynting vector for the power-exponential pulse excitation with $c_0t_w/d = 0.9236$. In Fig. 8.9(a) the wavefront just reaches the dielectric/vacuum interface. Because of the relatively high ratio of the spatial extent of the excitation pulse compared with the slot width, the radiation of the slot resembles the one that would be radiated from a line source. In Fig. 8.9(b), the reflected wave constituents as well as head-wave constituent are clearly seen.

In order to illustrate the dependence on the relation between the spatial extent of the excitation pulse and the slot width, the rise time t_r of the excitation pulse has been decreased to one tenth of the free-space travel time across the slab. The corresponding normalized pulse time width is $c_0t_w/d = 0.1847$. For this case, Fig. 8.10 shows the Poynting vector distribution at the two observation times $c_0t/d = 2$ and $c_0t/d = 4$. Overlapping cylindrical waves arising from the radiating edges and a plane-wave contribution emanating from the slot are clearly distinguishable. The electromagnetic power density radiated from the slot is now concentrated within the narrower beam propagating above the radiating slot.

For a closer look, Figures 8.11 and 8.12 show the time evolution of the Poynting vector in the observation domain $\{-1.1 \le x_1/d \le 1.1, 0 \le x_3/d \le 0.6\}$ at two observation times (a) $c_0t/d = 0.55$, (b) $c_0t/d = 1.21$ for both foregoing normalized pulse time widths $c_0t_w/d = \{0.1847, 0.9236\}$. While in Figures 8.11 the cylindrical waves are hardly identifiable, the Figures 8.12 clearly show the cylindrical waves emanating at radiating edges before and after they overlap themselves.

At two points inside the spatial observation region, the Cagniard-DeHoop paths have been evaluted for the first two successive time-domain constituents $n = \{0, 1\}$. The

Table 8.2: Arrival times of constituents in the dielectric slab.

Arrival times						
	Head-wave (upgoing, left edge)			Body-wave (upgoing, left edge)		
order	$c_0 T_{\text{HWa}+}^{[n]}/d$			$c_0 T_{\text{BWa}+}^{[n]}/d$		
$[n]$	↑B	↑C	↑D	↑B	↑C	↑D
0	3.2234	5.2234	7.2234	3.6000	2.774	11.1786
1	-	8.6875	10.6875	6.6993	9.2130	12.5252
2	-	12.1516	14.1516	10.4307	12.1984	14.8593
3	-	-	17.6157	14.3080	15.6435	17.7966
4	-	-	-	18.2384	19.3039	-
	Head-wave (downgoing, left edge)			Body-wave (downgoing, left edge)		
order	$c_0 T_{\text{HWa}-}^{[n]}/d$			$c_0 T_{\text{BWa}-}^{[n]}/d$		
$[n]$	↑B	↑C	↑D	↑B	↑C	↑D
0	3.2407	5.2407	7.2407	3.6111	7.2829	11.1821
1	-	8.7048	10.7048	6.7171	9.2261	12.5348
2	-	12.1689	14.1689	10.4499	12.2147	14.8728
3	-	-	17.6330	14.3276	15.6614	17.8124
4	-	-	-	18.2582	19.3225	-
	Head-wave (upgoing, right edge)			Body-wave (upgoing, right edge)		
order	$c_0 T_{\text{HWb}+}^{[n]}/d$			$c_0 T_{\text{BWb}+}^{[n]}/d$		
$[n]$	↑B	↑C	↑D	↑B	↑C	↑D
0	-	4.2234	6.2234	2.2271	5.3815	9.2174
1	-	7.6875	9.6875	6.0729	7.8026	10.8111
2	-	-	13.1516	10.0399	11.1714	13.4462
3	-	-	16.6157	14.0257	14.8567	16.6349
4	-	-	-	18.0178	18.6719	-
	Head-wave (downgoing, right edge)			Body-wave (downgoing, right edge)		
order	$c_0 T_{\text{HWb}-}^{[n]}/d$			$c_0 T_{\text{BWb}-}^{[n]}/d$		
$[n]$	↑B	↑C	↑D	↑B	↑C	↑D
0	-	4.2407	6.2407	2.2450	5.3889	9.2217
1	-	7.7048	9.7048	6.0926	7.8179	10.8222
2	-	-	13.1689	10.0598	11.1893	13.4611
3	-	-	16.6330	14.0456	14.8755	16.6517
4	-	-	-	18.0377	18.6912	-

Table 8.3: Arrival times of constituents in the vacuum.

order [n]	Arrival times					
	Body-wave (left edge) $c_0 T_{\mathrm{BWa}}^{[n]}/d$			Body-wave (right edge) $c_0 T_{\mathrm{BWb}}^{[n]}/d$		
	↓B	↓C	↓D	↓B	↓C	↓D
0	3.2321	5.2321	7.2321	2.2384	4.2321	6.2321
1	6.7105	8.6962	10.6962	6.0875	7.6962	9.6962
2	10.4444	12.1603	14.1603	10.0548	11.1826	13.1603
3	14.3224	15.6547	17.6244	14.0406	14.8698	16.6244
4	18.2530	19.3167	-	18.0327	18.6858	-

time-window has been taken as $T_{\mathrm{BW}} \leq c_0 t/d \leq 20$. Fig. 8.13 shows the first quadrants of $p_{\mathrm{a,b}}$-planes with the corresponding Cagniard-DeHoop paths at $x_1 = d$, $x_3 = 2d$ while Fig. 8.14 shows the Cagniard-DeHoop paths for the observation point at $x_1 = 3d$, $x_3 = 2d$.

Our analysis can be used to further study the possibilities of adapting the excitation pulse to design requirements associated with optimum signal transfer [34] and/or time-domain beam shaping of antenna arrays.
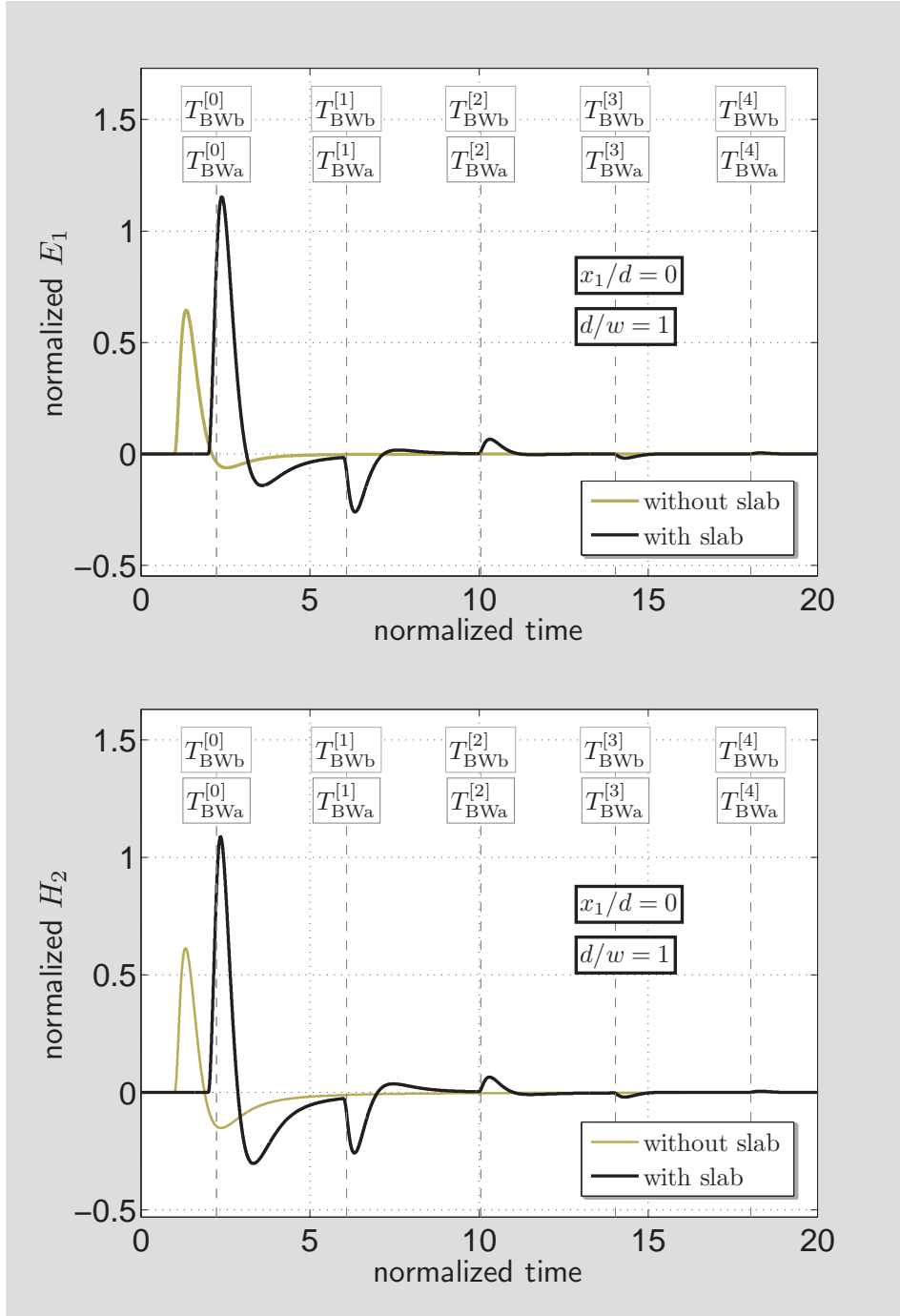
Figure 8.2: Normalized E_1 field time-domain response and normalized H_2 field time-domain response at $x_1/d = 0$.
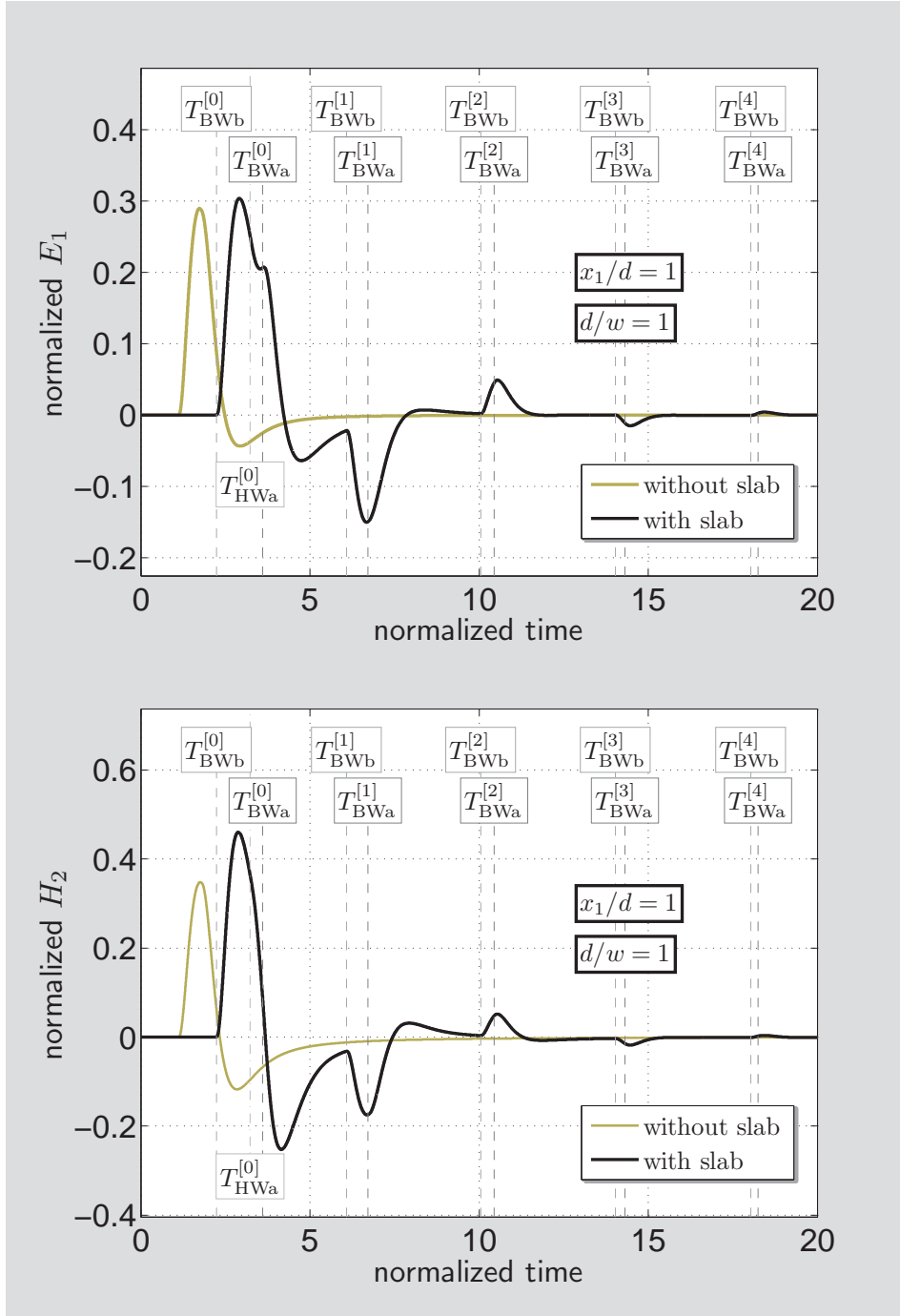
Figure 8.3: Normalized E_1 field time-domain response and normalized H_2 field time-domain response at $x_1/d = 1$.
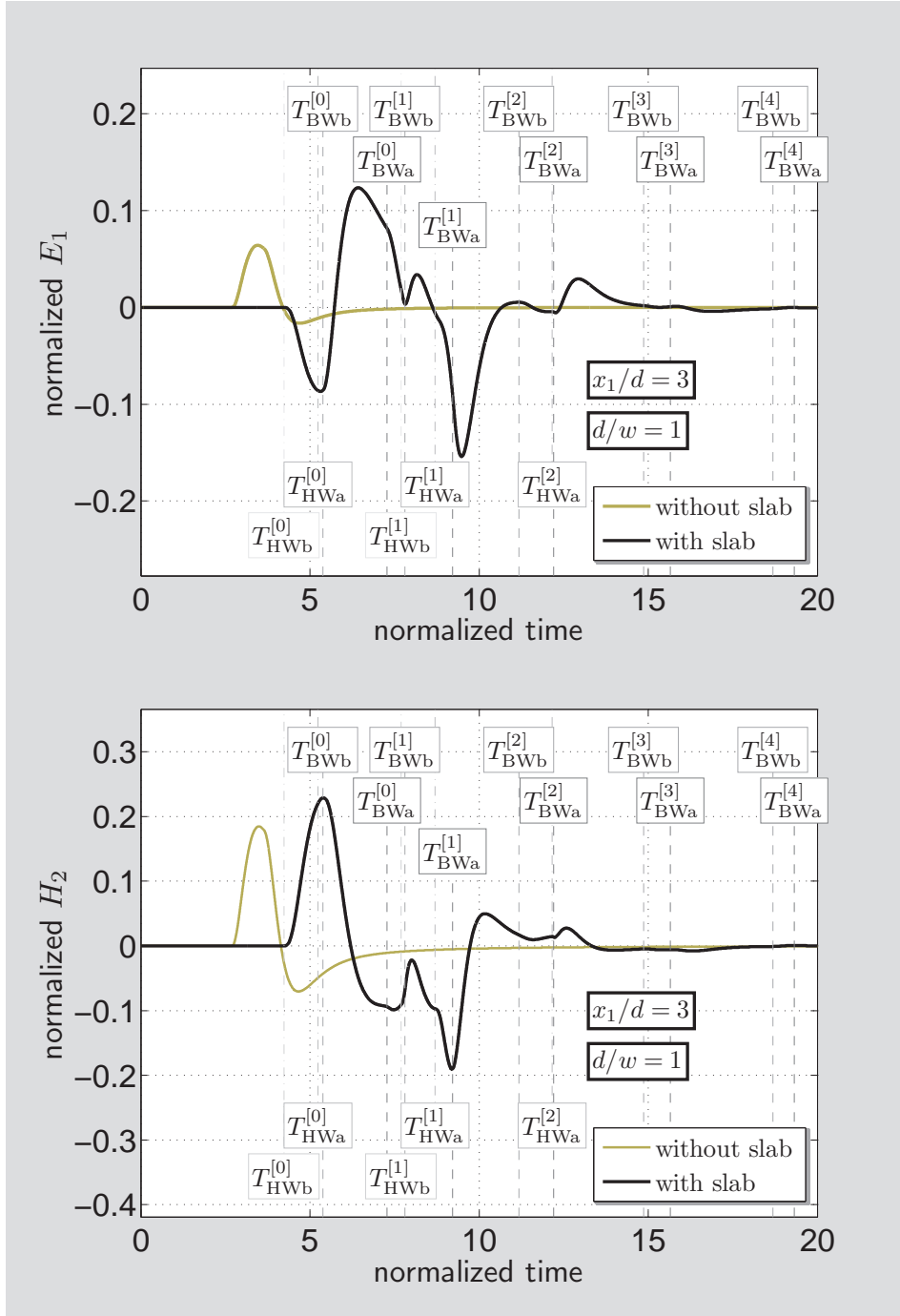
Figure 8.4: Normalized E_1 field time-domain response and normalized H_2 field time-domain response at $x_1/d = 3$.
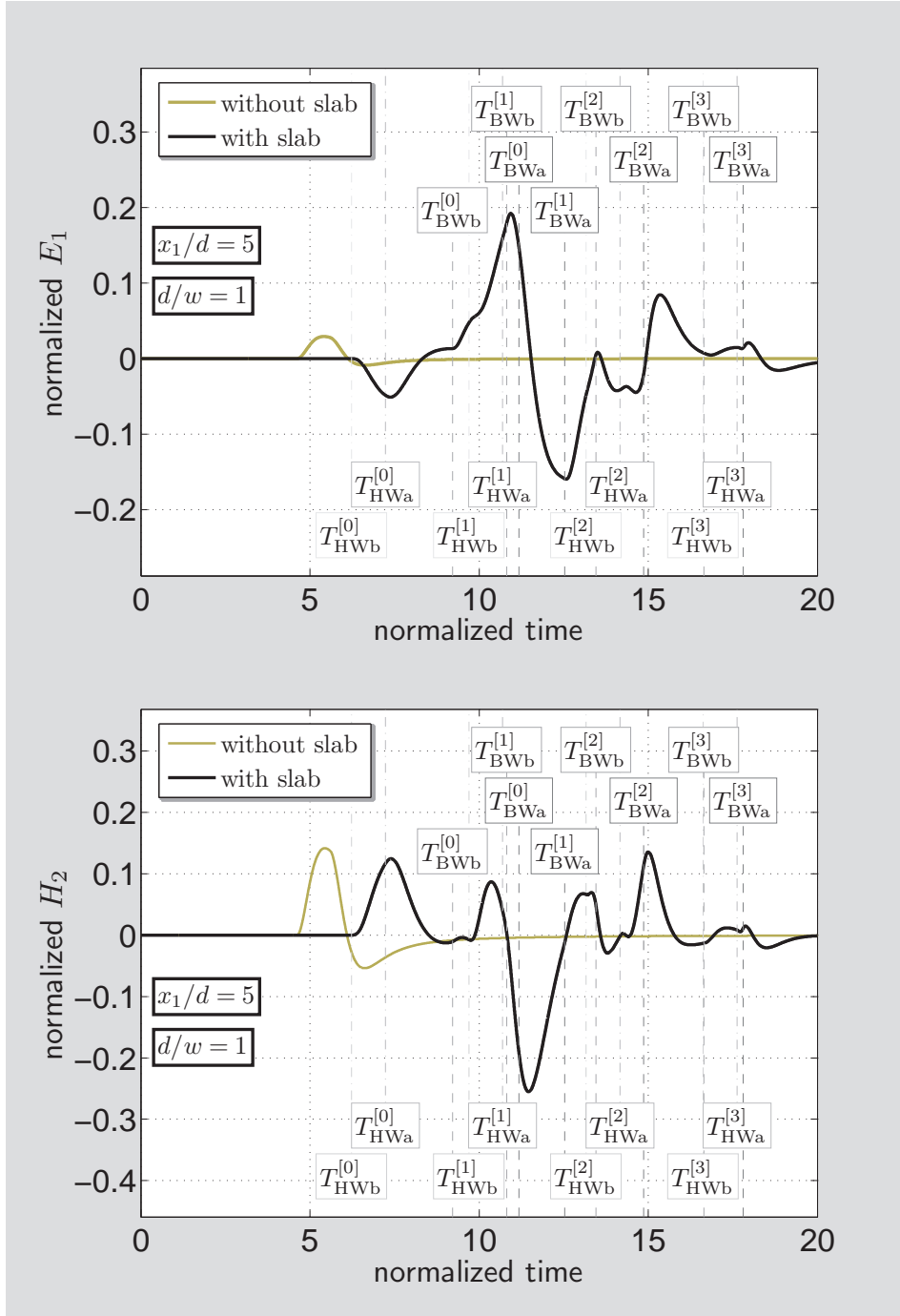
Figure 8.5: Normalized E_1 field time-domain response and normalized H_2 field time-domain response at $x_1/d = 5$.

81
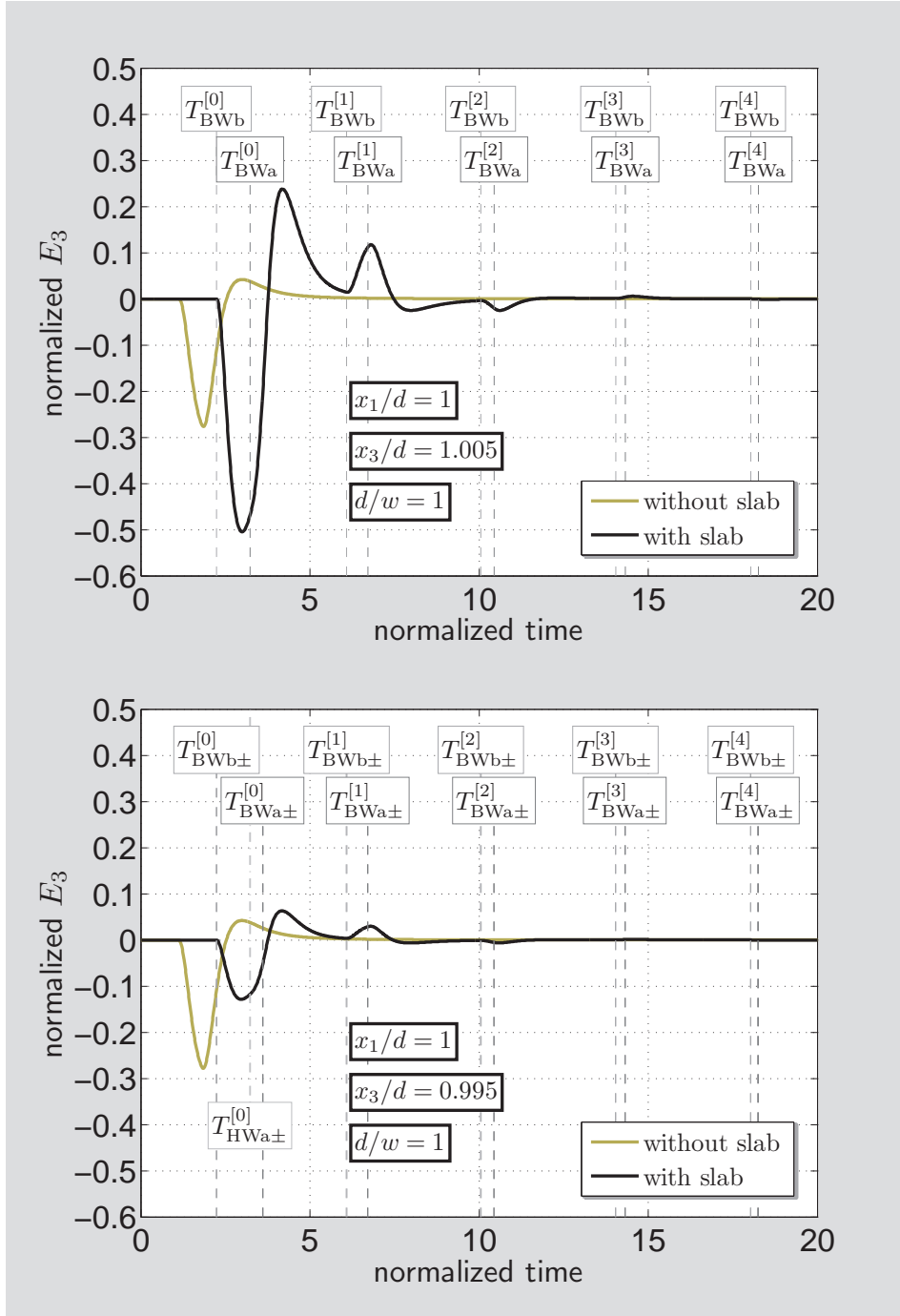
Figure 8.6: Normalized E_3 field time-domain response above ($x_3/d = 1.005$) and below ($x_3/d = 0.995$) the dielectric interface at $x_1/d = 1.0$.
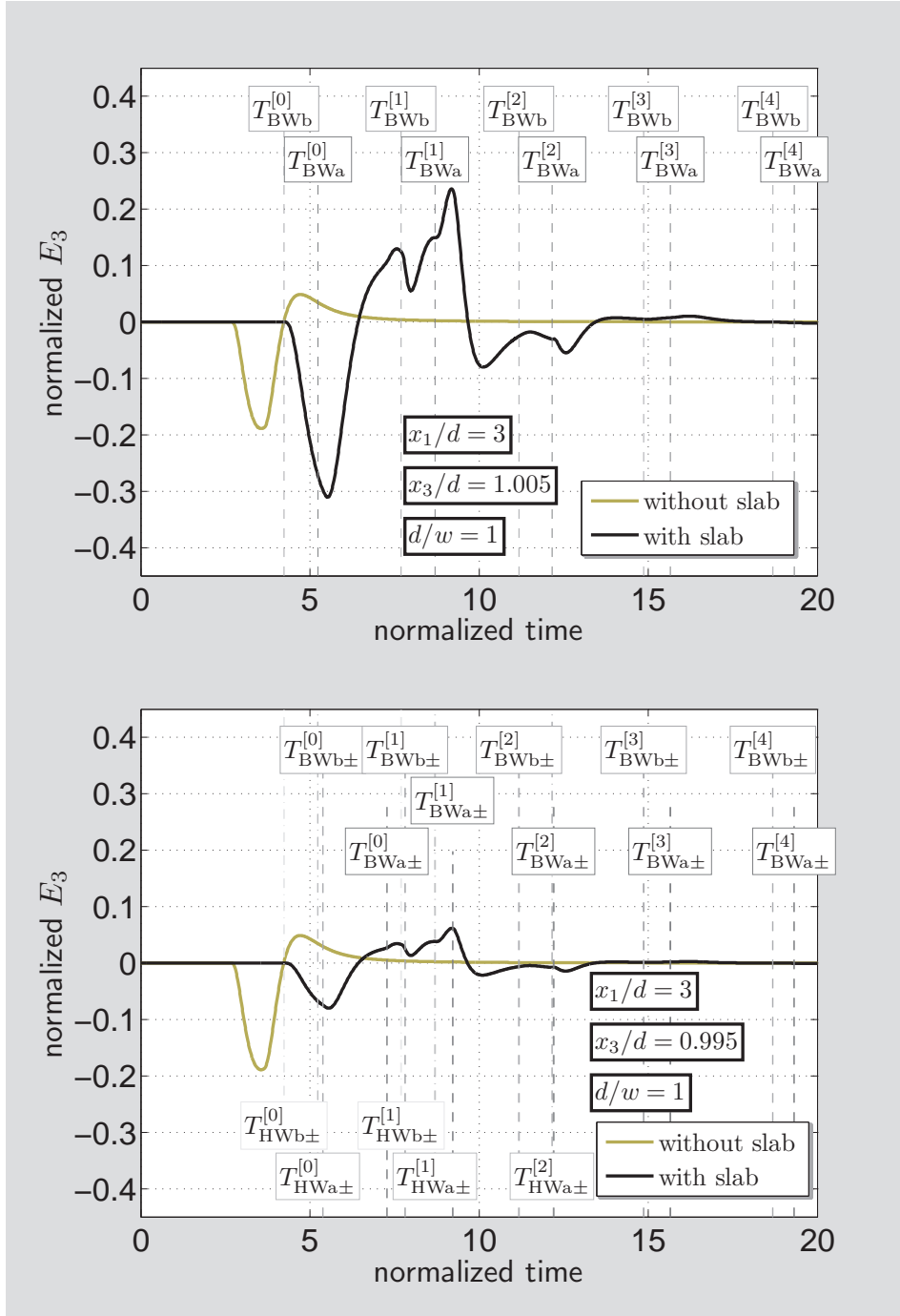
Figure 8.7: Normalized E_3 field time-domain response above ($x_3/d = 1.005$) and below ($x_3/d = 0.995$) the dielectric interface at $x_1/d = 3.0$.
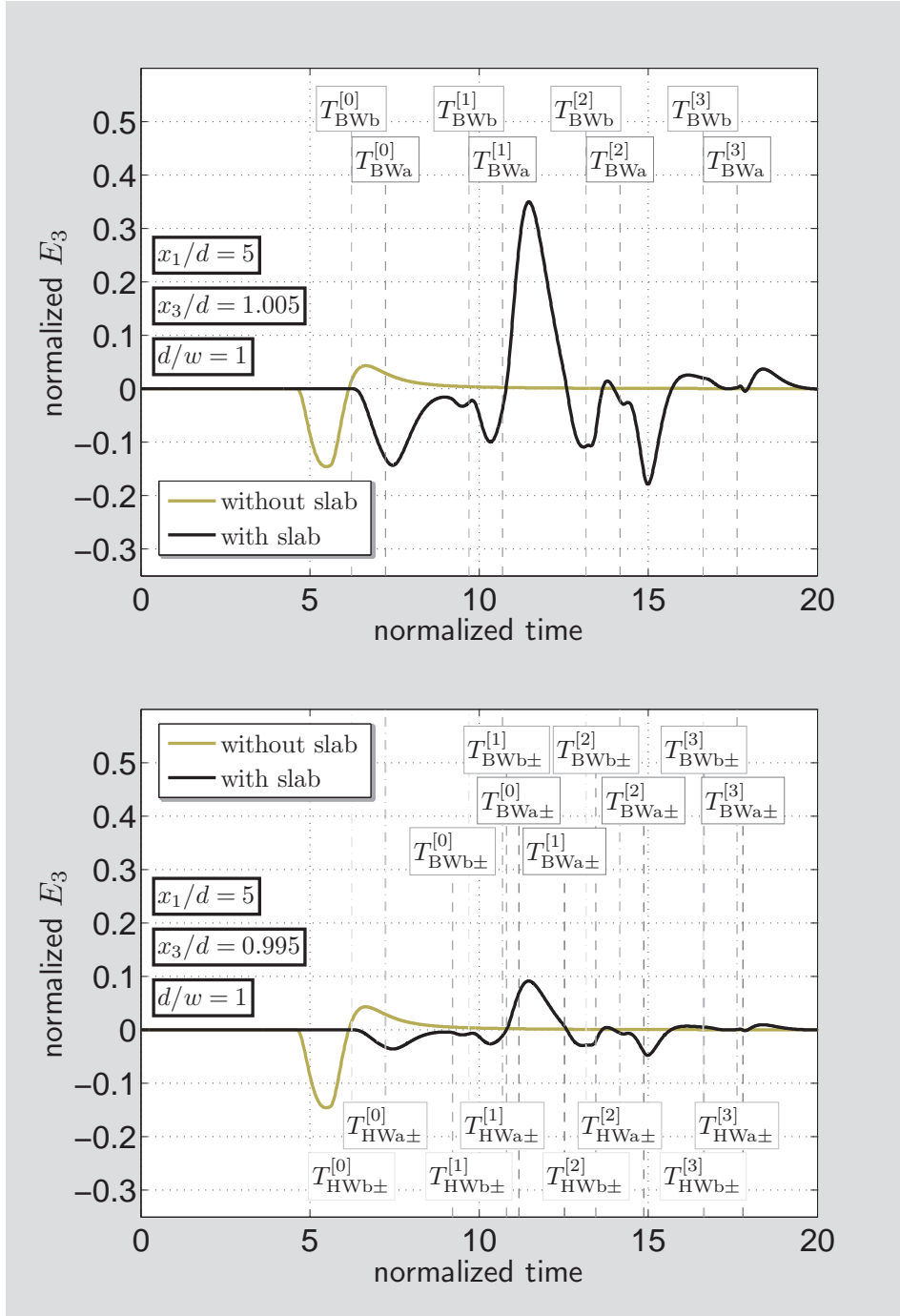
Figure 8.8: Normalized E_3 field time-domain response above $(x_3/d = 1.005)$ and below $(x_3/d = 0.995)$ the dielectric interface at $x_1/d = 5.0$.
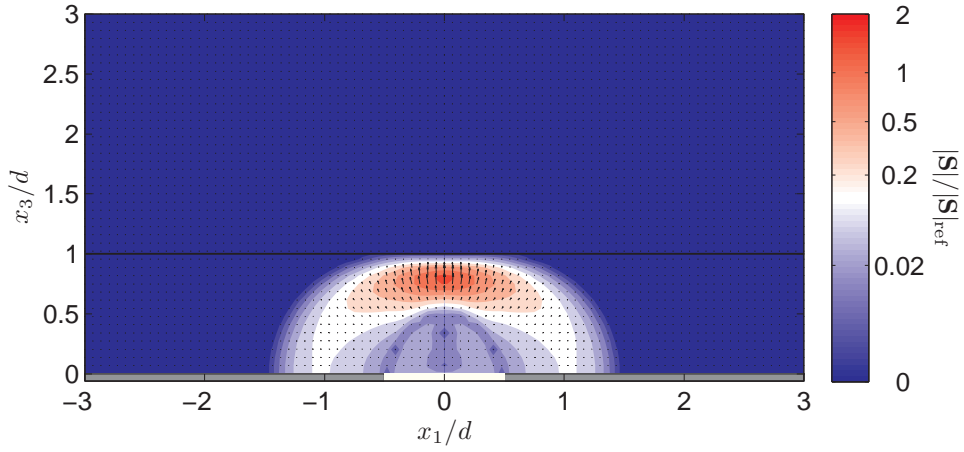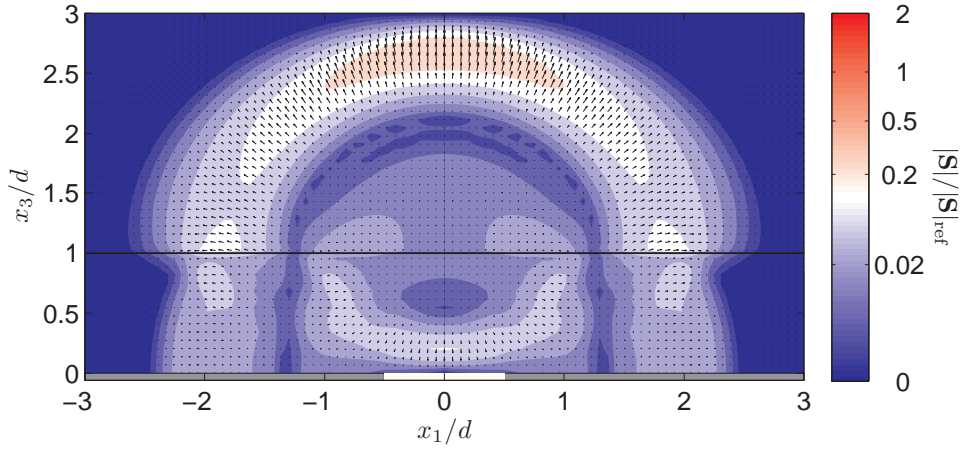
Figure 8.9: Normalized Poynting vector of the EM field at (a) $c_0 t/d = 2$; (b) $c_0 t/d = 4$. Slab thickness versus slot width is $d/w = 1$ and electromagnetic parameters of the dielectric slab are $\{\epsilon_1, \mu_1\} = \{4\epsilon_0, \mu_0\}$. Parameters of the excitation pulse are $c_0 t_w/d = 0.9236$, $\nu = 2$.
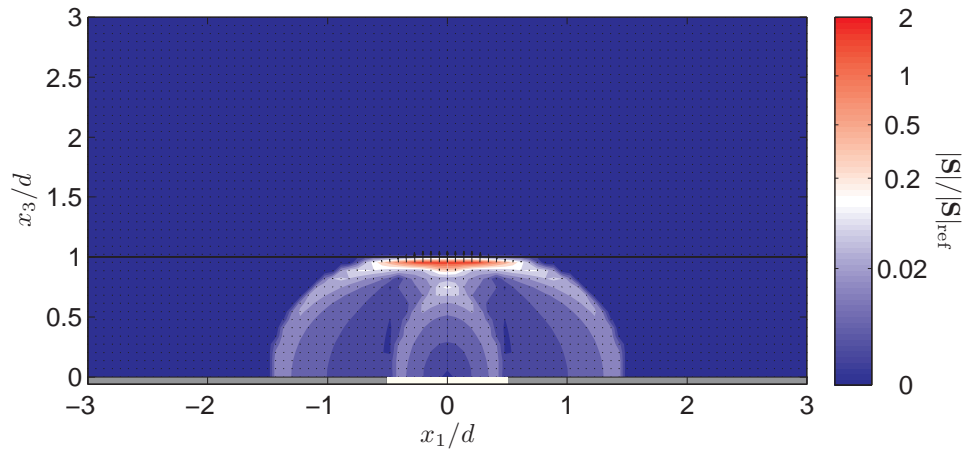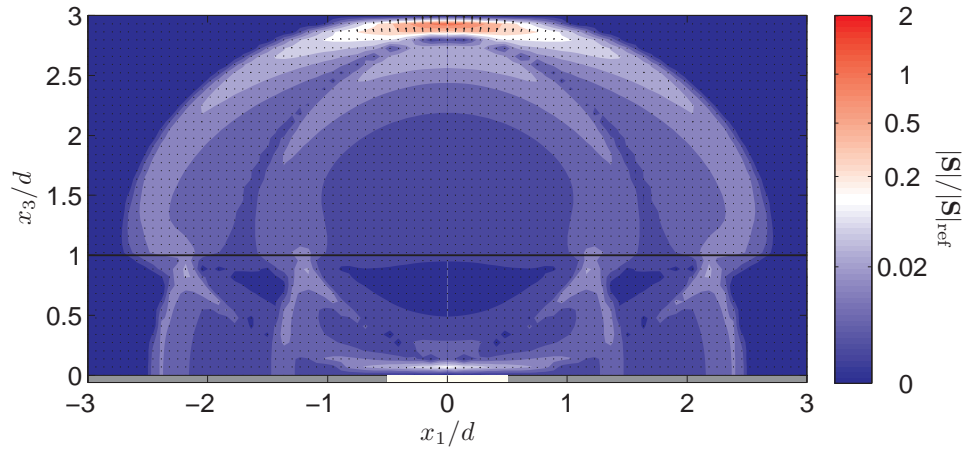
Figure 8.10: Normalized Poynting vector of the EM field at (a) $c_0 t/d = 2$; (b) $c_0 t/d = 4$. Slab thickness versus slot width is $d/w = 1$ and electromagnetic parameters of the dielectric slab are $\{\epsilon_1, \mu_1\} = \{4\epsilon_0, \mu_0\}$. Parameters of the excitation pulse are $c_0 t_w/d = 0.1847$, $\nu = 2$.
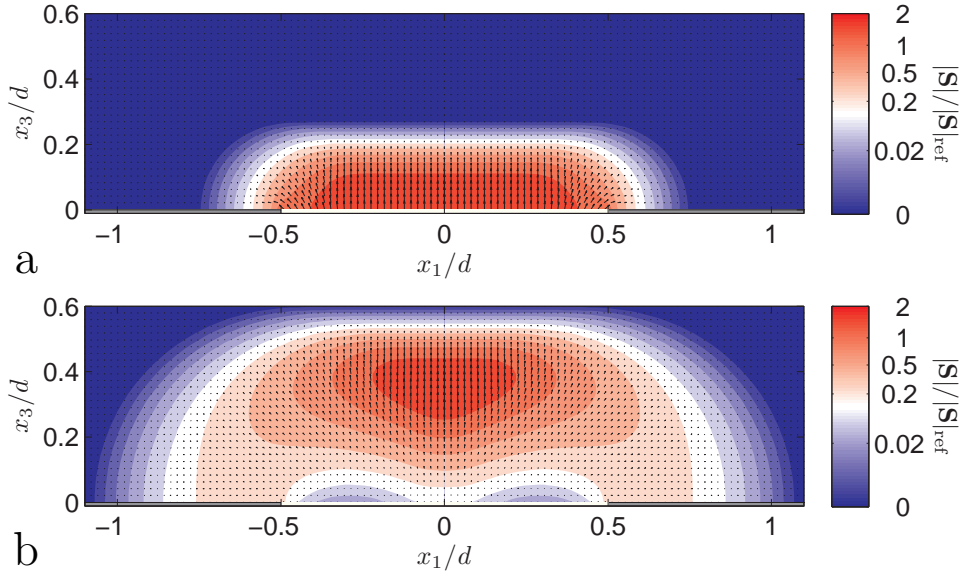
Figure 8.11: Normalized Poynting vector of the EM field at (a) $c_0 t/d = 0.55$; (b) $c_0 t/d = 1.21$. Slab thickness versus slot width is $d/w = 1$ and electromagnetic parameters of the dielectric slab are $\{\epsilon_1, \mu_1\} = \{4\epsilon_0, \mu_0\}$. Parameters of the excitation pulse are $c_0 t_w/d = 0.9236$, $\nu = 2$.
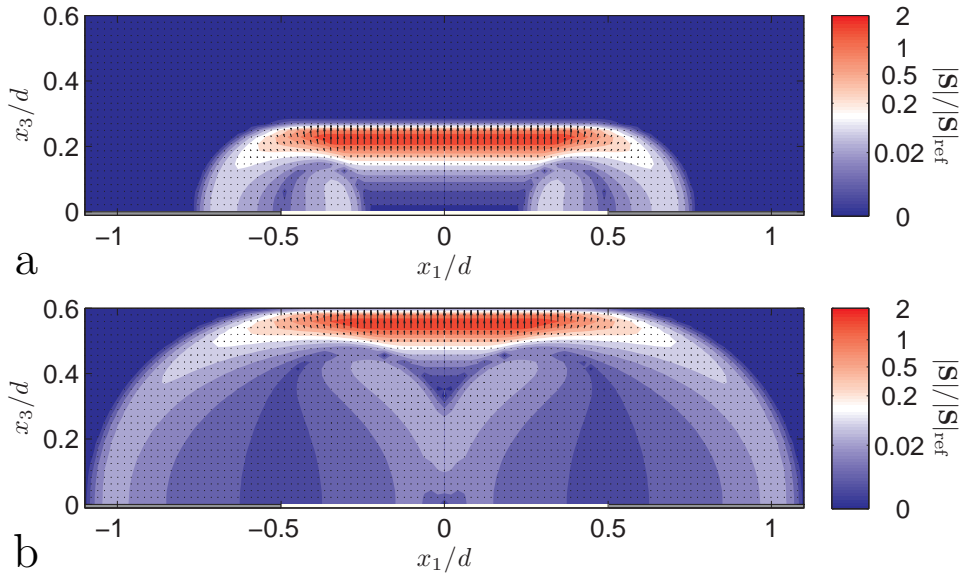
Figure 8.12: Normalized Poynting vector of the EM field at (a) $c_0 t/d = 0.55$; (b) $c_0 t/d = 1.21$. Slab thickness versus slot width is $d/w = 1$ and electromagnetic parameters of the dielectric slab are $\{\epsilon_1, \mu_1\} = \{4\epsilon_0, \mu_0\}$. Parameters of the excitation pulse are $c_0 t_w/d = 0.1847$, $\nu = 2$.
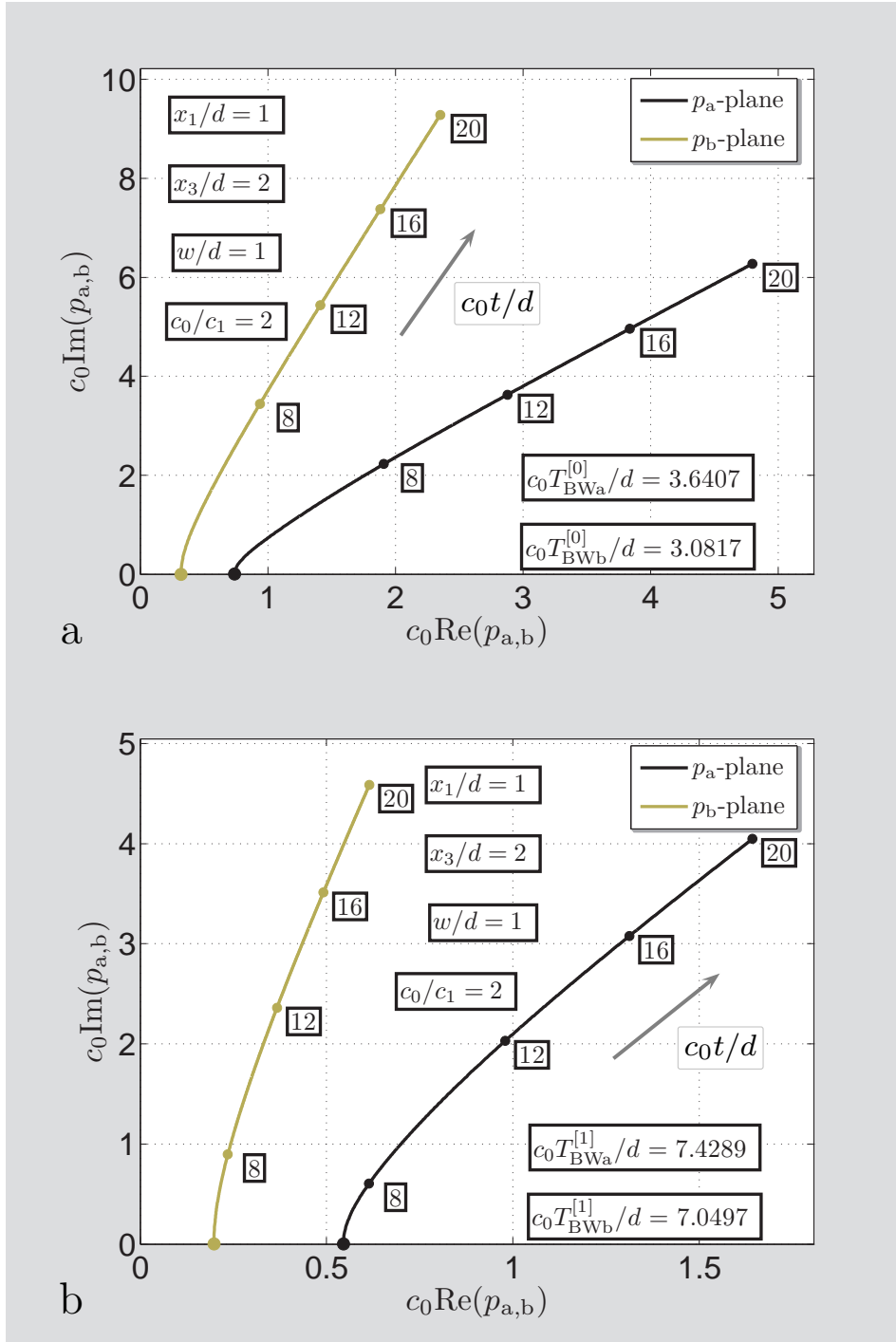
Figure 8.13: Examples of Cagniard-DeHoop contours associated with the first two successive time-domain constituents in vacuum (a) $n = 0$; (b) $n = 1$.
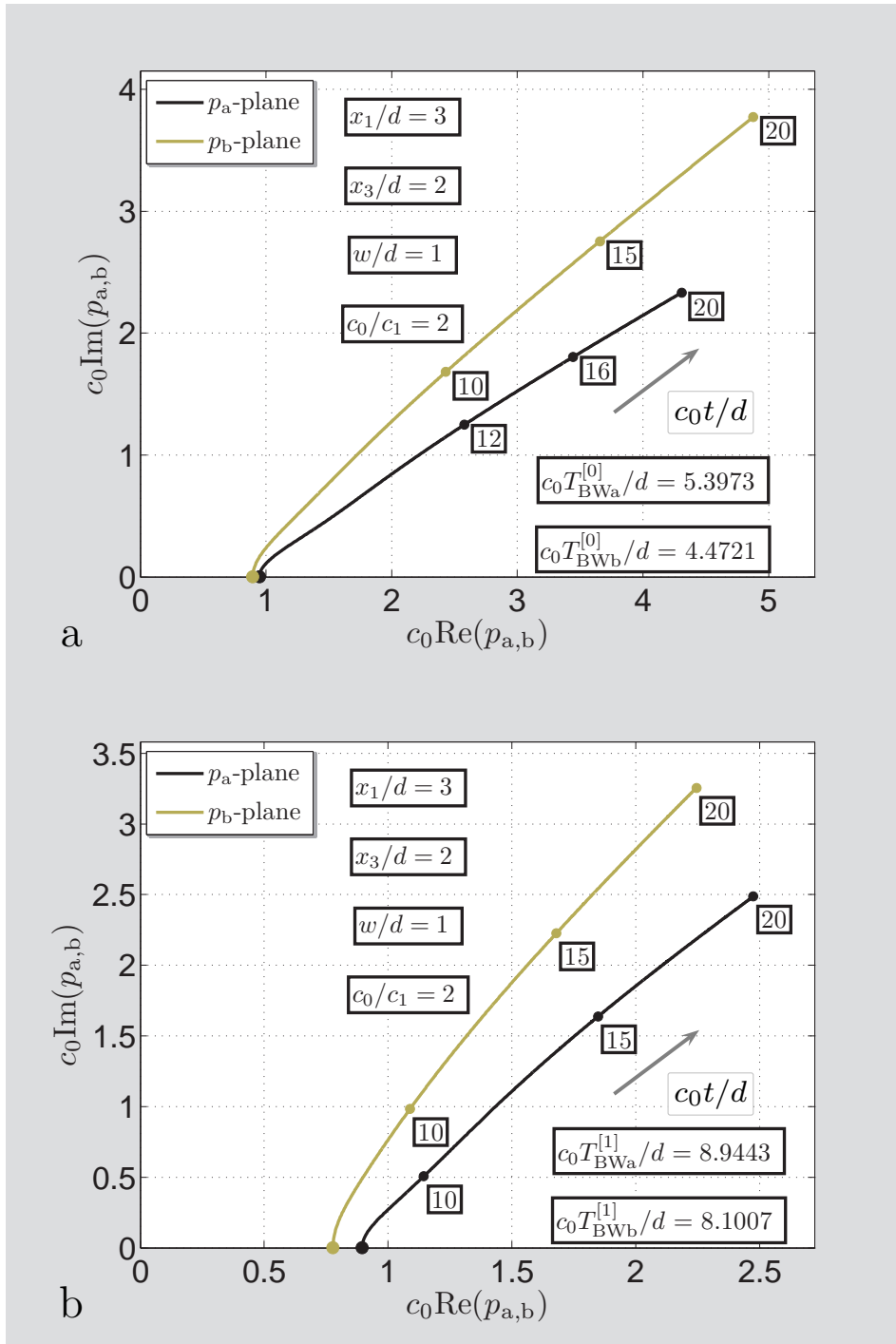
Figure 8.14: Examples of Cagniard-DeHoop contours associated with the first two successive time-domain constituents in vacuum (a) $n = 0$; (b) $n = 1$.

Chapter 9

Pulsed electromagnetic field radiation from a wide slot antenna with a modal excitation

Summary

In this chapter, a pulsed electromagnetic field radiation from an aperture of two-dimensional parallel-plate waveguide that supports the TM (Transverse Magnetic) propagation mode is investigated. As a main tool for the analysis, the Cagniard-DeHoop technique is employed. In conclusion, a number of numerical examples are given.

9.1   Introduction

So far, a pulsed electromagnetic field radiation from two-dimensional slot antennas with a uniform aperture distribution has been considered. The results of previous chapters correspond to the electromagnetic field radiation from a parallel-plate waveguide carrying the TEM (Transverse ElectroMagnetic) mode. In this chapter, an analysis of pulsed radiation from a parallel-plate waveguide is carried out with a nonuniform excitation field distribution, as is in case of the TM (Transverse Magnetic) mode in the waveguide.

The source excited the structure is modeled as a prescribed and spatially nonuniform distribution of the transverse electric field across the slot of a uniform and finite width. The structure further radiates into free space. Using the combination of a unilateral Laplace transformation with respect to time and the spatial slowness representation of the field components that is known as the Cagniard-DeHoop method [11, 12], closed-form expressions are obtained for the electric and the magnetic field as a function of position and time. From them it is clear that the nonuniform excitation via a wide slot shows additional features in that the corners of the waveguide feed show a separate diffractive behavior with accompanying wavefronts. The approach described in the chapter can be also applied on the more complicated configurations treated in Chapters 7–8.

Provided numerical examples clearly illustrate changes in pulse shapes of excited electromagnetic field components with respect to various excitation field spatial distributions.

9.2 Description of the configuration and formulation of the field problem

The configuration examined is shown in Fig. 9.1. The configuration consists of unbounded perfectly electrically conducting (PEC) screen $\mathcal{S} = \{(-\infty < x_1 < -w/2) \cup (w/2 < x_1 < \infty), -\infty < x_2 < \infty, x_3 = 0\}$ with a feeding aperture $\mathcal{A} = \{-w/2 < x_1 < w/2, -\infty < x_2 < \infty, x_3 = 0\}$ of the finite width $w > 0$. The structure radiates into the vacuum half-space $\mathcal{D} = \{-\infty < x_1 < \infty, -\infty < x_2 < \infty, 0 < x_3 < h\}$ with scalar electric permittivity and magnetic permeability $\{\epsilon_0, \mu_0\}$ and corresponding electromagnetic wave speed $c_0 = (\epsilon_0 \mu_0)^{-1/2}$.
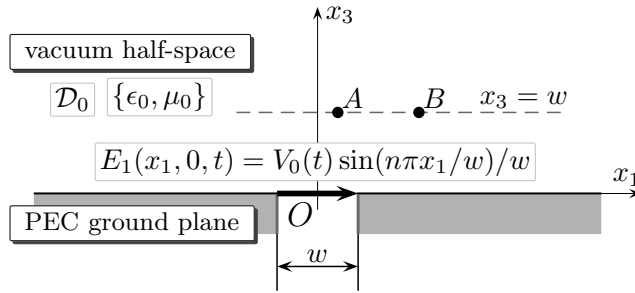
Figure 9.1: Configuration figure with indication of the aperture feeding.

The antenna aperture is fed by the nonuniformly distributed, x_2−independent, electric field that corresponds to the TM modes that would be excited in a parallel-plate waveguide

$$E_1(x_1, 0, t) = V_0(t) \sin(n\pi x_1/w)/w \quad \text{in } \mathcal{A} \tag{9.1}$$

for $n = 1, 3, 5, \ldots$, where $V_0(t)$ is the feeding 'voltage'. Since the excitation, as well as the configuration, are independent of x_2, the non-zero components of the electric field strength $\{E_1, E_3\}(x_1, x_3, t)$ and the magnetic field strength $H_2(x_1, x_3, t)$ satisfy in $\mathcal{D}_0$ the source-free field equations (cf. Eqs. (2.5) − (2.7))

$$\partial_1 H_2 - \epsilon \partial_t E_3 = 0 \tag{9.2}$$
$$\partial_3 H_2 + \epsilon \partial_t E_1 = 0 \tag{9.3}$$
$$\partial_1 E_3 - \partial_3 E_1 - \mu \partial_t H_2 = 0 \tag{9.4}$$

and the excitation condition is (cf. Eq. (2.3))

$$\lim_{x_3 \downarrow 0} E_1(x_1, x_3, t) = [V_0(t)/w] \sin(n\pi x_1/w) \Pi(x_1/w) \quad \text{for all } t \tag{9.5}$$

where $\Pi(x)$ is the rectangular function (see Eq. (2.4)). It is assumed that $V_0(t)$ starts to act at $t = 0$ and that prior to this instant the field vanishes throughout the configuration.

9.3   Field representations

In view of the Cagniard-DeHoop technique we employ the unilateral Laplace transformation with respect to time

$$\hat{V}_0(s) = \int_{t=0}^{\infty} \exp(-st)V_0(t)\mathrm{d}t \qquad (9.6)$$

in which s is taken to be real-valued and positive relying on Lerch's theorem [27, 44]. Further we use the wave slowness field representation

$$\left\{\hat{E}_1, \hat{E}_3, \hat{H}_2\right\}(x_1, x_3, s) = \frac{s}{2\pi\mathrm{i}} \int_{p=-\mathrm{i}\infty}^{\mathrm{i}\infty} \exp(-spx_1)\left\{\tilde{E}_1, \tilde{E}_3, \tilde{H}_2\right\}(p, x_3, s)\mathrm{d}p \qquad (9.7)$$

Under these transformations, the field equations (9.2) – (9.4) and the excitation condition (9.5) transform into

$$-sp\tilde{H}_2 - s\epsilon\tilde{E}_3 = 0 \qquad (9.8)$$
$$\partial_3\tilde{H}_2 + s\epsilon\tilde{E}_1 = 0 \qquad (9.9)$$
$$-sp\tilde{E}_3 - \partial_3\tilde{E}_1 - s\mu\tilde{H}_2 = 0 \qquad (9.10)$$

and

$$\lim_{x_3\downarrow 0}\tilde{E}_1(p, x_3, s) = \mathrm{i}^{n-1}[\hat{V}_0(s)/w]\left[\exp(spw/2) + \exp(-spw/2)\right]\tilde{G}(p, s) \qquad (9.11)$$

where

$$\tilde{G}(p, s) = \frac{1}{2}\left(\frac{1}{ps + \mathrm{i}n\pi/w} + \frac{1}{ps - \mathrm{i}n\pi/w}\right) \qquad (9.12)$$

The bounded slowness-domain field quantities follow from (9.8) – (9.11) by expressing them in the form

$$\{\tilde{E}_1, \tilde{E}_3, \tilde{H}_2\}(p, x_3, s) = \{\gamma_0/\epsilon_0, -p/\epsilon_0, 1\}\tilde{A}(p, s)\exp[-s\gamma_0(p)x_3] \qquad (9.13)$$

where $\tilde{A}(p, s)$ follows from the application of the excitation condition as

$$\tilde{A}(p, s) = \epsilon_0\tilde{E}_1(p, 0, s)/\gamma_0(p) \qquad (9.14)$$

in which

$$\gamma_0(p) = (1/c_0^2 - p^2)^{1/2} \quad \text{with } \mathrm{Re}[\gamma_0(p)] > 0 \qquad (9.15)$$

for all $p \in \mathbb{C}$.

9.4 The time-domain radiated fields

In this section we provide the time-domain fields radiated into the domain $\mathcal{D}$. Using the results of Section 9.3 we express them as

$$\left\{\hat{E}_1, \hat{E}_3, \hat{H}_2\right\}(x_1, x_3, s) =$$

$$\frac{s\hat{V}_0(s)}{2\pi w \mathrm{i}}\mathrm{i}^{n-1}\int_{p=-\infty}^{\mathrm{i}\infty}\exp\left\{-s[pX_\mathrm{a} + \gamma_0(p)x_3]\right\}\tilde{G}(p,s)\left\{1, -\frac{p}{\gamma_0(p)}, \frac{\epsilon_0}{\gamma_0(p)}\right\}\mathrm{d}p$$

$$+\frac{s\hat{V}_0(s)}{2\pi w \mathrm{i}}\mathrm{i}^{n-1}\int_{p=-\infty}^{\mathrm{i}\infty}\exp\left\{-s[pX_\mathrm{b} + \gamma_0(p)x_3]\right\}\tilde{G}(p,s)\left\{1, -\frac{p}{\gamma_0(p)}, \frac{\epsilon_0}{\gamma_0(p)}\right\}\mathrm{d}p \qquad (9.16)$$

with $X_\mathrm{a} = x_1 + w/2$ and $X_\mathrm{b} = x_1 - w/2$. The algebraic parts of the integrands do not contain any propagation coefficient that differs from the propagation coefficient $\gamma_0(p)$ in the propagation factors. This has the consequence that the corresponding Cagniard-DeHoop contours for a positive horizontal offset intersect the real p-axis in between $p = 0$ and $p = 1/c_0$, implying the absence of head-waves. The time-domain counterparts are found via the Cagniard-DeHoop technique as described in Appendix C. In this way, we can arrive at

$$\{E_1, E_3, H_2\}(x_1, x_3, t) =$$

$$\frac{\partial_t V_0(t)}{w} \overset{(t)}{*} \frac{\mathrm{i}^{n-1}}{\pi}\int_{\tau=T_\mathrm{a}}^{\infty}\mathrm{Re}\left(G[p_\mathrm{a}(\tau), t-\tau]\left\{\gamma_0[p_\mathrm{a}(\tau)], -p_\mathrm{a}(\tau), \epsilon_0\right\}\right)\frac{\mathrm{d}\tau}{(\tau^2 - T_\mathrm{a}{}^2)}$$

$$+\frac{\partial_t V_0(t)}{w} \overset{(t)}{*} \frac{\mathrm{i}^{n-1}}{\pi}\int_{\tau=T_\mathrm{b}}^{\infty}\mathrm{Re}\left(G[p_\mathrm{b}(\tau), t-\tau]\left\{\gamma_0[p_\mathrm{b}(\tau)], -p_\mathrm{b}(\tau), \epsilon_0\right\}\right)\frac{\mathrm{d}\tau}{(\tau^2 - T_\mathrm{b}{}^2)}$$

$$+\Pi\left(\frac{x_1}{w}\right)\left\{\left(\frac{\epsilon_0}{\mu_0}\right)^{1/2}\partial_t, \partial_3, \partial_1\right\}\frac{V_0(t)}{w} \overset{(t)}{*} J_0\left[\frac{n\pi c_0}{w}\left(t^2 - \frac{x_3^2}{c_0^2}\right)^{1/2}\right]$$

$$\times H\left(t - \frac{x_3}{c_0}\right)\sin(n\pi x_1/w) \qquad (9.17)$$

with

$$p_\mathrm{a,b}(\tau) = \left\{X_\mathrm{a,b}\tau + \mathrm{i}x_3(\tau^2 - T_\mathrm{a,b}{}^2)^{1/2}\right\}/\left\{X_\mathrm{a,b}{}^2 + x_3^2\right\} \qquad (9.18)$$

$$\gamma_0[p_\mathrm{a,b}(\tau)] = \left\{x_3\tau - \mathrm{i}X_\mathrm{a,b}(\tau^2 - T_\mathrm{a,b}{}^2)^{1/2}\right\}/\left\{X_\mathrm{a,b}{}^2 + x_3^2\right\} \qquad (9.19)$$

$$T_\mathrm{a,b} = (X_\mathrm{a,b}{}^2 + x_3^2)^{1/2}/c_0 \qquad (9.20)$$

and

$$G(p, \tau) = \cos(n\pi\tau/pw)/p \qquad (9.21)$$

provided that $p \neq 0$. The real parts in (9.17) can be easily found

$$
\begin{aligned}
\mathrm{Re}\left\{ \tilde{G}[p_{\mathrm{a,b}}(\tau), t - \tau]\gamma_0[p_{\mathrm{a,b}}(\tau)]\right\} &= \frac{x_3 X_{\mathrm{a,b}}}{c_0^2 \tau^2 - x_3^2} \cos\left[\frac{n\pi(t-\tau)}{w}\frac{X_{\mathrm{a,b}}\tau}{\tau^2 - x_3^2/c_0^2}\right] \\
&\times \cosh\left[\frac{n\pi(t-\tau)}{w}\frac{x_3(\tau^2 - T_{\mathrm{a,b}}{}^2)^{1/2}}{\tau^2 - x_3^2/c_0^2}\right] \\
&- \frac{\tau(\tau^2 - T_{\mathrm{a,b}}{}^2)^{1/2}}{\tau^2 - x_3^2/c_0^2}\sin\left[\frac{n\pi(t-\tau)}{w}\frac{X_{\mathrm{a,b}}\tau}{\tau^2 - x_3^2/c_0^2}\right] \\
&\times \sinh\left[\frac{n\pi(t-\tau)}{w}\frac{x_3(\tau^2 - T_{\mathrm{a,b}}{}^2)^{1/2}}{\tau^2 - x_3^2/c_0^2}\right] \quad (9.22)
\end{aligned}
$$

for E_1 field component and

$$
\begin{aligned}
\mathrm{Re}\left\{ \tilde{G}[p_{\mathrm{a,b}}(\tau), t - \tau]p_{\mathrm{a,b}}(\tau)\right\} &= \cos\left[\frac{n\pi(t-\tau)}{w}\frac{X_{\mathrm{a,b}}\tau}{\tau^2 - x_3^2/c_0^2}\right] \\
&\times \cosh\left[\frac{n\pi(t-\tau)}{w}\frac{x_3(\tau^2 - T_{\mathrm{a,b}}{}^2)^{1/2}}{\tau^2 - x_3^2/c_0^2}\right] \quad (9.23)
\end{aligned}
$$

for E_3 field component and finally

$$
\begin{aligned}
\mathrm{Re}\left\{ \tilde{G}[p_{\mathrm{a,b}}(\tau), t - \tau]\right\} &= \frac{X_{\mathrm{a,b}}\tau}{\tau^2 - x_3^2/c_0^2} \cos\left[\frac{n\pi(t-\tau)}{w}\frac{X_{\mathrm{a,b}}\tau}{\tau^2 - x_3^2/c_0^2}\right] \\
&\times \cosh\left[\frac{n\pi(t-\tau)}{w}\frac{x_3(\tau^2 - T_{\mathrm{a,b}}{}^2)^{1/2}}{\tau^2 - x_3^2/c_0^2}\right] \\
&- \frac{x_3(\tau^2 - T_{\mathrm{a,b}}{}^2)^{1/2}}{\tau^2 - x_3^2/c_0^2}\sin\left[\frac{n\pi(t-\tau)}{w}\frac{X_{\mathrm{a,b}}\tau}{\tau^2 - x_3^2/c_0^2}\right] \\
&\times \sinh\left[\frac{n\pi(t-\tau)}{w}\frac{x_3(\tau^2 - T_{\mathrm{a,b}}{}^2)^{1/2}}{\tau^2 - x_3^2/c_0^2}\right] \quad (9.24)
\end{aligned}
$$

for H_2 field component.

The evaluation of the fields exactly above the radiating edge, i.e. for $X_{\mathrm{a}} = 0$ or for $X_{\mathrm{b}} = 0$, requires increased attention. In this case, one of the Cagniard-DeHoop paths runs along the imaginary axis, starting at $p_{\mathrm{a}} = 0$ or $p_{\mathrm{b}} = 0$. For this case, the Eq. (9.17) is not valid because of the division by zero in (9.21). Nevertheless, one can show from (9.16) that for $\{E_1, H_2\}$ field components, the integration along the imaginary axis in the sense of Cauchy principal value gives only half-pole contributions that correspond to the third term in the right-hand of (9.17). On the other hand, the half-pole contributions connected with E_3 cancel each other, but the integration along the rest of the integration path gives a nonzero value except for the arrival time when the field is also zero. One can encounter numerical difficulties on account of the exponential growing of the integrands in (9.23). A solution of this problem can be found in a linear interpolation between the values of E_3 evaluated with the help of (9.17) at some neighbouring points or in a numerical differentiation induced by Eq. (9.2).

9.5   Illustrative numerical examples

This section provides illustrative numerical examples for the case of power-exponential excitation pulses with $V_{\max} = 1$, $\nu = 2$ ($t_w/t_r = 1.8473$), $c_0 t_w = 0.1847w$ ($t_r = 0.1w/c_0$) as depicted in Fig. 7.2.

All cylindrical wave field constituents contain time-convolution integrals with inverse square-root singularities at the arrival time of the wave. These are numerically handled via a stretching of the variable of integration according to

$$\tau = T_a \cosh(u) \quad \text{for } 0 < u < \infty \tag{9.25}$$

with the Jacobian

$$\frac{\partial \tau}{\partial u} = T_a \sinh(u) = (\tau^2 - T_a{}^2)^{1/2} \tag{9.26}$$

According to Fig. 9.1, two observation points at the vertical level $x_3 = w$ have been chosen with horizontal offsets: (A) $x_1/w = 0.25$; (B) $x_1/w = 1$. Note that due to the antisymmetry of the excitation field distribution, only the vertical electric field component E_3 is nonzero along $x_1/w = 0$ for all TM modes, while for the TEM mode uniform excitation this component is zero and $\{E_1, H_2\}$ components form the plane wave here.

At the chosen observation points, the pulse shapes of $\{E_1, E_3, H_2\}(x_1, x_3, t)$ are computed within the time-window $0 < c_0 t/w < 4.0$ for two successive TM modes with $n = \{1, 3\}$ and for TEM mode. In the following figures, normalized $E_{1,3}$ represents $E_{1,3}w/V_{\max}$, normalized H_2 represents $(\mu_0/\epsilon_0)^{1/2}H_2w/V_{\max}$ and normalized time stands for $c_0 t/w$.

Figures 9.2 – 9.4 show the pulse shapes of $\{E_1, E_3, H_2\}(x_1, x_3, t)$ at point (A), $x_1/w = 0.25$, $x_3/w = 1$. Since this observation point lies above the radiating slot, all time-domain responses start before the arrival time T_b due to the wave progressing upward from the aperture.

Figures 9.5 – 9.7 show the pulse shapes of $\{E_1, E_3, H_2\}(x_1, x_3, t)$ at point (B), $x_1/w = 1$, $x_3/w = 1$. In this case, the observation point does not lie above the radiating slot and the resposenses start at the arrival connected with the closer edge.

In all figures can be observed how the spatial changes in the distribution of the excitation field manifest themselves in the temporal responses of radiated electromagnetic field components.
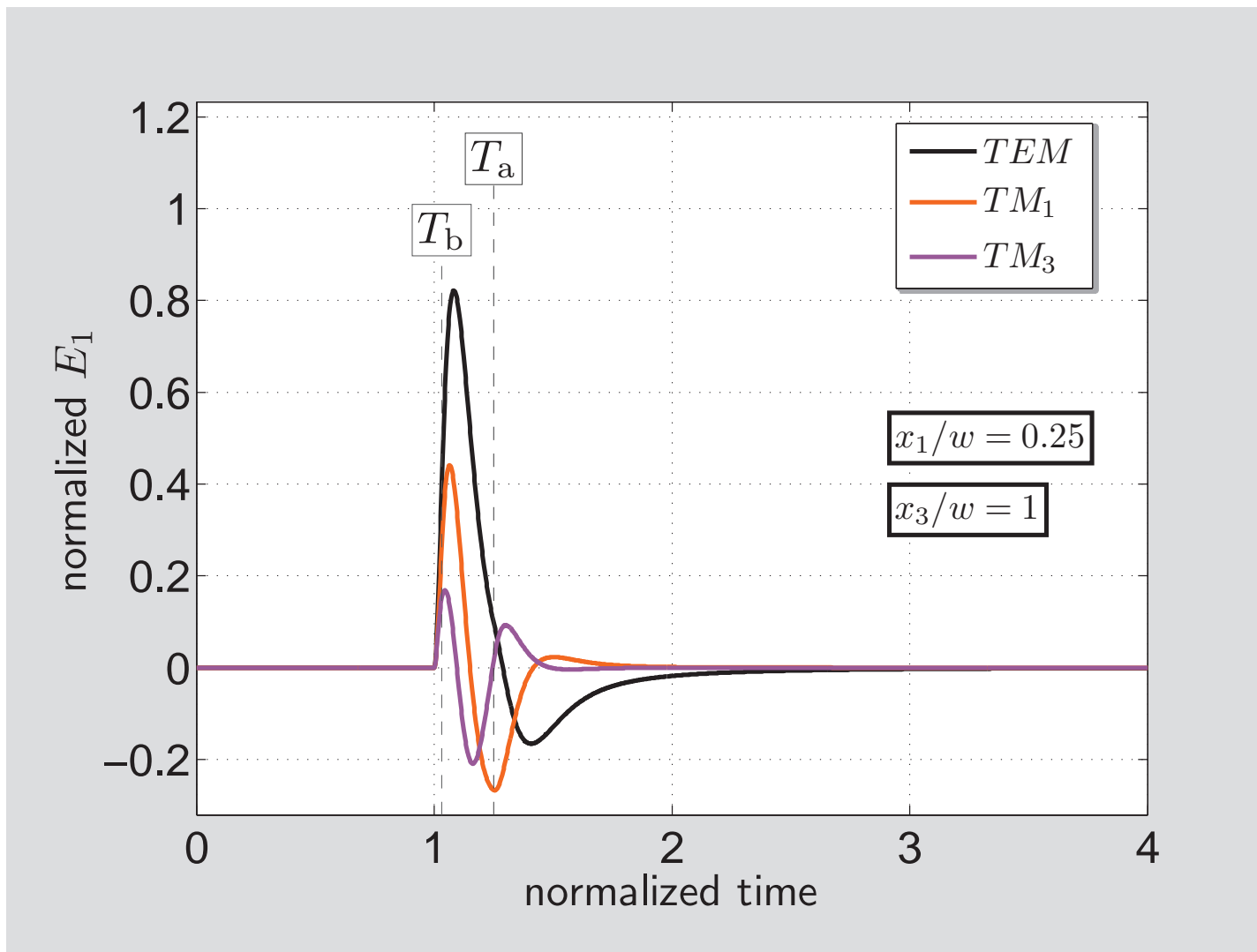
Figure 9.2: Normalized E_1 time-domain response at $x_1/w = 0.25$, $x_3/w = 1$. Parameters of the excitation pulse are $c_0 t_w/w = 0.1847$, $\nu = 2$.
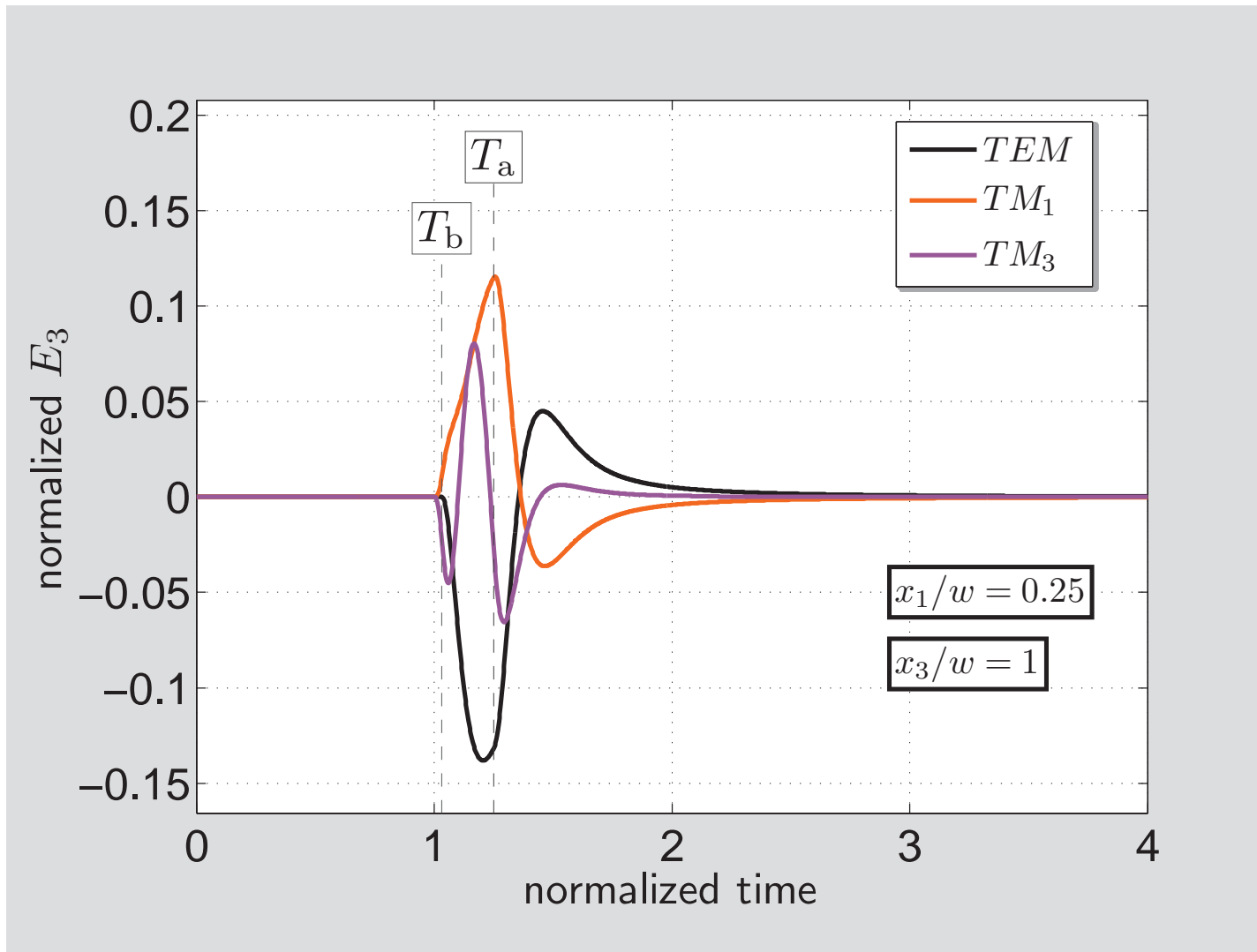
Figure 9.3: Normalized E_3 time-domain response at $x_1/w = 0.25$, $x_3/w = 1$. Parameters of the excitation pulse are $c_0 t_w/w = 0.1847$, $\nu = 2$.
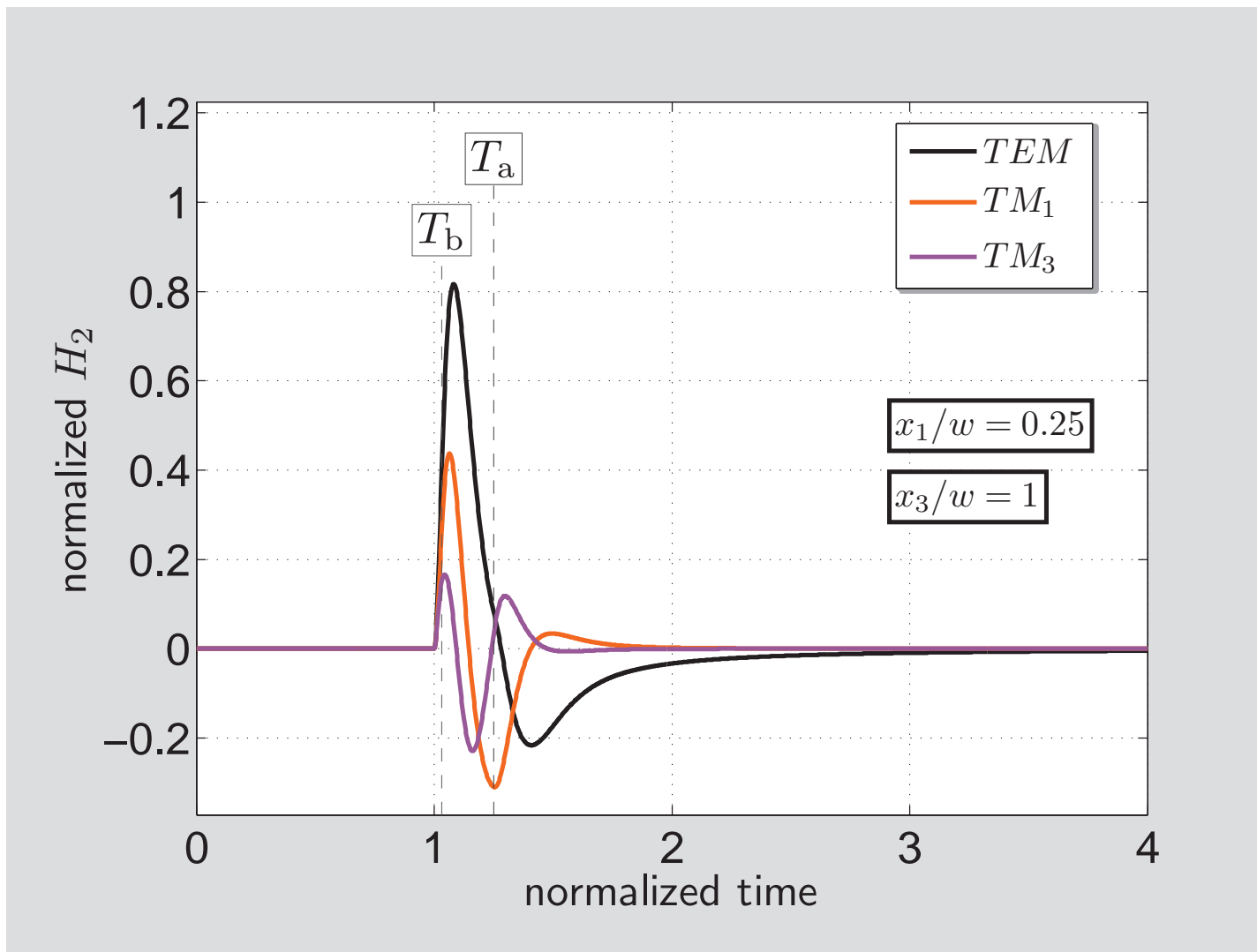
Figure 9.4: Normalized H_2 time-domain response at $x_1/w = 0.25$, $x_3/w = 1$. Parameters of the excitation pulse are $c_0 t_w/w = 0.1847$, $\nu = 2$.
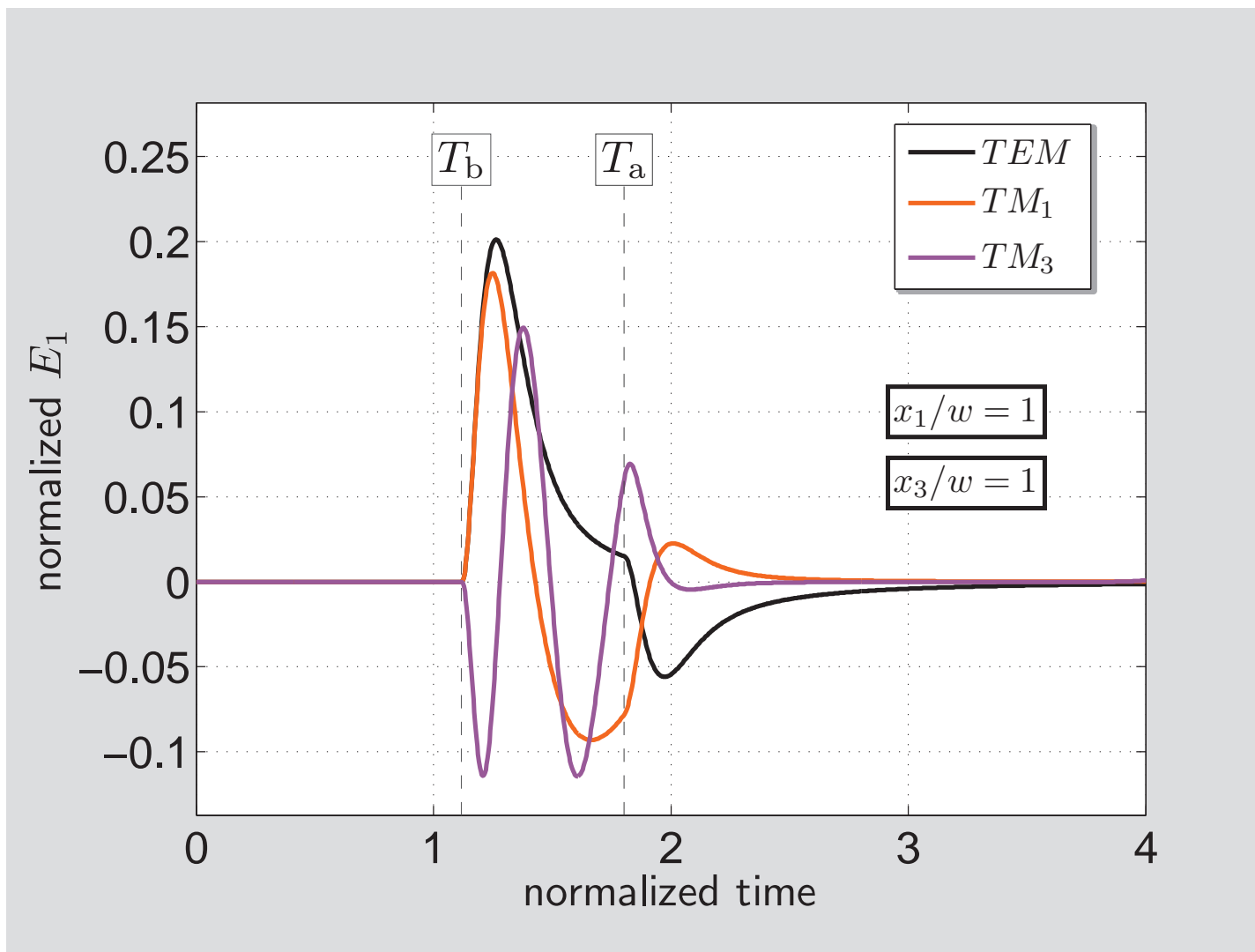
Figure 9.5: Normalized E_1 time-domain response at $x_1/w = 1$, $x_3/w = 1$. Parameters of the excitation pulse are $c_0 t_w/w = 0.1847$, $\nu = 2$.
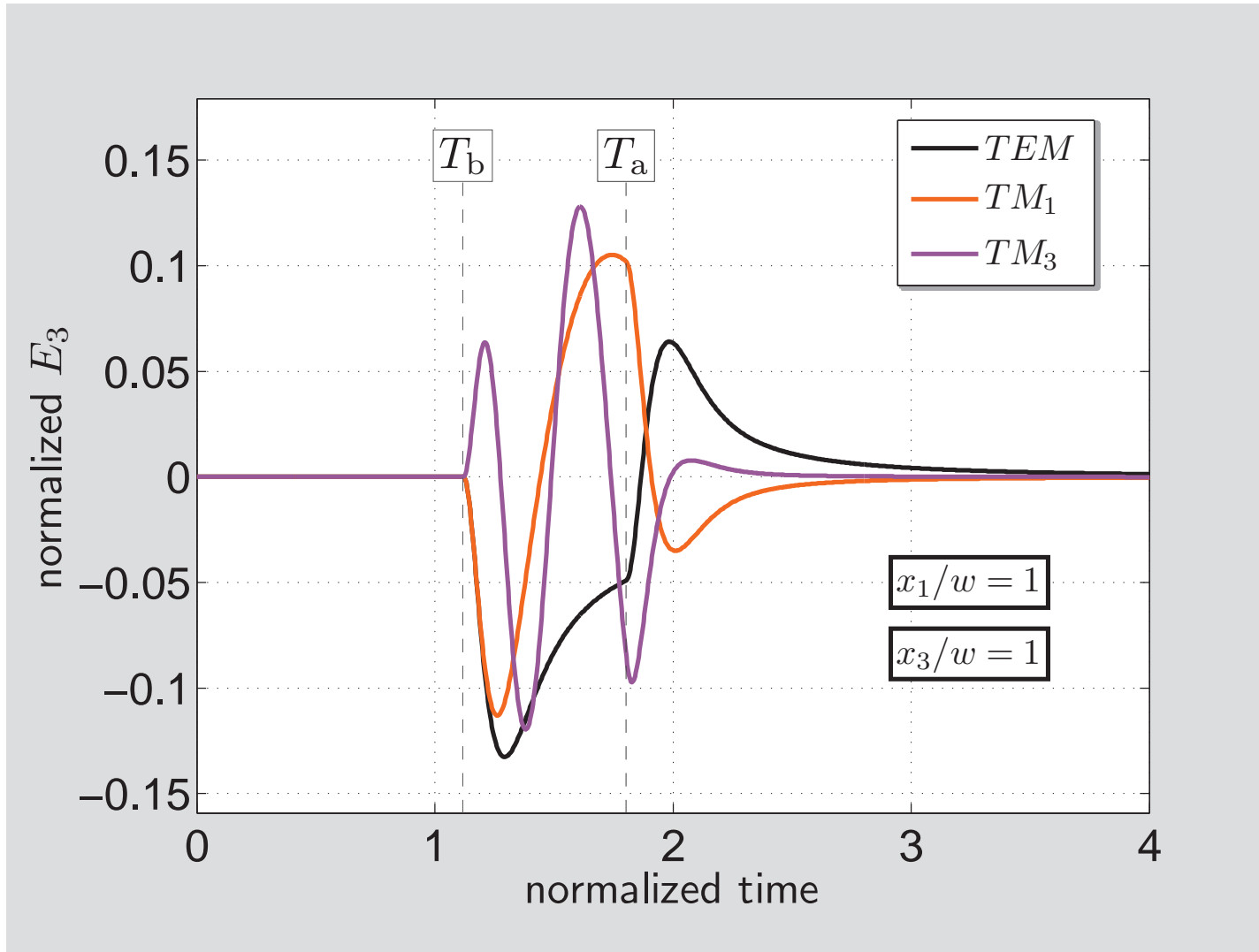
Figure 9.6: Normalized E_3 time-domain response at $x_1/w = 1$, $x_3/w = 1$. Parameters of the excitation pulse are $c_0 t_w/w = 0.1847$, $\nu = 2$.
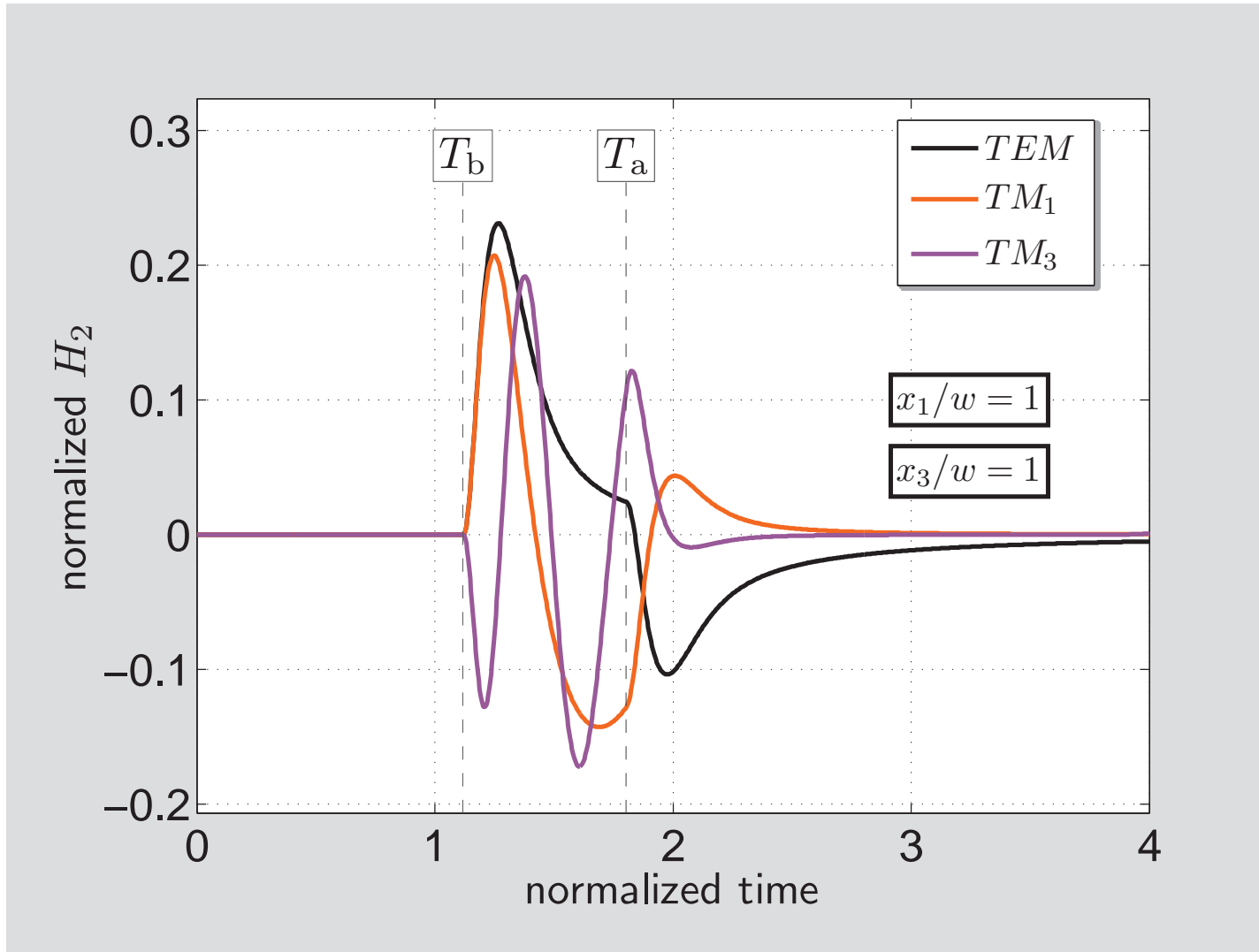
Figure 9.7: Normalized H_2 time-domain response at $x_1/w = 1$, $x_3/w = 1$. Parameters of the excitation pulse are $c_0 t_w/w = 0.1847$, $\nu = 2$.

Chapter 10

Conclusions

Currently used computational tools are not up to the demands that came up with the recent advances in the communication systems. Realizing the lack of the pulsed-field computational tools, we have developed one for the exact time-domain analysis of some typical radiators used in antenna arrays. The applied approach is entirely built upon the space-time description and does not introduce any mathematical artifacts that follow from frequency-domain descriptions. As it turned out, the developed pulsed-field computational tool provides the capabilities that lie far beyond the scope of currently used software instruments. The most striking feature is the possibility of the exact evaluation of all excited pulsed electromagnetic field components at a given observation point within a finite time-window. The obtained results have proved to be applicable to the design of the antenna arrays with agile beam steering and beam shaping facilities.

To accommodate the identified objectives of the thesis, we have employed the Cagniard-DeHoop technique. It has been demonstrated that this technique is capable of providing the exact time-domain closed-form expressions that give physical insights into the radiation mechanism, which is necessary for the efficient design process in practice. These results thus form the solid fundamental basis for novel *time-domain* applications of antenna arrays.

Throughout the thesis, the pulsed electromagnetic field excited by controlled aperture source distributions is investigated in various problem configurations. The common feature of the solution of all problems is the development of the generic integral representation for the radiated electromagnetic field components, which significantly contribute to the brevity and lucidity of the thesis. The handling with generic integral representations can be designated as the theoretical cornerstone of the thesis. Most of the chapters are supplemented with numerical examples that clearly illustrate the main features of a pertinent problem in hand.

In Chapter 3 the pulsed electromagnetic field radiation from the narrow slot has been adressed. Chapter provided more ways for solving the problem and, thus, helped the reader to understand the approach applied troughout the thesis.

Chapter 4 aimed at the investigation of the pulsed electromagnetic radiation from the narrow slot antenna in the presence of the additional perfectly electrically conducting screen. This chapter has illustrated how to accommodate the reflected time-domain constituents pertinent to the narrow slot antenna.

In Chapter 5 the pulsed electromagnetic radiation from the narrow slot with the dielectric covering was investigated. It has been shown that the applied approach is capable of describing all intricate phenomena that arise on account of the nonzero contrast in electromagnetic properties above the narrow radiating slot. The obtained exact expressions make possible to design a pulse-excited antenna array of narrow slots taking into account the influence of the protecting dielectric covering.

From Chapter 6 on, the more realistic aperture radiators, with a finite slot width, are considered. For this type of radiating apertures, it was demonstrated that the excitation via a wide slot shows additional features in that the corners show a separate diffractive behavior with accompanying wavefronts. Chapter 6 has described the pulsed radiation behavior of the free-standing wide slot and served as the point of the departure for the following chapters. Here, it has been demonstrated how the obtained results can be used for the design of a pulsed-field antenna array.

Chapter 7 focused on the analysis of the pulsed electromagnetic radiation from the wide slot antenna in the presence of the additional perfectly electrically conducting screen. This chapter has illustrated how to deal with the reflected time-domain constituents pertinent to the wide slot antenna.

In Chapter 8 the pulsed electromagnetic radiation from the wide slot with the dielectric covering was investigated. It has been shown that the applied approach is capable of describing all intricate phenomena that arise on account of the nonzero contrast in electromagnetic properties above the wide radiating slot. The obtained exact expressions make possible to design a pulse-excited antenna array of wide slots taking into account the influence of the protecting dielectric covering.

Chapter 9 concerned the handling of a nonuniform excitation field distribution, which can be applied on all previous problem configurations with the wide slot. It has been shown that the modal excitation can be easily taken into account at the expense of having to evaluate an additional one-dimensional integral over a finite interval. The provided numerical examples have demonstrated how the spatial changes in the modal excitation manifest themselves in the time-domain responses of the radiated field components.

The prospective developments and the course of the future research rest in a generalization of our approach for three-dimensional radiators and in the applications of the obtained results. In this respect, we can provide the following examples:

- The description of the interaction of the analyzed aperture antenna array and a scatterer through the time-domain field/source reciprocity theorem and a development of pulsed-field radar identification methods.

- The analysis and design of time-domain near-field focused antenna arrays.

- The design and optimisation of wireless integrated circuits interconnects.

Having pinpointed some of the future scientific targets, we conclude this thesis.

Appendix A

A narrow slot antenna:
The Cagniard-DeHoop technique

This section provides the description of Cagnuiard-DeHoop method dealing with the generic integral representation concerning a narrow slot antenna.[5] The generic integral form of the wave constituents in the interior of the dielectric slab and on its boundary is (s = time Laplace-transform parameter, p = slowness parameter along x_1)

$$\hat{W}(x_1, x_3, s) = \frac{s\hat{V}_0(s)}{2\pi i} \int_{p=-i\infty}^{i\infty} \exp\{-s[pX + \gamma_1(p)Z]\}\tilde{A}[\gamma_{0,1}(p)]\mathrm{d}p \qquad \text{(A.1)}$$

where $\tilde{A}[\gamma_{0,1}(p)]$ is an algebraic function of $\gamma_{0,1}(p)$ and has the branch cuts in accordance with $\mathrm{Re}[\gamma_{0,1}(p)] > 0$, i.e. $\{1/c_{0,1} < |\mathrm{Re}(p)| < \infty, \mathrm{Im}(p) = 0\}$ and X and Z are the propagation paths in the x_1- and x_3-directions. We assume that $c_0 \geqslant c_1$. Under the application of Cauchy's theorem and Jordan's lemma of complex function theory, the path of integration in (A.1) is replaced with one along the 'Cagniard-DeHoop path' defined through

$$pX + \gamma_1(p)Z = \tau \text{ for } T < \tau < \infty \qquad \text{(A.2)}$$

where τ is real-valued.

Body-wave path

The *body-wave path* follows from (A.2) as the hyperbolic arc $\mathcal{C}^{\mathrm{BW}} \cup \mathcal{C}^{\mathrm{BW}*}$, where

$$\mathcal{C}^{\mathrm{BW}} = \left\{ p^{\mathrm{BW}}(X, Z, \tau) = \frac{X\tau + iZ(\tau^2 - T_{\mathrm{BW}}^2)^{1/2}}{X^2 + Z^2}, T_{\mathrm{BW}} < \tau < \infty \right\} \qquad \text{(A.3)}$$

with

$$T_{\mathrm{BW}} = (X^2 + Z^2)^{1/2}/c_1 \qquad \text{(A.4)}$$

---

as the arrival time of the body-wave constituent. Along this path

$$\gamma_1(p^{\mathrm{BW}}) = \frac{Z\tau - \mathrm{i}X(\tau^2 - T_{\mathrm{BW}}^2)^{1/2}}{X^2 + Z^2} \quad \text{for } T_{\mathrm{BW}} < \tau < \infty \tag{A.5}$$

and the Jacobian of the mapping from p to τ is

$$\frac{\partial p^{\mathrm{BW}}}{\partial \tau} = \frac{\mathrm{i}\gamma_1(p^{\mathrm{BW}})}{(\tau^2 - T_{\mathrm{BW}}^2)^{1/2}} \quad \text{for } T_{\mathrm{BW}} < \tau < \infty \tag{A.6}$$

The body-wave path replaces the path of integration in (A.1) as long as the intersection of this path with the real p-axes does not lie on the branch cut associated with $\gamma_0(p)$, i.e. for points of observation in the range $\cos(\phi) = |X|/(X^2 + Z^2)^{1/2} < c_1/c_0$. For points of observation outside this range, the body-wave path has to be supplemented with a connecting loop integral along the branch cut associated with $\gamma_0(p)$. This loop integral yields the head-wave contribution to the wave constituent.

Head-wave path

The parametrized *head-wave path* follows from (A.2) as the loop $\mathcal{C}^{\mathrm{HW}} \cup \mathcal{C}^{\mathrm{HW}*}$, where

$$\mathcal{C}^{\mathrm{HW}} = \left\{ p^{\mathrm{HW}}(X, Z, \tau) = \frac{X\tau - Z(T_{\mathrm{BW}}^2 - \tau^2)^{1/2}}{X^2 + Z^2} + \mathrm{i}0, T_{\mathrm{HW}} < \tau < T_{\mathrm{BW}} \right\} \tag{A.7}$$

with

$$T_{\mathrm{HW}} = X/c_0 + Z(1/c_1^2 - 1/c_0^2)^{1/2} \tag{A.8}$$

as the arrival time of the head-wave constituent. Along this path

$$\gamma_1(p^{\mathrm{HW}}) = \frac{Z\tau + X(T_{\mathrm{BW}}^2 - \tau^2)^{1/2}}{X^2 + Z^2} \quad \text{for } T_{\mathrm{HW}} < \tau < T_{\mathrm{BW}} \tag{A.9}$$

and the Jacobian of the mapping from p to τ is

$$\frac{\partial p^{\mathrm{HW}}}{\partial \tau} = \frac{\gamma_1(p^{\mathrm{HW}})}{(T_{\mathrm{BW}}^2 - \tau^2)^{1/2}} \quad \text{for } T_{\mathrm{HW}} < \tau < T_{\mathrm{BW}} \tag{A.10}$$

The corresponding wave constituents follow from combining the two complex conjugate parts of the paths and applying Schwarz' theorem of complex function theory.

Time-domain body-wave constituent

The s-domain body-wave constituent follows from (A.1) as

$$\hat{W}(x_1, x_3, s) = \frac{s\hat{V}_0(s)}{\pi} \int_{\tau=T_{\mathrm{BW}}}^{\infty} \exp(-s\tau) \operatorname{Im} \left\{ \tilde{A} \left[\gamma_{0,1}(p^{\mathrm{BW}}) \right] \frac{\partial p^{\mathrm{BW}}}{\partial \tau} \right\} \mathrm{d}\tau \tag{A.11}$$
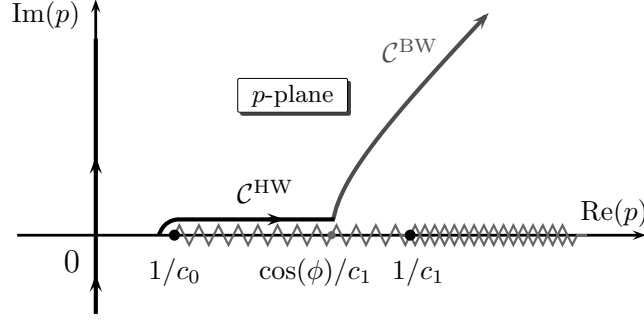
Figure A.1: Illustration of p-plane with body- and head-wave parts of the Cagniard-DeHoop contour $\mathcal{C}^{\mathrm{BW}}$ and $\mathcal{C}^{\mathrm{HW}}$ for $X > 0$, original integration contour $\mathrm{Re}(p) = 0$, branch-points $\{1/c_0, 1/c_1\}$ with corresponding branch-cuts and the point of intersection of $\mathcal{C}^{\mathrm{BW}}$ with $\mathrm{Im}(p) = 0$, $\cos(\phi)/c_1$.

On account of Lerch's uniqueness theorem of the unilateral Laplace transformation [27, 44] the time-domain constituent then follows as

$$W(x_1, x_3, t) = \partial_t V_0(t) \overset{(t)}{*} \pi^{-1} \mathrm{Re} \left\{ \tilde{A} \left\{ \gamma_{0,1} \left[p^{\mathrm{BW}}(x_1, x_3, t) \right] \right\} \gamma_1 \left[p^{\mathrm{BW}}(x_1, x_3, t) \right] \right\}$$
$$\times H(t - T_{\mathrm{BW}})(t^2 - T_{\mathrm{BW}}^2)^{-1/2} \tag{A.12}$$

where (A.6) has been used and $\overset{(t)}{*}$ denotes convolution with respect to time.

Time-domain head-wave constituent

The s-domain head-wave constituent follows from (A.1) as

$$\hat{W}(x_1, x_3, s) = \frac{s \hat{V}_0(s)}{\pi} \int_{\tau = T_{\mathrm{HW}}}^{T_{\mathrm{BW}}} \exp(-s\tau) \mathrm{Im} \left\{ \tilde{A} \left[\gamma_{0,1}(p^{\mathrm{HW}}) \right] \frac{\partial p^{\mathrm{HW}}}{\partial \tau} \right\} \mathrm{d}\tau \tag{A.13}$$

Again, on account of Lerch's uniqueness theorem of the unilateral Laplace transformation [27, 44] the time-domain constituent then follows as

$$W(x_1, x_3, t) = \partial_t V_0(t) \overset{(t)}{*} \pi^{-1} \mathrm{Im} \left\{ \tilde{A} \left\{ \gamma_{0,1} \left[p^{\mathrm{HW}}(x_1, x_3, t) \right] \right\} \gamma_1 \left[p^{\mathrm{HW}}(x_1, x_3, t) \right] \right\}$$
$$\times \Pi \left[(t - T_{\mathrm{C}})/T_{\mathrm{L}} \right] (T_{\mathrm{BW}}^2 - t^2)^{-1/2} \tag{A.14}$$

where (A.10) has been used, $\Pi(x)$ is the rectangular function and

$$T_{\mathrm{C}} = (T_{\mathrm{HW}} + T_{\mathrm{BW}})/2 \tag{A.15}$$
$$T_{\mathrm{L}} = T_{\mathrm{BW}} - T_{\mathrm{HW}} \tag{A.16}$$

These results are used in the main text.

Appendix B

A wide slot antenna:
The Cagniard-DeHoop technique

This section provides the description of Cagniard-DeHoop method dealing with the generic integral representation concerning a slot antenna with a finite slot width.[6] The generic form of the transversal wave constituents in the interior of the dielectric slab and on its boundary is (s = time Laplace-transform parameter, p = slowness parameter along x_1)

$$\hat{W}(x_1, x_3, s) = \hat{V}_0(s)[\hat{W}_{\mathrm{b}}(x_1, x_3, s) - \hat{W}_{\mathrm{a}}(x_1, x_3, s)] \tag{B.1}$$

with

$$\hat{W}_{\mathrm{a}}(x_1, x_3, s) = \frac{1}{2\pi\mathrm{i}} \int_{p=-\mathrm{i}\infty}^{\mathrm{i}\infty} \frac{\tilde{A}[\gamma_{0,1}(p)]}{p} \exp\{-s[pX_{\mathrm{a}} + \gamma_1(p)Z]\}\mathrm{d}p \tag{B.2}$$

where $\tilde{A}[\gamma_{0,1}(p)]$ is an algebraic function of $\gamma_{0,1}(p)$, $X_{\mathrm{a}} = x_1 - a$ and Z are the propagation paths in the x_1- and x_3-directions. We assume that $c_0 \geqslant c_1$ and $a < b$. In this section, all conclusions for the expressions marked with 'a' are the same as for those marked with 'b', only with 'a' replaced with 'b'. The right hand side of (B.1) has no singularity except of the branch points connected with branch cuts due to $\tilde{A}[\gamma_{0,1}(p)]$ with $\mathrm{Re}[\gamma_{0,1}(p)] > 0$, i.e. $\{1/c_{0,1} < |\mathrm{Re}(p)| < \infty, \mathrm{Im}(p) = 0\}$. However, the desired Cagniard-DeHoop technique can only be applied to the separate terms, each of which has a simple pole at $p = 0$. To accomodate this situation, the path of integration is replaced with one that is indented to the right with a semi-circular arc with center at $p = 0$ and vanishingly small radius. This leads for the integration to the same result. Subsequently, under the application of Cauchy's theorem and Jordan's lemma of complex function theory, the paths of integration in (B.1)–(B.2) are replaced with ones along the Cagniard-DeHoop contours defined through

$$pX_{\mathrm{a,b}} + \gamma_1(p)Z = \tau \text{ for } T < \tau < \infty \tag{B.3}$$

where τ is real-valued. From here on, the complex slowness parameters connected with the horizontal offsets X_{a} and X_{b} are denoted p_{a} and p_{b}, respectively.

---

[6]Part of this chapter is based on the paper [19]; ©[2011] IEEE. The permission of IEEE and co-authors Adrianus T. De Hoop and Ioan E. Lager to reproduce these results is gratefully acknowledged.

Three different cases have to be distinguished. In the region $x_1 < a$, the indented contours are deformed into the Cagniard-DeHoop contours lying in the left halves of p_a and p_b complex planes. With the chosen indentation, the pole contributions in $p_{a,b}$-planes are present. But, in view of (B.1), both residues cancel each other. In the region $x_1 > b$, the indented contours are deformed into the Cagniard-DeHoop contours lying in the right halves of p_a and p_b complex planes. With the chosen indentation, the pole contributions are not present. Finally, in the region above the slot $a < x_1 < b$, the indented contours are deformed into the Cagniard-DeHoop contours lying in the right half of p_a-plane and in the left half of p_b-plane (See Fig. B.1). With the chosen indentation, the pole contribution in p_b-plane has to be included. Along the lines $x_1 = a$ and $x_1 = b$, the indented integration contour becomes unchanged and the isolated simple pole is counted as one half, which corresponds to taking the Cauchy principal value.

Body-wave path

The *body-wave path* follows from (B.3) as the hyperbolic arc $\mathcal{C}_a^{\mathrm{BW}} \cup \mathcal{C}_a^{\mathrm{BW}*}$, where

$$\mathcal{C}_a^{\mathrm{BW}} = \left\{ p_a^{\mathrm{BW}}(X_a, Z, \tau) = \frac{X_a\tau + \mathrm{i}Z(\tau^2 - T_{\mathrm{BWa}}^2)^{1/2}}{X_a^2 + Z^2}, T_{\mathrm{BWa}} < \tau < \infty \right\} \tag{B.4}$$

with

$$T_{\mathrm{BWa}} = (X_a^2 + Z^2)^{1/2}/c_1 \tag{B.5}$$

as the arrival time of the body-wave constituent. Along this path

$$\gamma_1(p_a^{\mathrm{BW}}) = \frac{Z\tau - \mathrm{i}X_a(\tau^2 - T_{\mathrm{BWa}}^2)^{1/2}}{X_a^2 + Z^2} \quad \text{for } T_{\mathrm{BWa}} < \tau < \infty \tag{B.6}$$

and the Jacobian of the mapping from p_a to τ is

$$\frac{\partial p_a^{\mathrm{BW}}}{\partial \tau} = \frac{\mathrm{i}\gamma_1(p_a^{\mathrm{BW}})}{(\tau^2 - T_{\mathrm{BWa}}^2)^{1/2}} \quad \text{for } T_{\mathrm{BWa}} < \tau < \infty \tag{B.7}$$

The body-wave path replaces the path of integration in (B.1)–(B.2) as long as the intersection of this path with the real p_a-axes does not lie on the branch cut associated with $\gamma_0(p_a)$, i.e. for points of observation in the range $|X_a|/(X_a^2 + Z^2)^{1/2} < c_1/c_0$. For points of observation outside this range, the body-wave path has to be supplemented with a connecting loop integral along the branch cut associated with $\gamma_0(p_a)$. This loop integral yields the head-wave contribution to the wave constituent.

Head-wave path

The parametrized *head-wave path* follows from (B.3) as the loop $\mathcal{C}_a^{\mathrm{HW}} \cup \mathcal{C}_a^{\mathrm{HW}*}$, where

$$\mathcal{C}_a^{\mathrm{HW}} = \left\{ p_a^{\mathrm{HW}}(X_a, Z, \tau) = \frac{X_a\tau - Z(T_{\mathrm{BWa}}^2 - \tau^2)^{1/2}}{X_a^2 + Z^2} + \mathrm{i}0, T_{\mathrm{HWa}} < \tau < T_{\mathrm{BWa}} \right\} \tag{B.8}$$
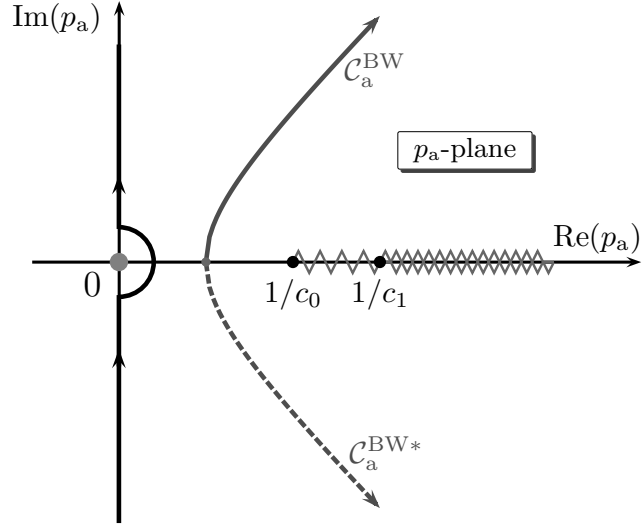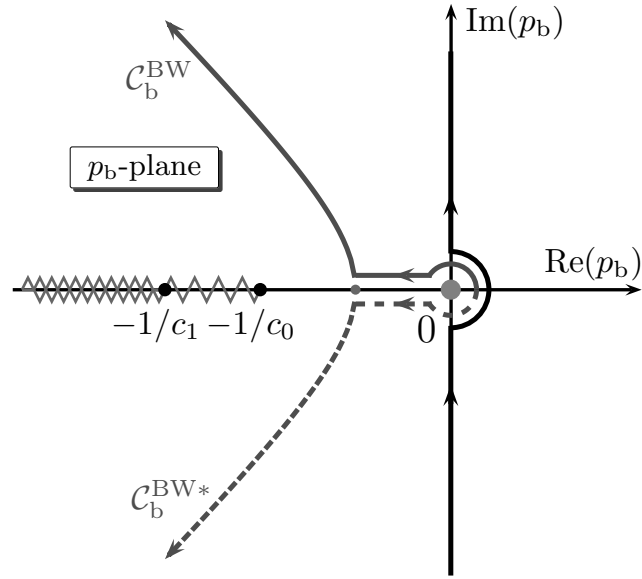
Figure B.1: Illustration of p-planes for $a < x_1 < b$, original integration contour with the indentation at origin and branch-points $\{1/c_0, 1/c_1\}$ with corresponding branch-cuts. (a) p_a-plane with the body-wave Cagniard-DeHoop contour $\mathcal{C}_a^{\mathrm{BW}} \cup \mathcal{C}_a^{\mathrm{BW}*}$; (b) p_b-plane with the body-wave part of the Cagniard-DeHoop contour $\mathcal{C}_b^{\mathrm{BW}} \cup \mathcal{C}_b^{\mathrm{BW}*}$.

with

$$T_{\text{HWa}} = X_{\text{a}}/c_0 + Z(1/c_1^2 - 1/c_0^2)^{1/2} \tag{B.9}$$

as the arrival time of the head-wave constituent. Along this path

$$\gamma_1(p_{\text{a}}^{\text{HW}}) = \frac{Z\tau + X(T_{\text{BWa}}^2 - \tau^2)^{1/2}}{X_{\text{a}}^2 + Z^2} \quad \text{for } T_{\text{HWa}} < \tau < T_{\text{BWa}} \tag{B.10}$$

and the Jacobian of the mapping from p_{a} to τ is

$$\frac{\partial p_{\text{a}}^{\text{HW}}}{\partial \tau} = \frac{\gamma_1(p_{\text{a}}^{\text{HW}})}{(T_{\text{BWa}}^2 - \tau^2)^{1/2}} \quad \text{for } T_{\text{HWa}} < \tau < T_{\text{BWa}} \tag{B.11}$$

The corresponding wave constituents follow from combining the two complex conjugate parts of the paths and applying Schwarz' theorem of complex function theory.

Plane-wave path

If $a \le x_1 \le b$ then a contribution from the simple pole at $p_{\text{b}} = 0$ has to be counted in. The parametrized *plane-wave path* consists of a circle with center at $p_{\text{b}} = 0$ and vanishingly small radius, i.e. $p_{\text{b}} = p_{\text{b}}^{\text{PW}}(\varepsilon, \theta)$, where

$$p_{\text{b}}^{\text{PW}} = \varepsilon \exp(\text{i}\theta) \quad \text{for } \tau = Z/c1 \tag{B.12}$$

and $\varepsilon \downarrow 0$, $0 \le \theta < 2\pi$. Along this path

$$\gamma_{0,1}(p_{\text{b}}^{\text{PW}}) = 1/c_{0,1} \quad \text{for } \tau = Z/c1 \tag{B.13}$$

Time-domain body-wave constituent

The s-domain body-wave constituent follows from (B.1)–(B.2) as

$$\hat{W}_{\text{a}}^{\text{BW}}(x_1, x_3, s) = \frac{1}{\pi} \int_{\tau = T_{\text{BWa}}}^{\infty} \exp(-s\tau) \, \text{Im} \left\{ \frac{\tilde{A}\left[\gamma_{0,1}(p_{\text{a}}^{\text{BW}})\right]}{p_{\text{a}}^{\text{BW}}} \frac{\partial p_{\text{a}}^{\text{BW}}}{\partial \tau} \right\} \text{d}\tau \tag{B.14}$$

On account of Lerch's uniqueness theorem of the unilateral Laplace transformation [27, 44] the time-domain body-wave constituent then follows as

$$W^{\text{BW}}(x_1, x_3, t) = V_0(t) \overset{(t)}{*} \left[W_{\text{b}}^{\text{BW}}(x_1, x_3, t) - W_{\text{a}}^{\text{BW}}(x_1, x_3, t)\right] \tag{B.15}$$

with

$$W_{\text{a}}^{\text{BW}}(x_1, x_3, t) = \pi^{-1}\text{Re}\left\{\tilde{A}\left\{\gamma_{0,1}\left[p_{\text{a}}^{\text{BW}}(X_{\text{a}}, x_3, t)\right]\right\} \gamma_1\left[p_{\text{a}}^{\text{BW}}(X_{\text{a}}, x_3, t)\right]/p_{\text{a}}^{\text{BW}}(X_{\text{a}}, x_3, t)\right\}$$
$$\times H(t - T_{\text{BWa}})(t^2 - T_{\text{BWa}}^2)^{-1/2} \tag{B.16}$$

where (B.7) has been used and $\overset{(t)}{*}$ denotes convolution with respect to time.
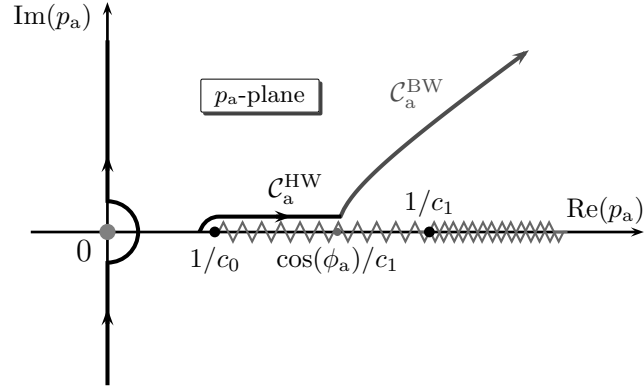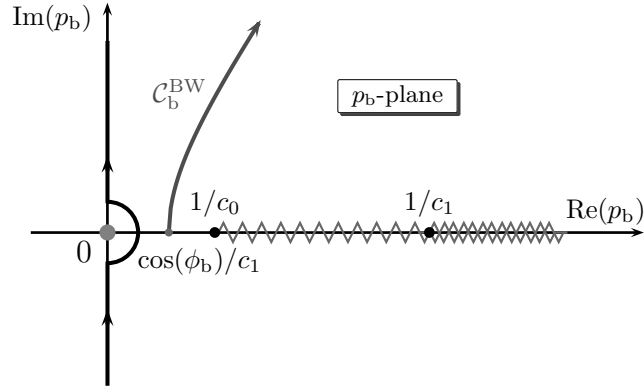
Figure B.2: Illustration of p-planes for the observation point B in Fig. 8.1 (not true-to-scale), original integration contour with the indentation at origin and branch-points $\{1/c_0, 1/c_1\}$ with corresponding branch-cuts. (a) p_a-plane with body- and head-wave parts of the Cagniard-DeHoop contour $\mathcal{C}_a^{BW}$ and $\mathcal{C}_a^{HW}$, $\cos(\phi_a) = X_a/(X_a^2 + Z^2)^{1/2}$; (b) p_b-plane with body-wave part of the Cagniard-DeHoop contour $\mathcal{C}_b^{BW}$, $\cos(\phi_b) = X_b/(X_b^2 + Z^2)^{1/2}$.

Time-domain head-wave constituent

The s-domain head-wave constituent follows from (B.1)–(B.2) as

$$\hat{W}_{\mathrm{a}}^{\mathrm{HW}}(x_1, x_3, s) = \frac{1}{\pi} \int_{\tau=T_{\mathrm{HWa}}}^{T_{\mathrm{BWa}}} \exp(-s\tau) \, \mathrm{Im} \left\{ \frac{\tilde{A}\left[\gamma_{0,1}(p_{\mathrm{a}}^{\mathrm{HW}})\right]}{p_{\mathrm{a}}^{\mathrm{HW}}} \frac{\partial p_{\mathrm{a}}^{\mathrm{HW}}}{\partial \tau} \right\} \mathrm{d}\tau \qquad \text{(B.17)}$$

On account of Lerch's uniqueness theorem of the unilateral Laplace transformation [27, 44] the time-domain head-wave constituent then follows as

$$W^{\mathrm{HW}}(x_1, x_3, t) = V_0(t) \overset{(t)}{*} \left[W_{\mathrm{b}}^{\mathrm{HW}}(x_1, x_3, t) - W_{\mathrm{a}}^{\mathrm{HW}}(x_1, x_3, t)\right] \qquad \text{(B.18)}$$

with

$$W_{\mathrm{a}}^{\mathrm{HW}}(x_1, x_3, t) = \pi^{-1}\mathrm{Im} \left\{ \tilde{A}\left\{ \gamma_{0,1}\left[p_{\mathrm{a}}^{\mathrm{HW}}(X_{\mathrm{a}}, x_3, t)\right]\right\} \gamma_1 \left[p_{\mathrm{a}}^{\mathrm{HW}}(X_{\mathrm{a}}, x_3, t)\right] / p_{\mathrm{a}}^{\mathrm{HW}}(X_{\mathrm{a}}, x_3, t)\right\}$$
$$\times \Pi\left[(t - T_{\mathrm{Ca}})/T_{\mathrm{La}}\right] (T_{\mathrm{BWa}}^2 - t^2)^{-1/2} \qquad \text{(B.19)}$$

where (B.11) has been used, $\Pi(x)$ is the rectangular function and

$$T_{\mathrm{Ca}} = (T_{\mathrm{HWa}} + T_{\mathrm{BWa}})/2 \qquad \text{(B.20)}$$
$$T_{\mathrm{La}} = T_{\mathrm{BWa}} - T_{\mathrm{HWa}} \qquad \text{(B.21)}$$

Time-domain plane-wave constituent

The s-domain plane-wave constituent follows from (B.1)–(B.2) with (B.12) as

$$\hat{W}_{\mathrm{b}}^{\mathrm{PW}}(x_1, x_3, s) = \tilde{A}(1/c_{0,1})[H(x_1 - a) - H(x_1 - b)]\exp(-sZ/c_1) \qquad \text{(B.22)}$$

On account of Lerch's uniqueness theorem of the unilateral Laplace transformation [27, 44] the time-domain plane-wave constituent then follows as

$$W^{\mathrm{PW}}(x_1, x_3, t) = V_0(t) \overset{(t)}{*} W_{\mathrm{b}}^{\mathrm{PW}}(x_1, x_3, t) \qquad \text{(B.23)}$$

with

$$W_{\mathrm{b}}^{\mathrm{PW}}(x_1, x_3, t) = \tilde{A}(1/c_{0,1})[H(x_1 - a) - H(x_1 - b)]\delta(t - Z/c_1) \qquad \text{(B.24)}$$

These results are used in the main text.

Appendix C

A modal excitation:
The Cagniard-DeHoop technique

This section provides the description of Cagniard-DeHoop method dealing with the generic integral representation concerning a pulsed electromagnetic radiation from a two-dimensional parallel plate waveguide supporting a TM mode. The generic integral representation is (s = time Laplace-transform parameter, p = slowness parameter along x_1)

$$\hat{W}(x_1, x_3, s) = \hat{V}_0(s) \left[\hat{A}(x_1 - w/2, x_3, s) + \hat{A}(x_1 + w/2, x_3, s) \right] \tag{C.1}$$

where

$$\hat{A}(x_1, x_3, s) = \frac{1}{2\pi i} \int_{p=-i\infty}^{i\infty} \exp\{-s[px_1 + \gamma_0(p)x_3]\} \tilde{G}(p, s) \frac{\mathrm{d}p}{\gamma_0(p)} \tag{C.2}$$

where $\gamma_0(p) = (1/c_0^2 - p^2)^{1/2}$ with $\mathrm{Re}[\gamma_0(p)] > 0$ which entails the branch-cuts along $\{1/c_0 < |\mathrm{Re}(p)| < \infty, \mathrm{Im}(p) = 0\}$. The function $\tilde{G}(p, s)$ given in (9.12) has simple pole singularities at $p = \pm in\pi/sw$, but the right-hand side of (C.1) is bounded here. However, the Cagniard-DeHoop technique can only be applied to the separate terms, each of which has simple poles on the imaginary axis. To accommodate this situation, the integration path is replaced with one that is indented to the right with semicircular arcs with centers at $p = \pm in\pi/sw$ and vanishingly small radii. This leads for the integration to the same results. Subsequently, the integral in $\hat{A}(x_1, x_3, s)$ is, under the application of Cauchy's theorem and Jordan's lemma, replaced with the Cagniard-DeHoop path $\mathcal{C} \cup \mathcal{C}^*$, where

$$\mathcal{C} = \left\{ p(\tau) = \frac{x_1\tau + ix_3(\tau^2 - T^2)^{1/2}}{x_1^2 + x_3^2}, T < \tau < \infty \right\} \tag{C.3}$$

in which

$$T = (x_1^2 + x_3^2)^{1/2}/c_0 \tag{C.4}$$

During the contour deformation, a contribution of simple pole singularities has to be taken into account. For the chosen contour indentation, this has to be done for $x_1 \leq 0$ when the Cagniard-DeHoop path lies in left half of the complex p-plane (see Fig. C.1). On
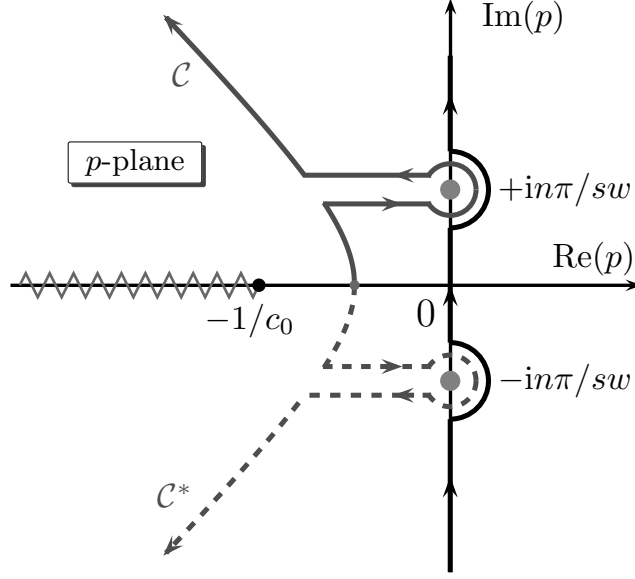
Figure C.1: Illustration of the Cagniard-DeHoop path for $x_1 < 0$ with the original integration contour indented at simple pole singularities $p = \pm \mathrm{i} n\pi/sw$.

account of Lerch's uniqueness theorem of the unilateral Laplace transformation [27, 44], the corresponding time-domain expression for $A(x_1, x_3, t)$ follows as

$$A(x_1, x_3, t) = \frac{1}{\pi} \int_{\tau=T}^{t} \mathrm{Re}\left\{ G[p(\tau), t-\tau] \right\} \frac{\mathrm{d}\tau}{(\tau^2 - T^2)^{1/2}}$$

$$+ c_0 \cos\left(\frac{n\pi x_1}{w}\right) J_0\left[\frac{n\pi c_0}{w}\left(t^2 - \frac{x_3^2}{c_0^2}\right)^{1/2}\right] H\left(t - \frac{x_3}{c_0}\right)[1 - H(x_1)] \qquad \text{(C.5)}$$

for $T > x_3/c_0$ and relation [1, (29.3.92)] has been used. Finally, the time-domain counterpart of $\hat{W}(x_1, x_3, s)$ is given as

$$W(x_1, x_3, t) = V_0(t) \overset{(t)}{*} [A(x_1 - w/2, x_3, t) + A(x_1 + w/2, x_3, t)] \qquad \text{(C.6)}$$

These results are used in the main text.

114

Appendix D

Numerical parametrization of the Cagniard-DeHoop contour

This section aims at providing a numerical approach concernig the numerical parametrization of the Cagniard-DeHoop contour connected with a general pulsed-field problem including planar stratified media. Regarding the problems appearing in this thesis, the analytical expressions for the contour parametrization exist. The parametrization for a single vertical propagation term is given upon solving a quadratic equation and for the case with two progation terms, Cardano's formula can be used. However, for the sake of a generic applicability, we follow the line proposed by De Hoop [13].

Starting with the generic integral representation

$$\hat{W}(X,s) = \frac{1}{2\pi i} \int_{p=-i\infty}^{i\infty} \exp\{-s[pX + \sum_n \gamma_n(p)Z_n]\}\tilde{A}[\gamma_n(p)]\mathrm{d}p \qquad (\text{D.1})$$

where $\gamma_n(p) = (\Omega_n^2 - p^2)^{1/2}$ is n-th vertical propagation term, Z_n and X denote vertical and horizontal propagation path lengths, s is a real and positive Laplace transformation variable, p is a slowness parameter and $\tilde{A}[\gamma_n(p)]$ denotes an algebraic function of the vertical propagation terms. In view of the Cagniard-DeHoop technique we deform the integration path along the imaginary p-axis into the Cagniard-DeHoop contour such that

$$pX + \sum_n \gamma_n(p)Z_n = \tau \qquad (\text{D.2})$$

is real-valued. Keeping $\text{Re}[\gamma_n(p)] \geq 0$ in the entire p-plane implies the branch-cuts along the real axis in the p-plane $\{p \in \mathbb{C}; \Omega_n \leq |\text{Re}(p)| < \infty, \text{Im}(p) = 0\}$.

The first task is to determine a point of intersection of the integration contour with the real p-axis. Corresponding time is found with the help of (D.2) by observing that the contour connected with a body-wave reaches a minimum at this point. Thus, for the first derivative of (D.2) with respect to p we can write

$$\partial\tau/\partial p = X - p \sum_n Z_n \gamma_n^{-1}(p) \qquad (\text{D.3})$$

The stationary points are then determined by solving the equation $\partial\tau/\partial p = 0$. Since the second derivative with respect to p

$$\partial^2\tau/\partial p^2 = -\sum_n \Omega_n^2 Z_n \gamma_n^{-3}(p) \tag{D.4}$$

is negative in the interval $\mathcal{J} : \{p \in \mathbb{C}; 0 < \mathrm{Re}(p) < \Omega_{\min}, \mathrm{Im}(p) = 0\}$ with $\Omega_{\min} = \min_n\{\Omega_n\}$, we can conclude that there is at most one root in this interval. It is immediately clear that in $\mathcal{J}$ exist two points p_A, p_B for which $\partial p/\partial\tau(p_A) > 0$ and $\partial p/\partial\tau(p_B) < 0$, which has the consequence that exactly one root exists in $\mathcal{J}$. Since (D.3) is unbounded at $p = \Omega_{\min}$ we cannot use Newton's root-finding method. Another possible choice, ussually more efficient than the bisection method, is the regula falsi method. The points p_A and p_B are then utilized as the starting points in an iterative process. To find these points we observe that

$$x - \frac{p}{\gamma_{\min}} \sum_n Z_n < \partial\tau/\partial p < x - Z_{\min}\frac{p}{\gamma_{\min}} \tag{D.5}$$

in $\mathcal{J}$, where $Z_{\min}$ is a vertical propagation path length corresponding to $\gamma_{\min} = (\Omega_{\min}^2 - p^2)^{1/2}$. From the latter inequality we can find the the starting points for the iterative process

$$p_A = \Omega_{\min}\frac{X}{[X^2 + (\sum_n Z_n)^2]^{1/2}}, \quad p_B = \Omega_{\min}\frac{X}{(X^2 + Z_{\min}^2)^{1/2}} \tag{D.6}$$

The second derivative (with respect to p) of the function under investigation $\partial\tau/\partial p$ is then given as

$$\partial^3\tau/\partial p^3 = -3p \sum_n \Omega_n^2 Z_n \gamma_n^{-5}(p) \tag{D.7}$$

and is negative for $p \in \mathcal{J}$. Since $\mathrm{sign}\{\partial\tau/\partial p(p_B)\} = \mathrm{sign}\{\partial^3\tau/\partial p^3(p)\}$ for $p \in \mathcal{J}$, the following iteration procedure always converges

$$p_{n+1} = p_n - \frac{p_B - p_n}{\partial\tau/\partial p(p_B) - \partial\tau/\partial p(p_n)}\partial\tau/\partial p(p_n), \text{ with } p_1 = p_A \tag{D.8}$$

Once the iterative procedure (D.8) is terminated with a prescribed precision, the corresponding time T_{BW} is given as

$$p_{B;0}X + \sum_n \gamma_n(p_{B;0})Z_n = T_{\mathrm{BW}} \tag{D.9}$$

where $p_{B;0}$ is the result of the iteration (D.8). In the second step we use Newton's method with the starting value resulting from the asymptotic expression

$$p_\infty = \frac{\tau}{(X - \mathrm{i}\sum_n Z_n)}[1 + O(\tau^{-2})] \text{ as } \tau \to \infty. \tag{D.10}$$

With this starting value, the Cagniard-DeHoop path can be determined for $\tau > T_{\text{BW}}$ with the help of Newton's iterative procedure

$$p_{n+1} = p_n - \frac{F(p_n)}{\partial F/\partial p(p_n)}, \text{ with } p_1 = p_\infty \tag{D.11}$$

where $F(p) = pX + \sum_n \gamma_n(p)Z_n - \tau$.

So far we have considered the part of the Cagniard-DeHoop path connected with the body-waves only. In general, however, a vertical propagation coefficient $\gamma_h(p) = (\Omega_h^2 - p^2)^{1/2}$ can occur in the integrand while the corresponding vertical path length is zero. Then it can happen that $\Omega_h < p_{B;0} < \Omega_{\min}$. In order to avoid crossing the branch-cut, the hyperbolic arc part must be supplemented by a loop around the branch-cut associated with the branch-point Ω_h. Since the position of the branch-point Ω_h is known, the corresponding time is computed from (D.2) as

$$\Omega_h X + \sum_n (\Omega_n^2 - \Omega_h^2)^{1/2} Z_n = T_{\text{HW}} \tag{D.12}$$

The head-wave part of the Cagniard-DeHoop path is then found from (D.2) in the interval $T_{\text{HW}} < \tau < T_{\text{BW}}$. This can be again done iteratively according to the iterative process (D.11) with $p_1 = \Omega_h$.

117

Appendix E

The power exponential pulse

A convenient pulse type to model a unipolar pulse excitation[7] is the *power exponential pulse* [35]

$$V_0(t) = V_{\max}(t/t_{\mathrm{r}})^\nu \exp[-\nu(t/t_{\mathrm{r}} - 1)]H(t) \tag{E.1}$$

where $V_{\max}$ is the *pulse amplitude*, $\nu > 0$ is the *rising exponent* of the pulse and t_{r} is the *pulse rise time*. Note that $V_0(t_{\mathrm{r}}) = V_{\max}$. The *pulse time width* t_{w} follows from

$$V_{\max}t_{\mathrm{w}} = \int_{t=0}^\infty V_0(t)\mathrm{d}t \tag{E.2}$$

as

$$t_{\mathrm{w}} = t_{\mathrm{r}}\nu^{-\nu-1}\Gamma(\nu + 1)\exp(\nu) \tag{E.3}$$

The time Laplace transform of (E.1) is

$$\hat{V}_0(s) = V_{\max}\frac{1}{t_{\mathrm{r}}^\nu}\frac{\Gamma(\nu + 1)}{(s + \nu/t_{\mathrm{r}})^{\nu+1}}\exp(\nu) \tag{E.4}$$

The *spectral amplitude* of $V_0(t)$ follows from (E.4) as

$$|\hat{V}_0(\mathrm{i}\omega)| = V_{\max}\frac{1}{t_{\mathrm{r}}^\nu}\frac{\Gamma(\nu + 1)}{[\omega^2 + (\nu/t_{\mathrm{r}})^2]^{(\nu+1)/2}}\exp(\nu) \tag{E.5}$$

From

$$|\hat{V}_0(\mathrm{i}\omega)/\hat{V}_0(0)| = \frac{1}{[(\omega t_{\mathrm{r}}/\nu)^2 + 1]^{(\nu+1)/2}} \tag{E.6}$$

it follows that both

$$|\hat{V}_0(\mathrm{i}\omega)/\hat{V}_0(0)| \leq 1 \tag{E.7}$$

---

[7]This section is given in the paper [42] with $\nu = 0, 1, 2, \ldots$. Here we assume that ν is a real and positive constant.

118

and

$$|\hat{V}_0(\mathrm{i}\omega)/\hat{V}_0(0)| < \frac{1}{(\omega t_\mathrm{r}/\nu)^{\nu+1}} \tag{E.8}$$

In the *spectral diagram* (where $|\hat{V}_0(\mathrm{i}\omega)|$ is plotted against $|\omega|$, both on logarithmic scales), the right-hand sides of (E.7) and (E.8) are straight lines that are denoted as the *spectral bounds* of $|\hat{V}_0(\mathrm{i}\omega)/\hat{V}_0(0)|$. The two spectral bounds intersect at their *corner point*

$$\omega_\mathrm{corner} = \nu/t_\mathrm{r} \tag{E.9}$$

Bibliography

[1] M. Abramowitz and I. A. Stegun. *Handbook of Mathematical Functions.* Dover Publications, Mineola, NY, 1969.

[2] J. D. Achenbach. *Waves propagation in elastic solids.* North-Holland, Amsterdam, 1975.

[3] K. Aki and P. G. Richards. *Quantitative seismology, 2nd Edition.* University Science Books, Sausalito, California, 2009.

[4] C. E. Baum. General properties of antennas. *IEEE Transactions on Electromagnetic Compatibility*, 44:18–24, February 2002.

[5] L. Cagniard. *Réflexion et réfraction des ondes séismiques progressives.* Gauthier-Villars, Paris, 1939.

[6] L. Cagniard. *Reflection and Refraction of Progressive Seismic Waves.* McGraw-Hill, New York, 1962. (Translation by Flinn, E., Dix, C. H. of Réflexion et réfraction des ondes séismiques progressives, Paris, Gauthier-Villars, 1939).

[7] C. Chapman. *Fundamentals of seismic waves propagation.* Cambridge University Press, Cambridge, UK, 2006.

[8] C. C. Chen and L. Peters. Radar scattering and target imaging obtained using ramp-response techniques. *IEEE Antennas and Propagation Magazine*, 49:13–27, June 2007.

[9] W. C. Chew. *Waves and fields in inhomogeneous media.* IEEE Press, Piscataway, NJ, 1995.

[10] A. T. De Hoop. *Representation theorems for the displacement in an elastic solid and their application to elastodynamic diffraction theory.* PhD thesis, Technical University in Delft, the Netherlands, 1958. chapter IV.

[11] A. T. De Hoop. A modification of Cagniard's method for solving seismic pulse problems. *Applied Scientific Research*, B(8):349–356, 1960.

[12] A. T. De Hoop. Pulsed electromagnetic radiation from a line source in a two-media configuration. *Radio Science*, 14(2):253–268, 1979.

[13] A. T. De Hoop. Transient difussive electromangetic fields in stratified media: Calculation of the two-dimensional E-polarized field. *Radio Science*, 35(2):443–453, 2000.

[14] A. T. De Hoop. Impulsive spherical-wave reflection against a planar absorptive and dispersive dirichlet-to-neumann boundary - an extension of the modified cagniard method. In *2nd Conference on Mathematical Modeling of Wave Phenomena, AIP Conference Proceedings*, volume 834, pages 13–24, Melville, NY, USA, 2006.

[15] A. T. De Hoop. *Handbook of Radiation and Scattering of Waves*. Electronic reproduction, with corrections, 2008.

[16] A. T. De Hoop. Line-source excited pulsed acoustic wave reflection against the mass-loaded boundary of fluid. In *2nd Conference on Mathematical Modeling of Wave Phenomena, AIP Conference Proceedings*, volume 1106, pages 118–129, Melville, NY, USA, 2009.

[17] A. T. De Hoop, I. E. Lager, and V. Tomassetti. The pulsed-field multiport antenna system reciprocity relation and its applications - a time-domain approach. *IEEE Transactions on Antennas and Propagation*, 57:594–605, March 2009.

[18] A. T. De Hoop, C. H. Lam, and B. J. Kooij. Parametrization of acoustic boundary aborption and dispersion properties in time-domain source/receiver reflection measurement. *The Journal of the Acoustical Society of America*, 118(2):654–660, 2005.

[19] A. T. De Hoop, M. Stumpf, and I. E. Lager. Pulsed electromagnetic field radiation from a wide slot antenna with a dielectric layer. *IEEE Transactions on Antennas and Propagation*, 2011. accepted.

[20] L. B. Felsen and N. Marcuvitz. *Radiation and scattering of waves*. John Wiley & Sons, Inc., Hoboken, NJ, 2003.

[21] H. J. Frankena. Transient phenomena associated with Sommerfeld's horizontal dipole problem. *Applied Scientific Research*, B(8):357–368, 1960.

[22] R. F. Harrington. *Time-harmonic electromagnetic fields*. IEEE Press, New York, 2001.

[23] O. Heaviside. *Electromagnetic Theory*, volume I–III. Chelsea Publishing Company, New York, 1971.

[24] I. E. Lager and A. T. De Hoop. Inter-chip and intra-chip pulsed signal transfer between transmitting and receiving loops in wireless interconnect configurations. In *40th Proc. European Microwave Conference - EuMC*, pages 577–580, Paris, France, September 2010.

[25] I. E. Lager and A. T. De Hoop. Loop-to-loop pulsed electromagnetic field wireless integrated circuit interconnects signal transfer. Technical Report IRCTR-S-006-10, International Research Center for Telecommunications and Radar, 2010.

[26] S. W. Lee and L. Grun. Radiation from flanged waveguide: Comparison of solutions. *IEEE Transactions on Antennas and Propagation*, 30:147–148, January 1982.

[27] M. Lerch. Sur un point de la théorie des fonctions génératrices d'Abel. *Acta Mathematica*, 27:339–351, 1903.

[28] R. H. MacPhie and A. I. Zaghloul. Radiation from a rectangular waveguide with infinite flange - exact solution by the correlation matrix method. *IEEE Transactions on Antennas and Propagation*, 28:497–503, July 1980.

[29] N. Marcuvitz. *Waveguide handbook*. Institution of Electrical Engineers, London, 1993.

[30] K. A. Michalski. Extrapolation methods for sommerfeld integral tails. *IEEE Transactions on Antennas and Propagation*, 46:1405–1418, October 1998.

[31] J. Mosig. Integral equation technique. In Itoh T., editor, *Numerical Techniques for Microwave and Millimeter-Wave Passive Structures*, chapter 3, pages 133–213. John Wiley & Sons, 1989.

[32] J. R. Mosig. Arbitrarily shaped microstrip structures and their analysis with a mixed potential integral equation. *IEEE Transactions on Microwave Theory and Techniques*, 36:314–323, February 1988.

[33] S. Nag and L. L. Peters. Radar images of penetrable targets generated from ramp profile functions. *IEEE Transactions on Antennas and Propagation*, 49:32–40, January 2001.

[34] D. M. Pozar, R. E. McIntosh, and S. G. Walker. The optimum feed voltage for a dipole antenna for pulse radiation. *IEEE Transactions on Antennas and Propagation*, 31:563–569, July 1983.

[35] D. Quak. Analysis of transient radiation of a (traveling) current pulse on a straight wire segment. In *Proc. 2001 IEEE EMC International Symposium*, pages 849–854, Montreal, Que., Canada, July 2001.

[36] S. A. Schelkunoff. *Applied mathematics for engineers and scientists*. D. Van Nostrand Company, Inc., New York, 1948.

[37] J. P. Schouten. A new theorem in operational calculus together with an application of it. *Physica*, 2:75–80, 1935.

[38] A. Shlivinski, E. Heyman, and R. Kastner. Antenna characterization in the time-domain. *IEEE Transactions on Antennas and Propagation*, 45:1140–1149, July 1997.

[39] A. Sommerfeld. Uber die ausbreitung der wellen in der drahtlosen telegraphie. *Annalen Der Physik*, 28(4):665–736, 1909.

[40] A. Sommerfeld. *Partial Differential Equations in Physics*. Academic Press, Inc., New York, 1949.

[41] M. Stumpf, A. T. De Hoop, and I. E. Lager. Closed-form time-domain expressions for the 2D pulsed EM field radiated by an array of slot antennas of finite width. In *International Symposium on Electromagnetic Theory*, pages 786–789, URSI Commission B, Berlin, Germany, August 2010.

[42] M. Stumpf, A. T. De Hoop, and I. E. Lager. Pulsed electromagnetic field radiation from a narrow slot antenna with a dielectric layer. *Radio Science*, 45(RS5005), October 2010.

[43] B. Van der Pol. A theorem on electrical networks with an application to filters. *Physica*, 1:521–530, 1934.

[44] D. V. Widder. *The Laplace transform*. Princeton University Press, Princeton, NJ, 1946.

Index

List of Figures

List of Tables

Acknowledgement

Having concluded my work on the application of the Cagniard-DeHoop technique, it is my pleasure to express my gratitude to those who have affected the conception of my thesis.

I am particularly indebted to Prof. Adrianus T. De Hoop for giving me unforgettable "voyage through the landscape of wave field physics". Without his patient guidance this thesis would not come into existence.

I thank Dr. Ioan E. Lager for his bright observations during our discussions on results and for his assistance in improving the quality of the thesis.

I am indebted to Dr. Jaroslav Lacik and to Prof. Zbynek Raida for their constant support and friendliness during my studies in Brno.

Martin Štumpf

CONTACT INFORMATION	Department of Radio Electronics Purkynova 118 Brno University of Technology Brno, 612 00, the Czech Republic	**T** : +420-541-149-117 **F** : +420-541-149-244 **E** : martin.stumpf@centrum.cz **W** : http://www.urel.feec.vutbr.cz

PERSONAL DATA

Date of Birth : 22/09/1983   Place of Birth : Caslav, the Czech Republic
Citizenship : Czech   Marital Status : Unmarried

RESEARCH INTERESTS

Analytical and numerical modeling of electromagnetic, acoustic and elastodynamic wave phenomena, Cagniard-DeHoop technique, selected EMC problems

EDUCATION

Brno University of Technology, Brno, Czech Republic

Ph.D. Candidate, Electrical Engineering, September 2008 – expected on May 2011

- Dissertation Topic: "Pulsed electromagnetic field radiation from slot antennas"
- Advisors: Jaroslav Lacik, Zbynek Raida (BUT Brno), Adrianus T. De Hoop, Ioan E. Lager (TU Delft).

Brno University of Technology, Brno, Czech Republic

M.Sc., Electrical Engineering, September 2006 – June 2008

- Diploma Thesis: "Implementation and Testing of a 2D-Integral Equation MoM-Algorithm for the Analysis of Power-Bus Structures on Printed Circuit Boards" (in English)
- Advisor: Marco Leone (Otto von Guericke University)

Brno University of Technology, Brno, Czech Republic

B.Sc., Electrical Engineering, September 2003 – June 2006

- Bachelor Thesis: "Analysis of Frequency Selective Surfaces Using Spectral-Domain MoM" (in Czech)
- Advisor: Ivo Hertl (BUT Brno)

The Secondary School of Electrical Engineering, Pardubice, Czech Republic

Leaving examination, Computer and Automation Engineering, September 1999 – June 2003

- Final Project: "Design of a device for a measurement of bipolar transistor characteristics" (in Czech)

The Primary School, Choltice, Czech Republic

2nd level, September 1994 – June 1999

The Primary School, Lipoltice, Czech Republic

1st level, September 1990 – June 1994

Honors and Awards	• Young Scientist Award, URSI ElectroMagnetic Theory Symposium, Berlin, 2010.
	• Best Diploma Thesis Award in 2008, MTT/AP/ED/EMC Joint Chapter of the Czechoslovak Section of IEEE.
	• Award of the Chancellor of Brno University of Technology, 2008.
	• Award of the Dean of Brno University of Technology, 2008.
	• Best Paper Award, the conference Student EEICT, 2006.

Internships

February - June 2008   **Otto-von-Guericke University Magdeburg, Germany**
Institute for Fundamental Electrical Engineering and Electromagnetic Compatibility, Germany. Advisor : Marco Leone.

February - March 2009   **Delft University of Technology, the Netherlands**
International Research Centre for Telecommunication and Radar, Laboratory for Electromagnetic Research, the Netherlands. Advisors : Ioan E. Lager, Adrianus T. De Hoop.

November - December 2009   **Delft University of Technology, the Netherlands**
International Research Centre for Telecommunication and Radar, Laboratory for Electromagnetic Research, the Netherlands. Advisors : Ioan E. Lager, Adrianus T. De Hoop.

October - December 2010   **Delft University of Technology, the Netherlands**
International Research Centre for Telecommunication and Radar, Laboratory for Electromagnetic Research, the Netherlands. Advisors : Ioan E. Lager, Adrianus T. De Hoop.

Academic Experience

Brno University of Technology, Brno, Czech Republic

February - June, 2009   *Instructor*
Co-taught course for the Bachelors of Science in Computers and Programming 2. Shared responsibility for exams and grades.
• BPC2 – Computers and Programming 2, Summer 2009.

February - June, 2010   *Instructor*
Co-taught course for the Bachelors of Science in Computers and Programming 2. Shared responsibility for exams and grades.
• BPC2 – Computers and Programming 2, Summer 2010.

Courses Attended

The 19th International Travelling Summer Schools on Microwaves and Lightwaves (ITSS 2009), Roma, Italy, 4–10 July 2009.

The European School of Antennas (ESoA), course name: Time domain techniques for antenna analysis, Nice, France, 13–17 October 2008.

Selected Publications

M. Stumpf, A. T. De Hoop, and I. E. Lager, "Pulsed electromagnetic field radiation from a narrow slot antenna with a dielectric layer," *Radio Science*, 45, RS5005, doi:10.1029/2009RS004335, October 2010.

A. T. De Hoop, M. Stumpf and I. E. Lager, "Pulsed electromagnetic field radiation from a wide slot antenna with a dielectric layer," *IEEE Transactions on Antennas and Propagation*, accepted for publication, 2011.

M. Stumpf, M. Leone, "Efficient 2D-integral equation approach for the analysis of power-bus structures with arbitrary shape," *IEEE Transactions on Electromagnetic Compatibility*, vol. 51, no. 1, pp. 38–45, February 2009.

M. Stumpf, A. T. De Hoop and I. E. Lager, "Closed-form time-domain expressions for the 2D pulsed EM field radiated by an array of slot antennas of finite width," in *Proc. International Symposium on Electromagnetic Theory*, URSI Commission B, Berlin, pp. 786–789, August 2010.

M. Stumpf, O. Kroening, and M. Leone, "Power-bus modeling using 2D-integral-equation formulation," in *Proc. 20th International Symposium on Electromagnetic Compatibility EMC Zurich 2009*, Switzerland, pp. 189–192, January 2009.

COMPUTER SKILLS
- Languages: C/C++, Pascal, Matlab.
- Electromagnetic Tools: CST Microwave Studio, Ansoft Designer.